2008

Thin water films driven by air through surface roughness

Guoqing Wang
Iowa State University

Recommended Citation

Wang, Guoqing, "Thin water films driven by air through surface roughness" (2008). *Retrospective Theses and Dissertations*. 15864.
https://lib.dr.iastate.edu/rtd/15864

Thin water films driven by air through surface roughness

by

Guoqing Wang

A dissertation submitted to the graduate faculty
in partial fulfillment of the requirements for the degree of
DOCTOR OF PHILOSOPHY

Major: Aerospace Engineering

Program of Study Committee:
Alric Rothmayer, Major Professor
Richard H. Pletcher
Tom I-Ping Shih
Ambar K. Mitra
Fred L. Haan

Iowa State University

Ames, Iowa

2008

ProQuest Information and Learning Company
300 North Zeeb Road
P.O. Box 1346
Ann Arbor, MI 48106-1346

DEDICATION

I would like to dedicate this dissertation to my wife Xi Chen and my daughter Cindy. Their support is the power for me to complete this work.

TABLE OF CONTENTS

LIST OF TABLES

LIST OF FIGURES

ACKNOWLEDGEMENTS

I would like to take this opportunity to express my thanks to those who helped me with various aspects of conducting research and the writing of this dissertation. First and foremost, Dr. Alric Rothmayer for his guidance, patience and support throughout this research and the writing of this dissertation. I would also like to thank my committee for their efforts and contributions to this work: Dr. Richard H. Pletcher, Dr. Tom I-Ping Shih, Dr. Ambar K. Mitra, and Dr. Fred L. Haan. I would also like to thank Dr. Mark G. Potapczuk, Dr. Jen Ching Tsao, Mr. Brian D. Matheis, Mr. Otta P. Shourya, Mr. Joshua A. Krakos, Mr. Ben Rider for their help during these years.

This research was partially supported by NASA contract NAG3-2863, through the Icing Branch at the NASA Glenn Research Center. The author would like to thank Dr. M. Potapczuk and T. Bond for their helpful guidance and support.

My wife, Xi Chen, my parents, Mr. Gaobo Xiao and Mrs. Yihua Wang, and my parents-in-law, Mr. Youshi Chen and Mrs. Sufen Fu, deserve special thanks for their undivided attention and moral support.

ABSTRACT

The interaction between thin films and roughness surfaces has been studied when the thin viscosity-dominated films are driven by the air shear stress in the context of a high Reynolds number boundary layer theory. A number of properties of this model are examined, such as transport and pooling of water in a roughness field, heat transfer of film/roughness combinations, and rivulet formation. For rivulet formation due to the instability of two-dimensional film fronts, a general formula for the largest unstable wavelength, the fastest temporal growth rate, and the neutral wavelength has been developed from the linear instability analysis. This formula is validated using experimental data for film fronts on flat surfaces which are driven by constant surface tension gradients. This formula is also validated using numerical simulations of film fronts moving through various roughened surfaces.

To describe a water bead on a precursor film, a new disjoining pressure model is developed from a modified classical long-distance disjoining pressure model. This model satisfies the requirement that the disjoining pressure on the precursor film is larger than zero. Another advantage of this modified model is that an effective distance used in classical long-distance disjoining pressure models is avoided even when a water bead is on a dry surface. This model is validated using experimental data from aircraft icing tests.

CHAPTER 1. Introduction

When an aircraft flies through a cloud of supercooled water droplets, and the temperature is sufficiently low, the droplets can impact the aircraft and ice can accrete on wing surfaces. At temperature sufficiently close to freezing, impacting droplets partially freeze and a residue of water can remain on a roughened ice surface, often in the form of a thin water film. A number of studies have shown that air-driven films are a common feature of water transport along accreted ice surfaces. For example, Thomas, Cassoni & MacArthur (1996) have shown that supercooled droplets on ice run back as a liquid film, and experiments by Vargas (2005) have shown that the ice surface can be wet everywhere in glaze icing conditions near the stagnation line. Thin water films are also a commonly used model for water transport in engineering simulations of aircraft icing (see Bourgault, Beaugendre & Habashi 2000; Myers, Charpin & Chapman 2002, for example).

Thin films which are driven by body and external forces have been studied both experimentally and theoretically in a variety of situations, with the majority of cases involving gravity and Marangoni forces. For gravity driven films, Huppert (1982) experimentally showed that a film front moving along an inclined plate became unstable to disturbances along the front, forming rivulets. Huppert also found that the wavelength of the unstable film front was a function of both the surface tension and the gravity force component directed along the surface (also see Silvi & Dussan 1985; Jerrett & de Bruyn 1992). Stability of gravity-driven film fronts on an inclined surface were studied numerically by Troian, Herbolzheimer, Safran & Joanny (1989) (also see Schwartz 1989; Bertozzi & Brenner 1997). A number of authors have considered similar effects when the film is driven by Marangoni forces, which are stresses generated by temperature gradients (see Levich 1962; Levich & Krylov 1969; Cazabat, Heslot, Troian

& Carles 1990; Cazabat, Heslot, Carles & Troian 1992; Oron, Davis, & Bankoff 1997; Eres, Schwartz & Roy 2000; Luo & Pozrikdis 2006).

For wind-driven shallow water, the formation of interfacial waves and hydrodynamic stabilities have been studied with linear theories (see Lin 1955; Stoker 1957; Lighthill 1978) as well as with nonlinear theories (see Eckhaus 1965; Whitham 1974; Joseph 1976; Leibovich & Seebass 1974). The generation of wind-driven waves on thin films has been examined by Lock (1954), Craik (1966) and Akylas (1982), while equivalent studies of waves driven by turbulent air streams may be found in Miles (1959, 1962) (also see Valenzuela 1976; van Gastel, Janssen & Komen 1985; Belcher, Harris & Street 1994). A long-wave instability mechanism of water-wave formation induced by viscosity differences at interfaces has been studied by Yih (1967, 1990), while short-wave viscous instabilities have been studied by Hooper & Boyd (1987) (also see Blennerhassett & Smith 1987). Of more relevance to this study, high Reynolds number asymptotic methods have been used by Feldman (1957) (also see Timoshin 1997; Tsao, Rothmayer & Ruban 1997; Rothmayer & Tsao 2000) to study the instability of thin shear-driven films. Recent experiments by Marshall & Ettema (2004) have also examined the formation of wind-driven rivulets, but starting from very large droplets.

This study primarily focuses on thin water films driven by air shear stress through roughness, where thin viscosity-dominated films are described in the context of a high Reynolds number boundary layer theory on scales which are small enough that air driven instabilities do not effect the flow. A number of properties of this model are examined, including transport and pooling of water in a roughness field, heat transfer of film/roughness combinations, run-back of water beads, and rivulet formation due to the instability of two-dimensional film fronts.

CHAPTER 2. Thin water films

In the current study, water is driven by air through a roughness field which lies underneath an attached laminar Prandtl boundary layer. The air is assumed to be an ideal gas and the water is incompressible. In following sections, the superscript "$*$" denotes variables which are dimensional, while the subscript "∞" denotes free-stream variables. For example, the density ρ_∞, velocity V_∞, temperature θ_∞, and pressure P_∞ are reference variables measured in the air free stream. The characteristic length L is typically taken to be the radius of curvature of the leading edge of an airfoil or an airfoil chord length.

A non-dimensional Cartesian coordinates system (x, y, z) is located at a point within a laminar Prandtl boundary layer, where the local non-dimensional streamwise shear stress is $Re^{-1/2}\lambda$, where $Re = \rho_\infty V_\infty L/\mu_\infty$ is the free-stream Reynolds number. The coordinate x is the streamwise direction, y is the normal direction to the surface, and z is the spanwise direction.

2.1 Films driven by nonlinear condensed layers

When a thin liquid film is driven by air over roughness with diameter $Re^{-3/4} \ll \Delta \ll Re^{-3/8}$ and height $Re^{-1/2}\Delta^{1/3}$, the *condensed layer* or *wall layer* (see Bogolepov & Neiland 1971, 1976; Smith, Brighton, Jackson & Hunt 1981; Rothmayer & Smith 1998) allows a pressure and shear stress feedback between the viscous sublayer airflow and the liquid film when the length scale of the interaction is $\Delta = Re^{-9/14}\sigma^{3/7}$ (see Rothmayer & Tsao 2000; Rothmayer, Matheis & Timoshin 2002), where $\sigma = \sigma^*/\left(V_\infty \mu_\infty\right)$ is a dimensionless surface tension. The air pressure and shear at the liquid/air interface tend to destabilize the liquid surface, while surface tension acts to stabilize the interface. The condensed layer streamwise, spanwise and wall normal length scales of Rothmayer & Tsao (2000) are given in terms of the Reynolds number Re and dimensionless surface tension σ, with

$$(x, y, z) = \left(Re^{-9/14}\sigma^{3/7}X,\ Re^{-5/7}\sigma^{1/7}Y,\ Re^{-9/14}\sigma^{3/7}Z\right). \tag{2.1}$$

When the surface tension is large (i.e. $\sigma \sim O\left(Re^{5/8}\right)$) this interaction is controlled by a triple-deck (see Neiland 1969; Stewartson & Williams 1969; Messiter 1970; Timoshin 1997; Tsao *et al.* 1997; Timoshin & Hooper 2000; Pelekasis & Tsamopoulos 2001).

In the condensed layer, both the air sublayer and water film are controlled by unsteady boundary layer equations, providing that the viscosity ratio $\mathrm{M} = \mu^*_{water}(\theta_\infty)/\mu_\infty$ between the air and water is related to the density ratio, $D_{aw} = \rho_\infty/\rho^*_{water}$, as follows

$$\mathrm{M} = \mathcal{M} D_{aw}^{-1/2}, \tag{2.2}$$

where $\mathcal{M}$ typically ranges from 3 to 5 (see Rothmayer 2003). The air and water are coupled through a combination of pressure and shear stress in the sense that changes to the water interface shape create a pressure and shear stress response in the air, and the pressure and shear stress combination drives the water into motion. Solutions of the triple-deck and condensed layer problems may be found in Timoshin (1997), Tsao *et al.* (1997), Rothmayer & Tsao (2000), Pelekasis & Tsamopoulos (2001), Rothmayer *et al.* (2002) and Matheis & Rothmayer (2003).

2.2 Films on scales shorter than the condensed layer

An asymptotic solution on scales shorter than those of the condensed layer is used here to examine properties of the Rothmayer & Tsao (2000) structure in a simplified setting. The main new perturbation parameter is the streamwise length scale, Δ, which is assumed to be less than the condensed layer value of Rothmayer & Tsao (2000) but larger than the near wall Navier-Stokes scale, i.e.

$$Re^{-3/4} \ll \Delta \ll Re^{-9/14}\sigma^{-3/7}. \tag{2.3}$$

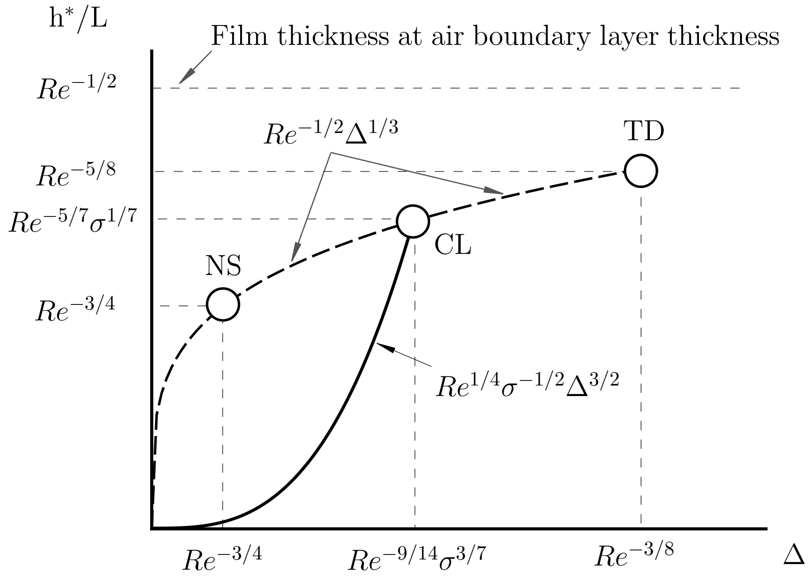

Figure 2.1 The roughness diameters, $\triangle$, and the roughness/water heights, h*/L, showing the relationship of the short scale roughness considered in this study to the condensed layer (CL), triple-deck (TD) and near-wall Navier-Stokes (NS) structures.

Wang & Rothmayer (2005) found that surface roughness on this scale, as shown in figure 2.1, can first interact with a thin film when the film thickness and roughness heights are both

$$h^*/L = Re^{1/4}\sigma^{-1/2}\Delta^{3/2}h, \tag{2.4}$$

where h^* is a dimensional undisturbed film thickness. This relation effectively sets the streamwise length scale for the interaction, given a known ambient film thickness h^*/L. When the surface roughness is the perturbation source for the air and water system, the time scale for a laminar unsteady response of the water interface is

$$t = Re^{-3/4}\sigma^{1/2}D_{aw}^{-1/2}\Delta^{-1/2}\mathcal{T}, \tag{2.5}$$

and the air is quasi-steady and laminar. Some trial and error reveals that the expansions of lengths, velocities, temperature and pressure in the water film take the form

$$(x, y, z) = \left(\Delta X,\ Re^{1/4}\sigma^{-1/2}\Delta^{3/2}Y,\ \Delta Z\right), \tag{2.6}$$

$$(u,\, v,\, w) \sim \left(Re^{3/4}\sigma^{-1/2}D_{aw}^{1/2}\Delta^{3/2}U,\; Re\sigma^{-1}D_{aw}^{1/2}\Delta^{2}V,\; Re^{3/4}\sigma^{-1/2}D_{aw}^{1/2}\Delta^{3/2}W \right) + \cdots \,, \tag{2.7}$$

$$\theta \sim 1 \mp \Theta + Re^{3/4}\sigma^{-1/2}D_{aw}^{1/2}\Delta^{3/2}\Theta\vartheta + \cdots \,, \tag{2.8}$$

where the upper sign "$-$" is used for above freezing freestream and the lower sign "$+$" is used for below freezing freestream. The water pressure is

$$p \sim P_B + Re^{-3/4}\sigma^{1/2}\Delta^{-1/2}P + \cdots \,, \tag{2.9}$$

where P_B is the local air boundary layer pressure. The air, on the other hand, is a linearized condensed layer with

$$(\hat{x}, \hat{y}, \hat{z}) = \left(\Delta\hat{X}, Re^{-1/2}\Delta^{1/3}\hat{Y}, \Delta\hat{Z} \right), \tag{2.10}$$

$$\left.\begin{aligned} \hat{u} &\sim \Delta^{1/3}\lambda\hat{Y} + Re^{3/4}\sigma^{-1/2}\Delta^{3/2}\hat{U} + \cdots \,, \\ \hat{v} &\sim Re^{1/4}\sigma^{-1/2}\Delta^{5/6}\hat{V} + \cdots \,, \\ \hat{w} &\sim Re^{3/4}\sigma^{-1/2}\Delta^{3/2}\hat{W} + \cdots \,, \end{aligned}\right\} \tag{2.11}$$

$$\hat{\theta} \sim 1 \mp \Theta + q\Delta^{1/3}\Theta\hat{Y} + Re^{3/4}\sigma^{-1/2}\Delta^{3/2}\Theta\hat{\vartheta} + \cdots \,, \tag{2.12}$$

and

$$\hat{p} \sim P_B + Re^{3/4}\sigma^{-1/2}\Delta^{11/6}\hat{P} + \cdots \,, \tag{2.13}$$

where λ is the air boundary layer shear stress and q is the boundary layer heat flux in the air, i.e. $q = Re^{-1/2}\Theta^{-1}\partial\hat{\theta}/\partial\hat{y}$, both measured at the wall. Note that Θ is a dimensionless perturbation of the free-stream temperature θ_∞ from a constant prescribed wall temperature, which is taken to be the freezing temperature $\theta^*_{freezing}$ for aircraft icing applications, i.e. $\Theta = \left| \left(\theta^*_{freezing} - \theta_\infty \right) / \theta^*_{freezing} \right|$. The water surface and the underlying surface roughness have the same height scale as that of the undisturbed water film, i.e.

$$(f_{water}, f_{ice}) \sim Re^{1/4}\sigma^{-1/2}\Delta^{3/2}\left(F_{water}, F_{ice}\right) + \cdots \,, \tag{2.14}$$

where f_{water} and f_{ice} are the functions for water film height and underlying ice roughness, respectively.

The following equations are obtained by substituting the above expansions into the non-dimensionalized mass conservation equation, the Navier-Stokes equations, and the energy conservation equation in both the air and water. In these equations, gravity is assumed to be sufficiently small, i.e.

$$G = \frac{Lg}{V_\infty^2} \ll Re^{-3/4}\sigma^{1/2}D_{aw}\Delta^{-3/2}, \tag{2.15}$$

where $g = 9.8\mathrm{m/s}^2$. In the air, the mass conservation equation is

$$\frac{\partial \hat{U}}{\partial \hat{X}} + \frac{\partial \hat{V}}{\partial \hat{Y}} + \frac{\partial \hat{W}}{\partial \hat{Z}} = 0. \tag{2.16}$$

The momentum conservation equations are

$$\lambda \hat{Y}\frac{\partial \hat{U}}{\partial \hat{X}} + \lambda \hat{V} = -\frac{\partial \hat{P}}{\partial \hat{X}} + \frac{\partial^2 \hat{U}}{\partial \hat{Y}^2}, \tag{2.17}$$

$$\frac{\partial \hat{P}}{\partial \hat{Y}} = 0, \tag{2.18}$$

and

$$\lambda \hat{Y}\frac{\partial \hat{W}}{\partial \hat{X}} = -\frac{\partial \hat{P}}{\partial \hat{Z}} + \frac{\partial^2 \hat{W}}{\partial \hat{Y}^2}. \tag{2.19}$$

The energy conservation equation is

$$\lambda \hat{Y}\frac{\partial \tilde{\vartheta}}{\partial \hat{X}} + q\hat{V} = Pr^{-1}\frac{\partial^2 \hat{\vartheta}}{\partial \hat{Y}^2}. \tag{2.20}$$

The boundary conditions in the air are

$$\hat{U} \to \lambda\left(F_{water} - h\right) \quad \text{and} \quad \hat{\vartheta} \to q\left(F_{water} - h\right) \quad \text{as} \quad \hat{Y} \to \infty, \tag{2.21}$$

and

$$\hat{U} = \hat{V} = \hat{W} = 0 \quad \text{and} \quad \hat{\vartheta} = 0 \quad \text{on} \quad \hat{Y} = F_{water}, \tag{2.22}$$

where h is the undisturbed dimensionless water film thickness. In the water, the mass, momentum, and energy equations are

$$\frac{\partial U}{\partial X} + \frac{\partial V}{\partial Y} + \frac{\partial W}{\partial Z} = 0, \tag{2.23}$$

$$0 = -\frac{\partial P}{\partial X} + \mathcal{M}\frac{\partial^2 U}{\partial Y^2}, \tag{2.24}$$

$$\frac{\partial P}{\partial Y} = 0, \tag{2.25}$$

$$0 = -\frac{\partial P}{\partial Z} + \mathcal{M}\frac{\partial^2 W}{\partial Y^2}, \tag{2.26}$$

and

$$Pr^{-1}\frac{\partial^2 \vartheta}{\partial Y^2} = 0. \tag{2.27}$$

At the interface between water and the solid ice surface, the conditions of no-slip and constant wall temperature are

$$U_{water} = V_{water} = W_{water} = 0 \quad \text{and} \quad \vartheta = 0 \quad \text{on} \quad Y = F_{ice}. \tag{2.28}$$

At the interface between water and air, the shear stress in air is balanced by that in the water, i.e.

$$\mathcal{M}\left(\frac{\partial U}{\partial Y}\right)_{water} = \lambda \text{ and } \mathcal{M}\left(\frac{\partial W}{\partial Y}\right)_{water} = 0 \text{ on } Y = F_{water}, \tag{2.29a,b}$$

and the pressure is balanced by surface tension due to the curvature of the water surface

$$P = -\left(\frac{\partial^2 F_{water}}{\partial X^2} + \frac{\partial^2 F_{water}}{\partial Z^2}\right) \quad \text{on} \quad Y = F_{water}. \tag{2.30}$$

The kinematic condition on the water/air interface $Y = F_{water}$ is

$$V_{water} = \frac{\partial F_{water}}{\partial \mathcal{T}} + U_{water}\frac{\partial F_{water}}{\partial X} + W_{water}\frac{\partial F_{water}}{\partial Z}. \tag{2.31}$$

Combining equations (2.23-2.31), a lubrication equation is found for the water interface

$$\frac{\partial F_{water}}{\partial T} + \frac{\partial}{\partial X}\left(\lambda\frac{F^2}{2}\right) + \frac{\partial}{\partial X}\left(-\frac{F^3}{3}\frac{\partial P}{\partial X}\right) + \frac{\partial}{\partial Z}\left(-\frac{F^3}{3}\frac{\partial P}{\partial Z}\right) = 0, \tag{2.32}$$

where $T = \mathcal{T}/\mathcal{M}$, $F = F_{water} - F_{ice}$ and P is given by equation (2.30). Note that in contrast to the condensed layer and triple-deck, the air is now decoupled from the water film. The water film is solved first, given an applied air shear stress, and the air has a linear response to changes in the water film interface shape.

2.3 Numerical methods and solutions

When numerically simulating the motion of a thin film, one challenging problem is the development of a model which captures fluid spreading on any surface where three media can co-exist, namely liquid, gas, and solid. The interface between these three media is called the contact line. The central problem (see Dussan 1979; de Gennes 1985) is that the boundaries for both liquid and gas on the solid surface are no-slip, i.e. zero velocity, whereas the liquid must be able to move forward or backward along the solid surface in order to move the contact line. This situation leads to a stress singularity at the contact line. Current understanding of general contact line behavior is poor and often requires complex and detailed simulations near the contact line, which is beyond the scope of this study. However, there are a number of well-known ways to avoid the contact line singularity in numerical simulations, for example by using a slip boundary condition (see Dussan & Davis 1974) or a precursor film (see Diez, Kondic & Bertozzi 2000). In this study, the precursor film method is used. In other words, it is assumed that the whole roughness field is covered by a very thin water film. A fourth order Runge-Kutta method is used for the time integration of the lubrication equation (2.32) (see Abramowitz & Stegun 1972). For the spatial differencing, a combination of central differencing and the positivity preserving scheme of Diez *et al.* (2000) is used. In the air, the Smith (1983) transformation is used for equations (2.16-2.20). The resulting air equations are solved using a finite difference method.

2.3.1 Films and beads flowing through roughness fields

Figure 2.2 shows a grid size study for a single, smooth, two-dimensional roughness element which is initially covered by a water film with uniform thickness, where the initial film thickness is $h = 0.2$ and the air shear stress is $\lambda = 4$. The roughness shape is given by

$$F_{ice}\left(X, Z\right) = c \cdot exp\left[-\sum_{n=0}^{N} \frac{t^n}{2n}\right], \tag{2.33}$$

where, in three-dimensions, $t = \left(X - X_0\right)^2/a^2 + \left(Z - Z_0\right)^2/b^2$. In figure 2.2, $c = 1$, $b = \infty$ and $N = 5$. Note that if $a = b = c$ then equation (2.33) approaches a hemisphere as $N \to \infty$.

Due to the interaction between the roughness and water film, the water mass is redistributed about the roughness element. The film surface becomes steady at long time in the immediate vicinity of the roughness element, which is the result shown in figure 2.2(a). At the same time, a decaying traveling wave is observed far downstream of the roughness, as shown in figure 2.2(b). It should be noted that the numerical simulations with different grid sizes shown in figure 2.2 agree well with each other.

Equivalent steady solutions about three-dimensional roughness fields are shown in figure 2.3. The roughness elements are distributed using two patterns: an aligned pattern is shown in figures 2.3(a) and 2.3(b), and an offset pattern is shown in figures 2.3(c) and 2.3(d). The hump geometry in figure 2.3 is given by equation (2.33) with $N = 4$. Initially, a uniform thin water film covers the entire domain, where the upstream film thickness is $h = 0.1$ and the air shear stress is $\lambda = 4$. In these figures, the green areas correspond to films having a thickness which is the same as that of the undisturbed upstream film. The red regions have smaller film thickness (down to 50% of the initial film thickness), and the blue regions have larger film thickness (up to 150% of the initial film thickness). Figures 2.3(a) and 2.3(b) show that the film pools near the first row of roughness elements, is directed into the trough between the downstream roughness, and thins out in the region immediately behind each roughness element. Similar solutions are seen in the first row of offset roughness elements, i.e. figures 2.3(c) and 2.3(d). However, in the offset case, the water from the gap between the first row directly impacts the roughness elements in the second row, pooling in front of the second row of roughness elements and subsequently flowing into the gaps between the roughness. This pattern is repeated further downstream.

When large beads are placed on the surface, they run back and eventually tend to form rivulets, as shown in figures 2.4 and 2.5. The roughness geometry in these figures is a smoothed parabola of revolution with $N = 6$ in equation (2.34), and the initial bead geometry is a parabola of revolution with $N = 4$ in (2.34). The formula used to generate the smoothed elliptic paraboloid is

$$F_{ice}\left(X, Z\right) = c \cdot exp\left(-\sum_{n=0}^{N} \frac{t^n}{n}\right), \tag{2.34}$$

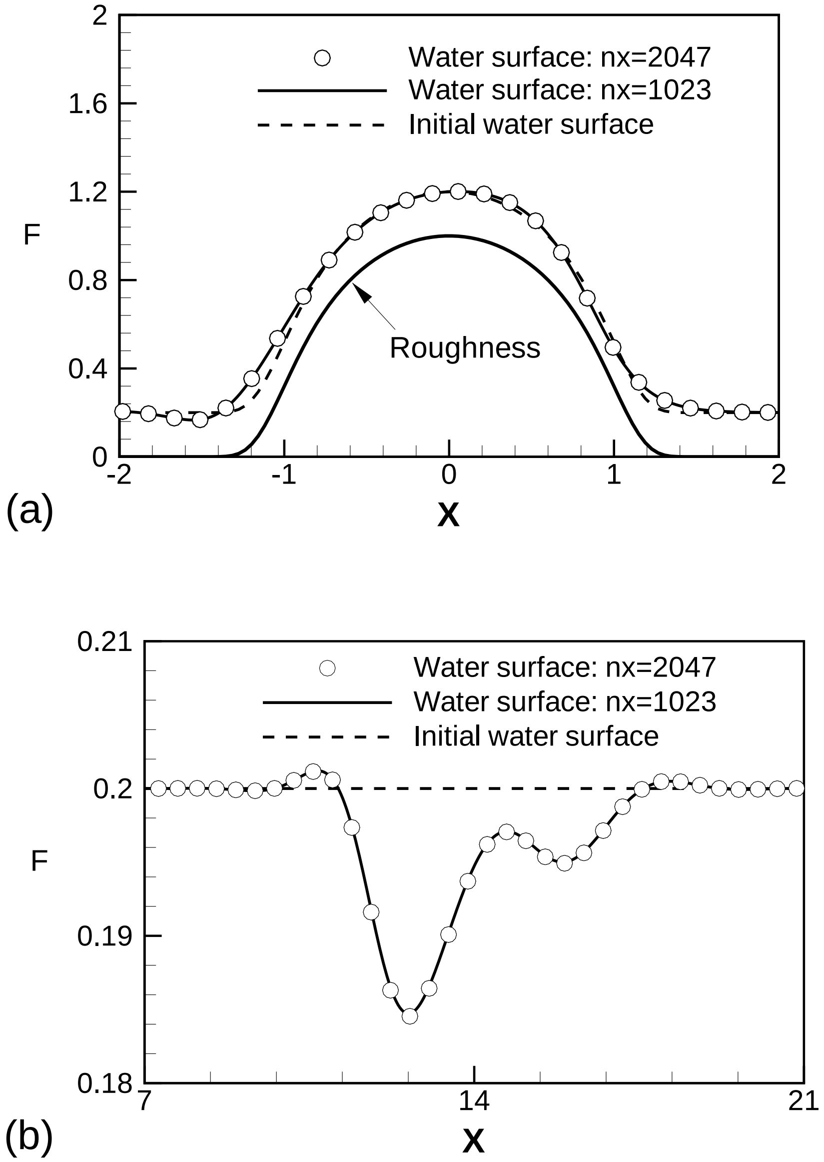

Figure 2.2 Typical two-dimensional flow of an initially uniform film driven by air shear stress past a single roughness element at $T = 18.31$. (a) Steady film around the roughness element, (b) traveling wave far downstream of the roughness, generated by the unsteady flow past the roughness at early time. The spatial computational domain is X $\in (-12,\ 28)$, and nx is the number of spatial grid points.

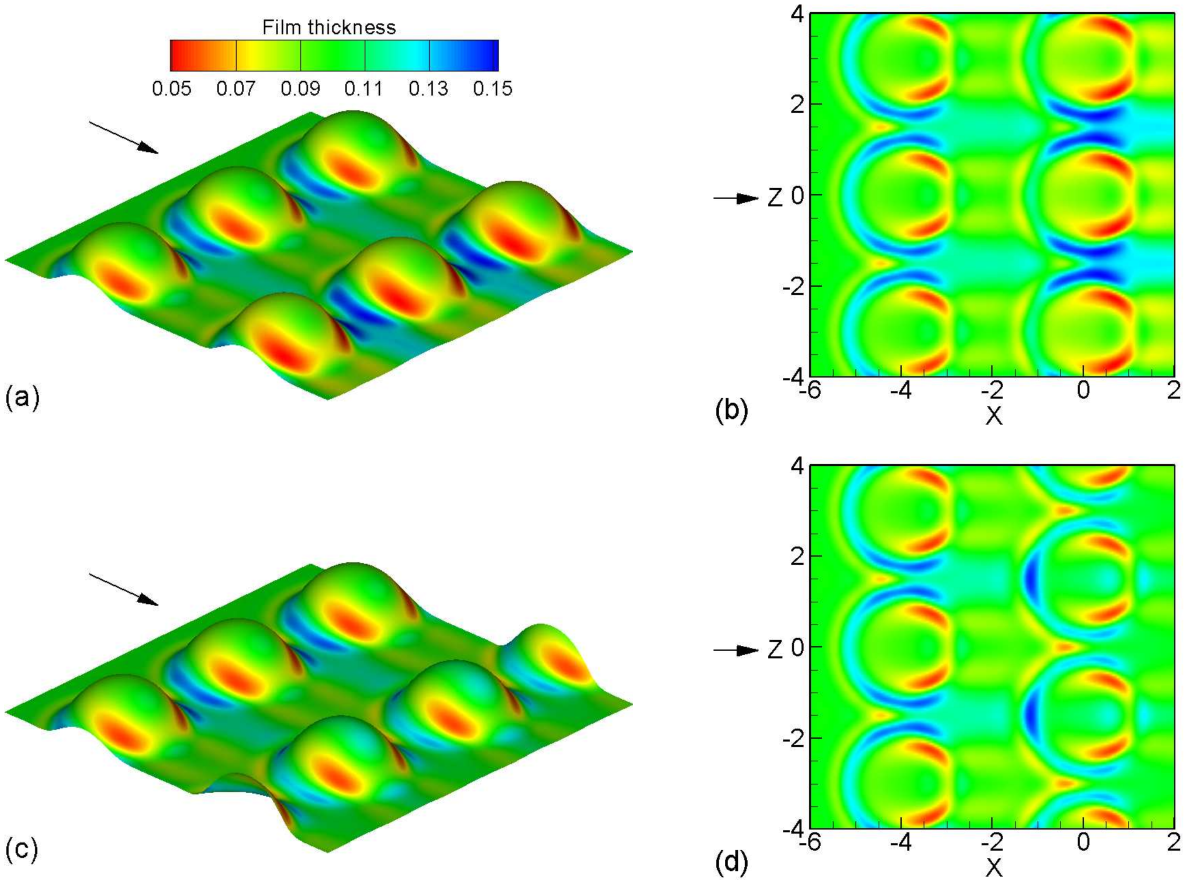

Figure 2.3 Typical steady state water film driven by air shear stress through a three dimensional roughness field: (a) 3D view and (b) top view of aligned roughness, (c) 3D view and (d) top view of offset roughness. Water flow and air shear is in direction of the arrows. The undisturbed film thickness is 0.1.

with $t = \left[a\,(X - X_0)^2 + b\,(Z - Z_0)^2\right]/c$. In figures 2.4(a) and 2.4(b), the same large water beads are placed far upstream of an aligned and offset roughness field, respectively, and the entire downstream surface is covered by a very thin film. These beads are about three times the height of the downstream roughness elements. In figures 2.5(a-f), the blue regions are the regions which are covered by an extremely thin film (about 1.4% of the roughness height). The film thickness increases progressively as the color changes from blue to red. As shown in figures 2.5(a) and 2.5(b), the leading row of beads form rivulets as they run back along the smooth surface, while the beads in the second row flow into the rivulets created by the first row. When the rivulets pass through the aligned roughness field, the troughs between the roughness elements channel the water flow and promote rivulet formation immediately downstream of the roughness field, as shown in figure 2.5(e). When the same rivulets pass through an offset roughness field, as shown in figure 2.5(b), the rivulets maintain their shape within and downstream of the roughness field, as shown in figure 2.5(f). In this case, no secondary rivulets are created when the water exits the offset roughness field.

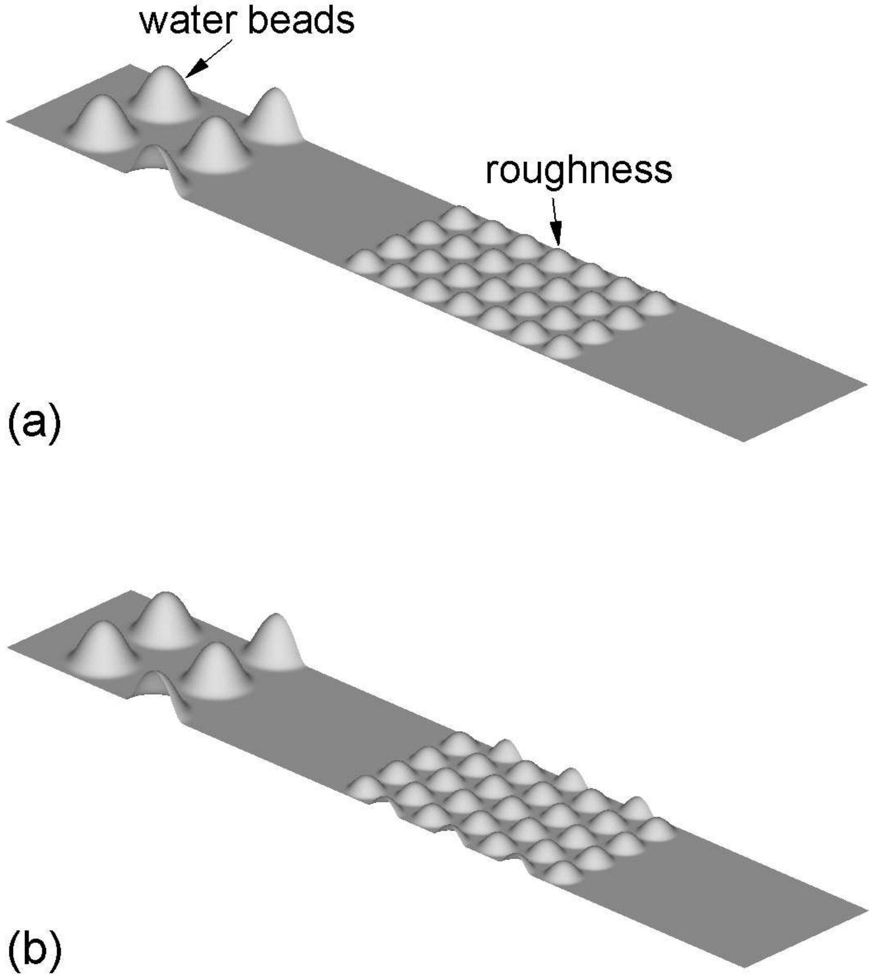

Figure 2.4 Starting conditions for the solutions shown in figures 2.5 and 2.7. Water beads are placed upstream of a roughness field: (a) initial beads and aligned roughness, and (b) initial beads and offset roughness.

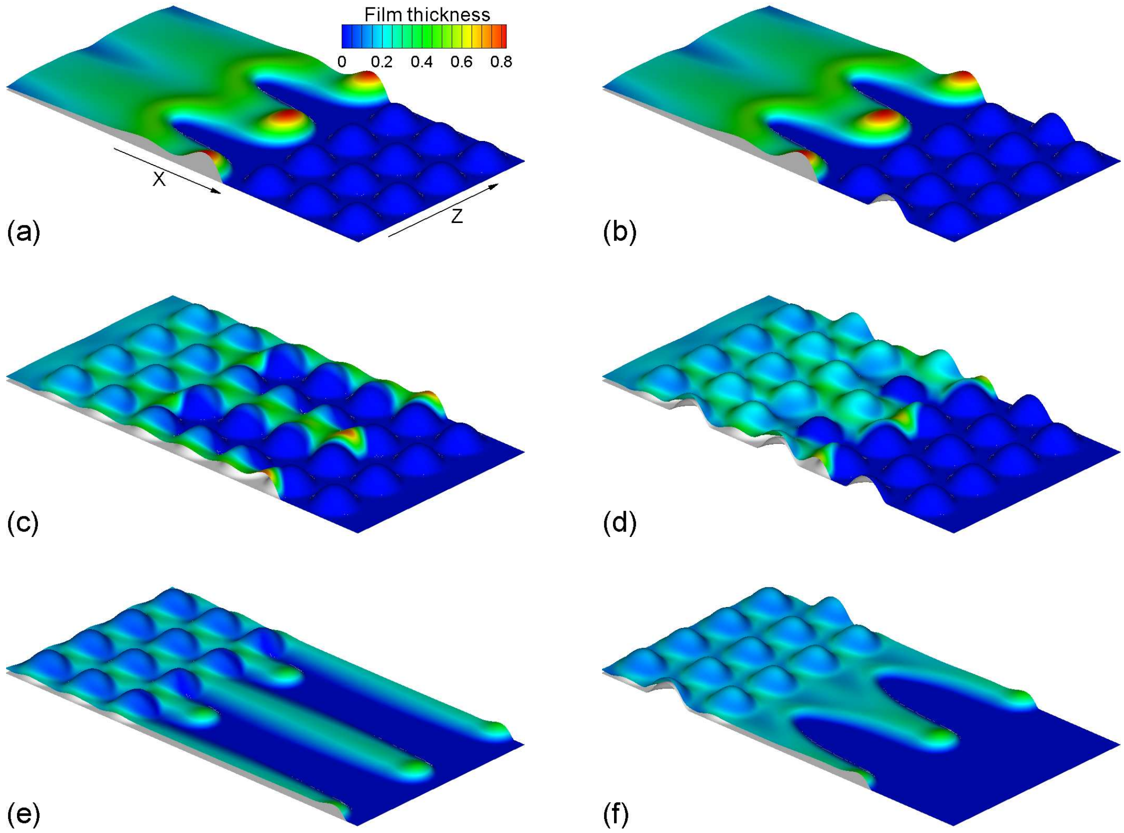

Figure 2.5 Water beads driven by air shear stress through wetted roughness fields. The water flows through an aligned roughness field at (a) $T = 10$, (c) $T = 24$, and (e) $T = 50$, and through an offset roughness field at (b) $T = 10$, (d) $T = 24$, and (f) $T = 50$. The direction of water flow and air shear is from upper left to lower right. Note that the dimension of these figures in the Z-direction is $(-4, 4)$, and in the X-direction it is $(5, 21)$ for (a) and (b), $(14, 30)$ for (c) and (d), and $(23, 39)$ for (e) and (f).

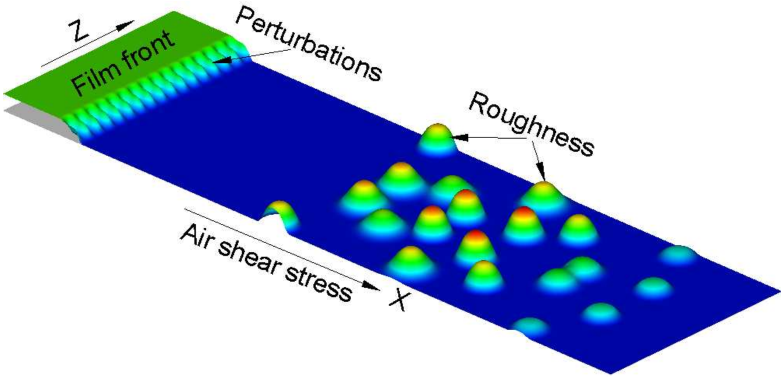

(a) *3D view*

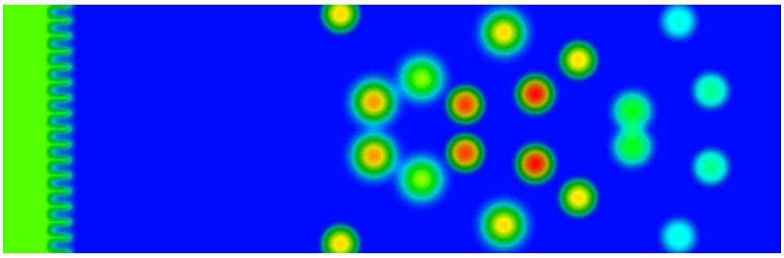

(b) *Top view*

Figure 2.6 Initial conditions for a film front with spanwise perturbations driven by the air shear stress through an irregular roughness field. Note that the dimension of these figures in the Z-direction is $(-4, 4)$, and in the X-direction it is $(-2, 25)$.

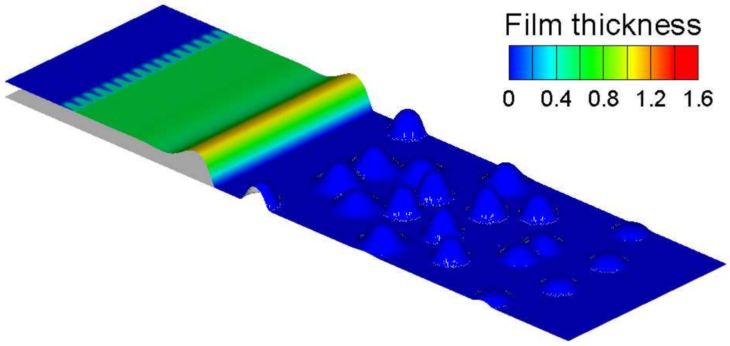

(a) $T = 5$

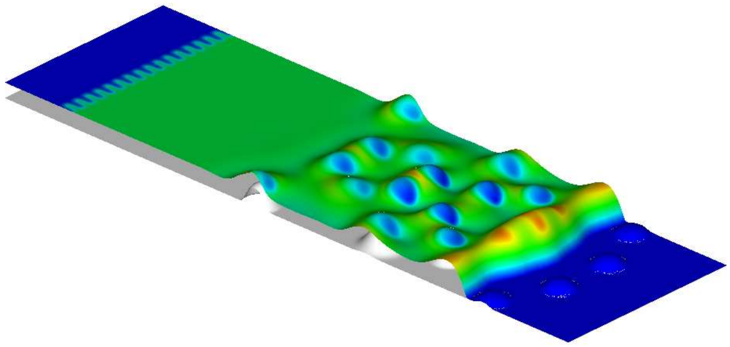

(b) $T = 12.5$

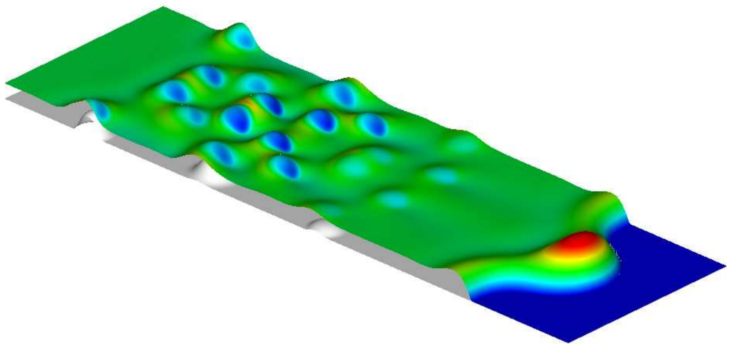

(c) $T = 20$

Figure 2.7 Typical solution of the perturbed film fronts driven by the air shear stress through wetted irregular roughness fields. The film thickness contours are at (a) $T = 5$, (b) $T = 12.5$, and (c) $T = 20$. Note that the dimension of these figures in the Z-direction is $(-4, 4)$, and in the X-direction it is $(-2, 25)$ for (a) and (b), $(6, 33)$ for (c).

As shown in the above cases, beads driven by the air shear stress through a roughness field have formed rivulets. When film fronts are driven by air over a flat surface, the film fronts will be stable if the wavelength of a spanwise perturbation is smaller than a critical value, otherwise the film fronts will be unstable (see chapter 3 and Wang & Rothmayer (2005, 2007)). A more complex example of rivulet formation occurs when a perturbed film front moves through an irregular roughness field. As shown in figure 2.6, a film front with small wavelength perturbation is driven by the air shear stress $\lambda = 2$ with the upstream film thickness h = 0.61 and the downstream film thickness $\delta = 0.01$. The color corresponds to the film thickness. At $T = 5$, the initial perturbation to the film front dies out and the film front becomes a two-dimensional soliton, as shown in figure 2.7(a). The soliton moves forward at a constant speed and has a fixed shape (see chapter 3 and Wang & Rothmayer (2005, 2007)). When the film front arrives at the irregular roughness field, as shown in figure 2.7(b), the film front is disturbed due to the interaction with the roughness elements. As shown in figure 2.7(c), a rivulet is formed when the film front passes through the roughness field.

2.3.2 Heat transfer of water films and beads flowing through roughness fields

As water films and large beads flow through the roughness fields shown in figures 2.4(a) and 2.4(b), the ambient leading order boundary layer scaled heat flux q in the air is $O\left(1\right)$. The height scale of (2.6) and (2.14) is less than that of the air condensed layer (i.e. $Re^{1/4}\sigma^{-1/2}\Delta^{3/2} \ll Re^{-1/2}\Delta^{1/3}$ when $\Delta \ll Re^{-9/14}\sigma^{-3/7}$). This means that the heat flux and temperature are small perturbations on local boundary layer values, as given by (2.8), (2.12), (2.20) and (2.27). In air, the governing equations (2.16-2.20) are quasi-steady, and they are solved at each time step after the water film surface has been updated. A finite difference scheme and block tri-diagonal method are used to solve these equations after they are simplified using the Smith (1983) transformation.

Figure 2.8 is the top view of the perturbed heat flux $\widehat{q}_{air} = \partial\widehat{\vartheta}/\partial\widehat{Y}$ on the water surface shown in figure 2.5 (Note that the perturbed water heat flux is proportional to the perturbed air heat flux). Figures 2.8(a,c,e) show the perturbed heat flux $\hat{q}_{air}$ when the ambient leading order heat flux is $q = -1$, where the air/water interfaces are those shown in figures 2.5(a,c,e) respectively. Figures 2.8(b,d,f) show $\hat{q}_{air}$ when $q = 1$, where the air/water interfaces are those shown in figures 2.5(b,d,f) respectively. In figure 2.8, the red regions are the positively perturbed heat flux, i.e. $\hat{q}_{air} > 0$. In other words, the red regions are heated. The blue regions are the negatively perturbed heat flux, i.e. $\hat{q}_{air} < 0$, and these regions are cooled. The green regions are where the perturbed heat flux is almost zero, in other words the heat flux in these regions is the same as the surface without roughness. These figures show that the ambient heat flux is enhanced at the top of the water and roughness protuberances, and the ambient heat flux is suppressed around the edges of roughness and water features.

Figures 2.9(a, b, c) show the top view of the perturbed heat flux $\hat{q}_{air}$ on the water on water surface shown in figure 2.7 with $q = -1$. The perturbed heat flux $\hat{q}_{air}$ is zero at the green regions, while it is lower to -0.5 at the water protuberances and roughness peaks and it is up to 0.7 at their feet.

2.4 Limit solutions

Two limit solutions are considered in order to verify the accuracy of the numerical scheme used to solve the lubrication equation. Both limit solutions are given in terms of the rescaled variables, $F = hf$, $F_{ice} = h_{ice} f_{ice}$, $\tau = h^3/3T$, $\Lambda = 3\lambda/\left(2h^2\right)$, and $H = h_{ice}/h$, where h is the initial uniform film thickness and h_{ice} is the maximum height of roughness elements on the wall. Using these variables, the film equation (2.32) becomes

$$\frac{\partial f}{\partial \tau} + \frac{\partial}{\partial X}\left(\Lambda f^2 - \frac{\partial p}{\partial X} f^3\right) + \frac{\partial}{\partial Z}\left(-\frac{\partial p}{\partial Z} f^3\right) = 0, \tag{2.35}$$

where

$$p = -\left[\frac{\partial^2 f}{\partial Z^2} + \frac{\partial^2 f}{\partial Z^2} + H\left(\frac{\partial^2 f_{ice}}{\partial Z^2} + \frac{\partial^2 f_{ice}}{\partial Z^2}\right)\right]. \tag{2.36}$$

The spanwise boundary condition is periodic and the streamwise boundary condition is

$$f = 1 \quad \text{and} \quad \partial f/\partial X = 0 \quad \text{as } X \to \pm\infty\ . \tag{2.37}$$

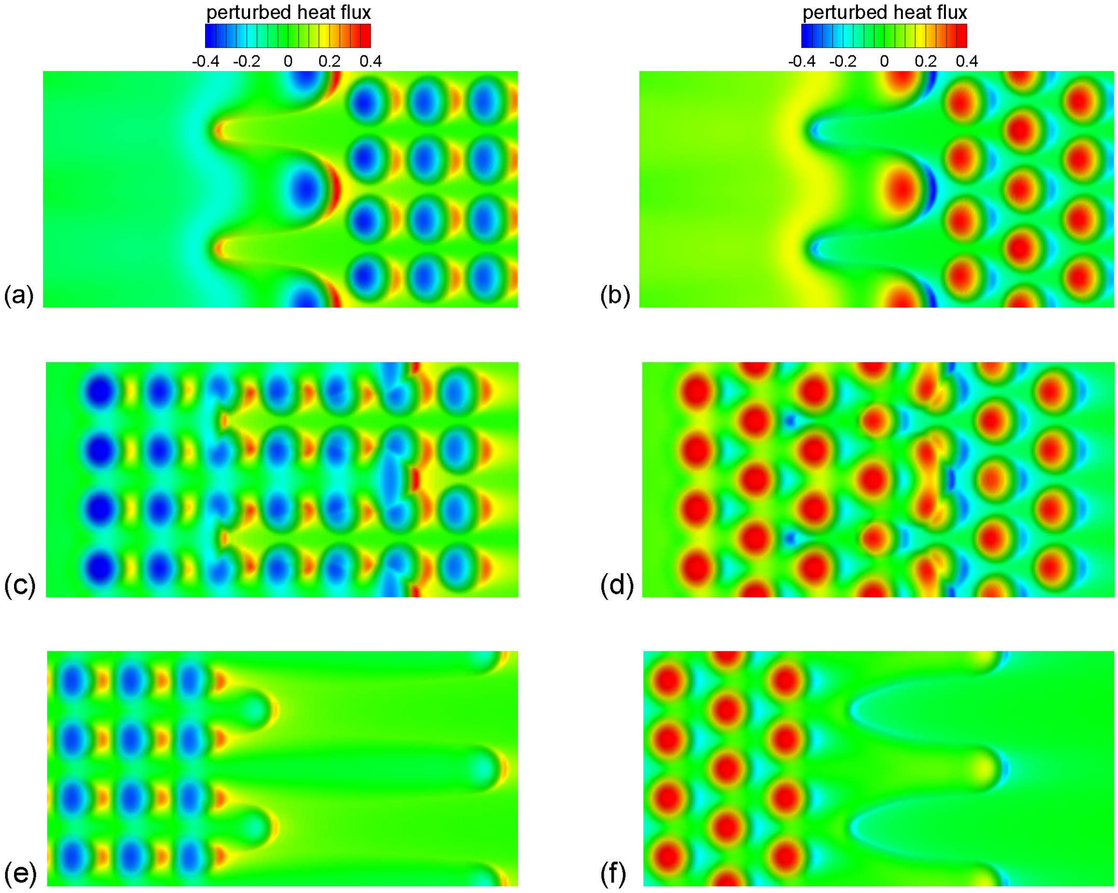

Figure 2.8 Typical perturbed heat flux $\hat{q}_{air}$ when the large beads of figure 2.4 are driven by air shear stress through wetted roughness fields. The water flows through an aligned roughness field with $q = -1$ at (a) $T = 10$, (c) $T = 24$, and (e) $T = 50$, and through an offset roughness field with $q = +1$ at (b) $T = 10$, (d) $T = 24$, and (f) $T = 50$. Note that the coordinates and dimensions of these figures are the same as those in figure 2.5.

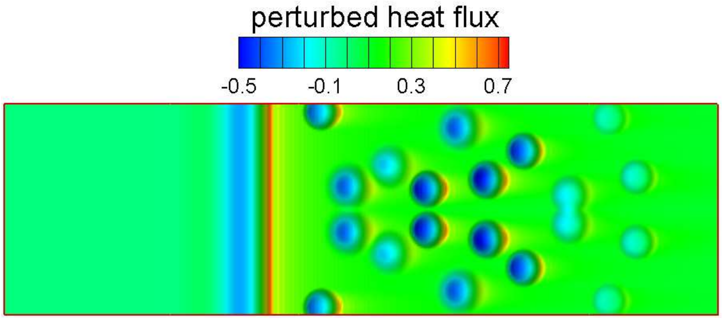

(a) $T = 5$

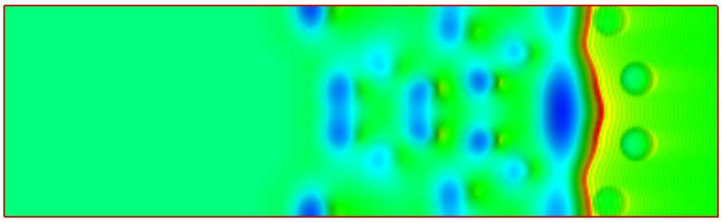

(b) $T = 12.5$

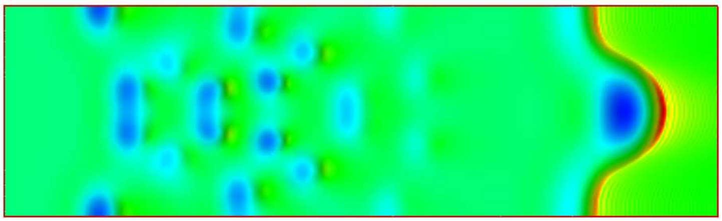

(c) $T = 20$

Figure 2.9 Typical contours of the perturbed heat flux $\hat{q}_{air}$ when the perturbed film fronts are driven by air shear stress through wetted irregular roughness fields when the ambient heat flux is $q = -1$ in the air. The contours of the perturbed heat flux are at (a) $T = 5$, (b) $T = 12.5$, and (c) $T = 20$. Note that the coordinates and dimensions of these figures are the same as those in figure 2.7.

2.4.1 Limit of small heights

In this limit, the roughness height h_{ice} and uniform film thickness h both become much smaller than the roughness diameter (i.e. $h \to 0$ and $h_{ice} \to 0$), and the roughness height ratio also becomes small, i.e. $H = h_{ice}/h \to 0$. The expansions for film thickness and pressure are given by

$$f \sim 1 + H\hat{f} + \cdots, \qquad p \sim H\hat{p} + \cdots, \tag{2.38a,b}$$

and the perturbations $\hat{f}$ and $\hat{p}$ satisfy the following equations

$$\frac{\partial \hat{f}}{\partial \tau} + \frac{\partial}{\partial X}\left(2\Lambda \hat{f} - \frac{\partial \hat{p}}{\partial X}\right) + \frac{\partial}{\partial Z}\left(-\frac{\partial \hat{p}}{\partial Z}\right) = 0 \tag{2.39}$$

and

$$\hat{p} = -\left(\frac{\partial^2 \hat{f}}{\partial X^2} + \frac{\partial^2 \hat{f}}{\partial Z^2} + \frac{\partial^2 \hat{f}_{ice}}{\partial X^2} + \frac{\partial^2 \hat{f}_{ice}}{\partial Z^2}\right). \tag{2.40}$$

Comparisons between this limit solution and solutions of equations (2.35) and (2.36) with $\Lambda = 1.5$ for different small values of H are shown in figure 2.10, where the three dashed lines are the solutions of (2.35) and (2.36), while the symbols (o) and solid lines are calculated from the equations (2.39) and (2.40) using both a finite difference and spectral method (see Canuto, Hussaini, Quarteroni & Zang 1988). It is clear that the solutions of (2.35) and (2.36) approach the limit solutions of (2.39) and (2.40).

When small beads are placed on a wetted flat plate, i.e. $f_{ice} = 0$, a similar solution may be found. In this situation the controlling parameter is the ratio of bead height h_{bead} and film thickness h, i.e. $H_b = h_{bead}/h \to 0$. Using the same expansions as (2.38a,b), but with H replaced by H_b, the limit equation is (2.39) but with the pressure term (2.40) replaced by

$$\hat{p} = -\left(\frac{\partial^2 \hat{f}}{\partial X^2} + \frac{\partial^2 \hat{f}}{\partial Z^2}\right). \tag{2.41}$$

Comparisons between this limit solution and solutions of (2.35) and (2.36) for different small H_b with shear stress parameter $\Lambda = 1.5$ are shown in figure 2.11, where the dashed lines are calculated from (2.35) and (2.36) while the symbols (o) and solid line are calculated from equations (2.39) and (2.41). Again, figure 2.11 shows that the solutions of (2.35) and (2.36) approach the limit solution of (2.39) and (2.41).

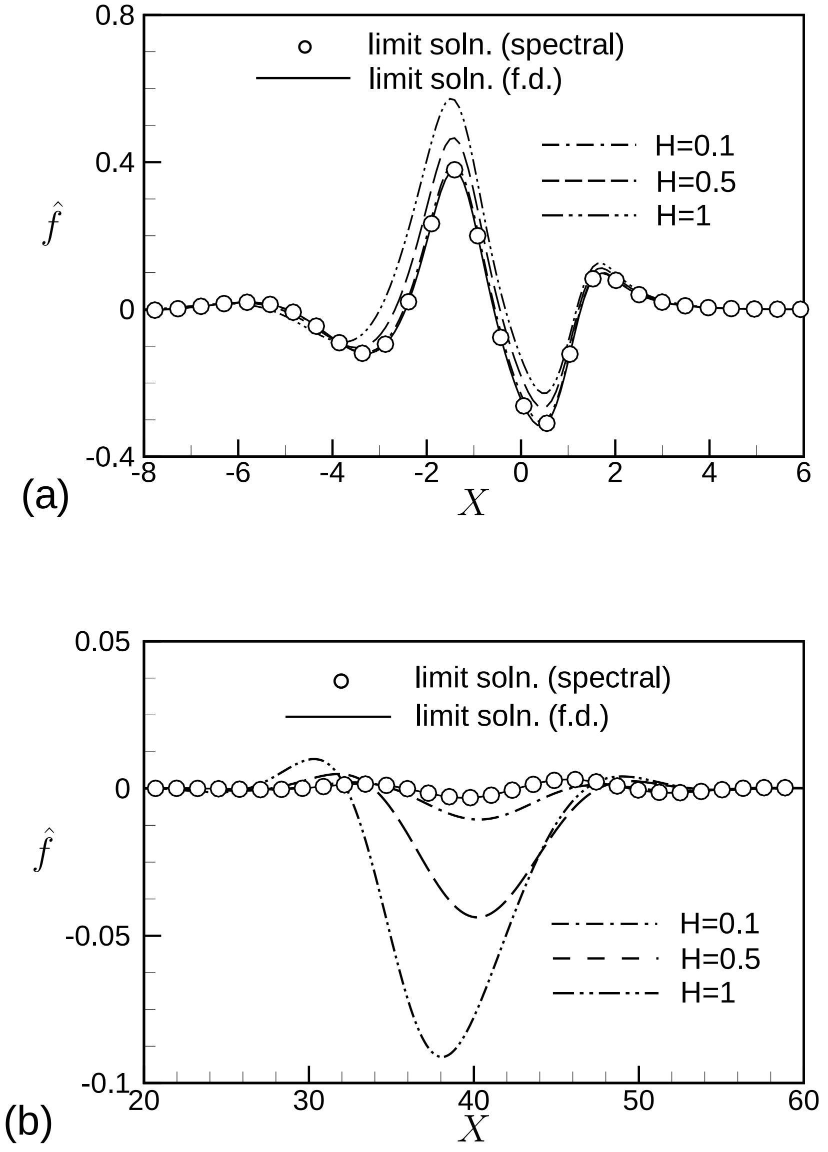

Figure 2.10 Comparison between computed solutions of (2.35) and (2.36) and the limit solution of (2.39) and (2.40) at $\tau \simeq 14.4$. (a) Solutions for the film near a roughness element which has $N = 2$ in (2.33). The values of H approaching the limit solutions are: $H = 1,\ 0.5,\ 0.1$. (b) Solutions for the traveling wave far downstream of the roughness for the same conditions as figure 2.10(a).

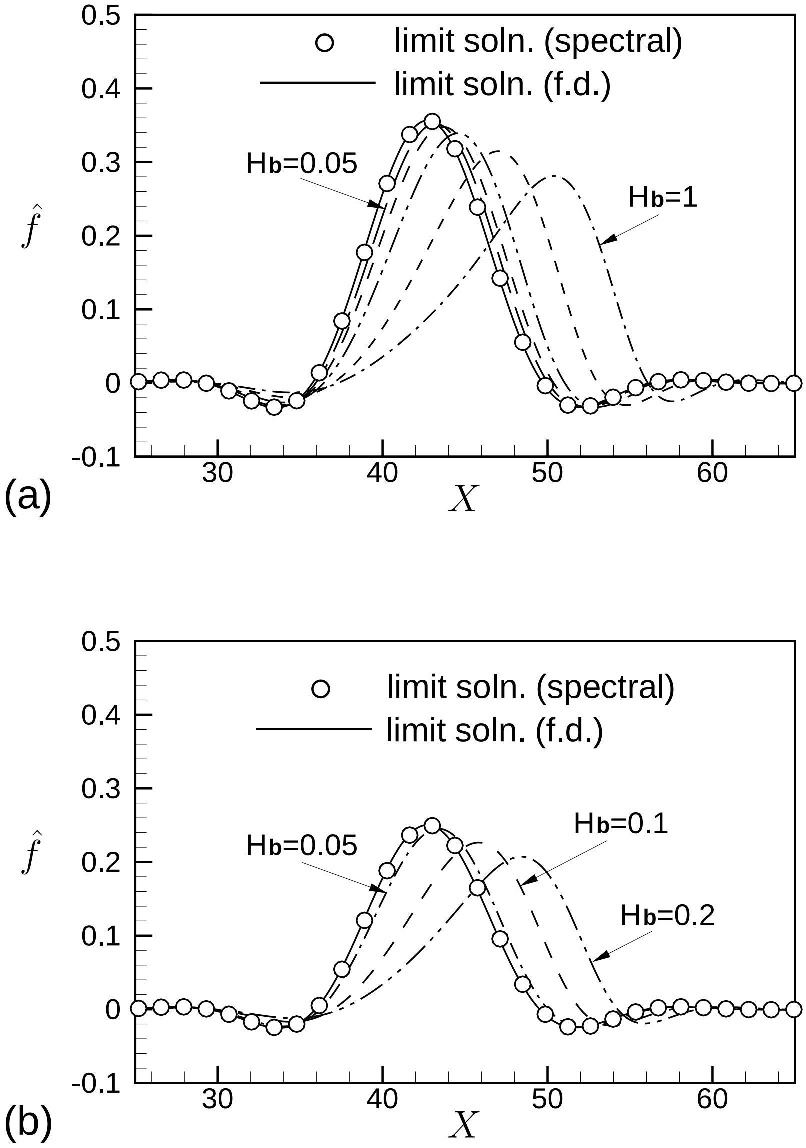

Figure 2.11 Comparison between computed solutions of (2.35) and (2.36) and the limit solution of (2.39) and (2.41) for a moving water bead at $\tau \simeq 14.4$. (a) Solutions when the initial bead shape has $N = 1$ in (2.33). The values of H_b approaching the limit solution are: $H_b = 1,\ 0.5,\ 0.2,\ 0.1,\ 0.05$. (b) Solutions when the initial bead shape has $N = 4$ in (2.33). The values of H_b approaching the limit solutions are: $H_b = 0.2,\ 0.1,\ 0.05$.

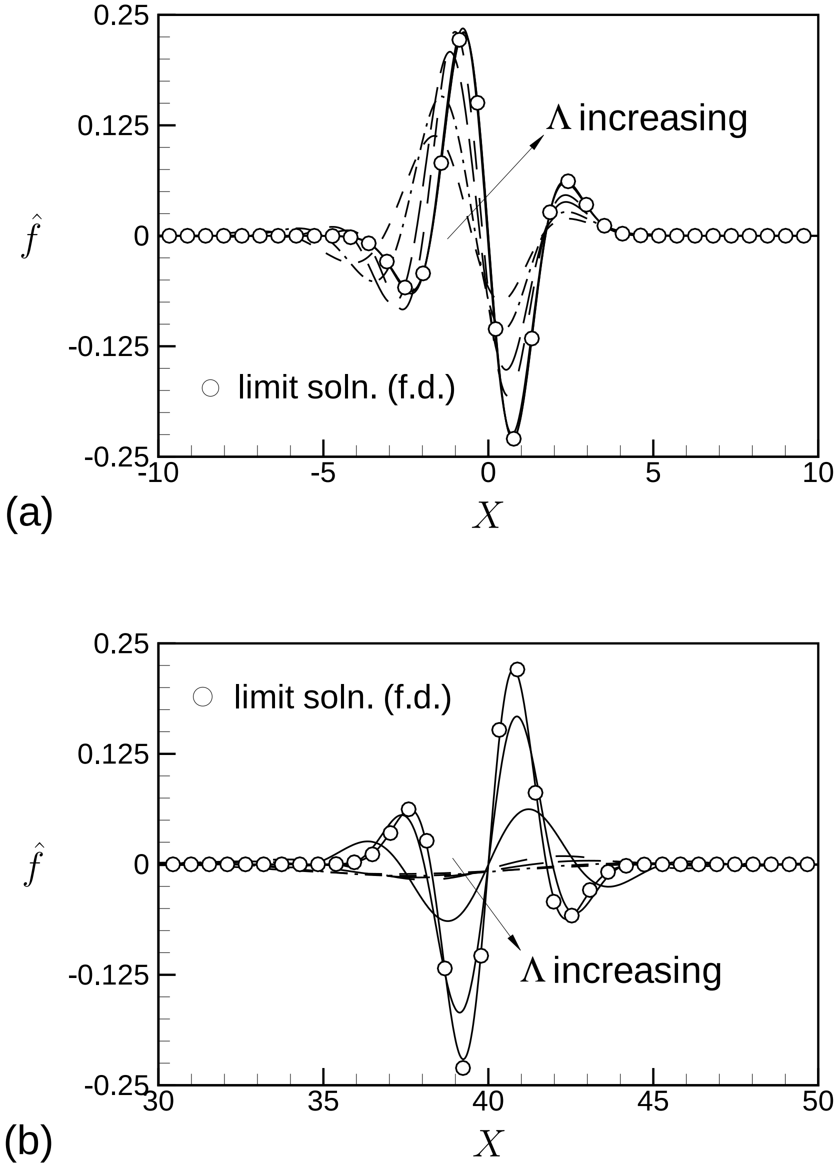

Figure 2.12 Comparison between computed solutions of (2.35) and (2.36) and the limit solution of (2.43) and (2.44) as $\Lambda \to \infty$ at $\hat{t} = 20$. (a) The film near the roughness with $N = 1$ in (2.33). The values of Λ approaching the limit solutions are: $\Lambda = 1,\ 2,\ 5,\ 10,\ 10^2,\ 10^3,\ 10^4$. (b) The traveling wave far downstream of the roughness for the same conditions as figure 2.12(a).

2.4.2 Limit of large shear stress

The second limit solution is when the normalized air shear stress Λ becomes large, i.e. $\Lambda = 3\lambda/\left(2h^2\right) \rightarrow \infty$. The film thickness and pressure are given by

$$f \sim 1 + \Lambda^{-1}\hat{f} + \cdots , \qquad p \sim \hat{p}_0 + \Lambda^{-1}\hat{p}_1 + \cdots , \tag{2.42a,b}$$

where $\hat{f}$ and $\hat{p}_0$ satisfy the following equations

$$\frac{\partial \hat{f}}{\partial \hat{t}} + 2\frac{\partial \hat{f}}{\partial X} = \left(\frac{\partial^2 \hat{p}_0}{\partial X^2} + \frac{\partial^2 \hat{p}_0}{\partial Z^2}\right) \tag{2.43}$$

and

$$\hat{p}_0 = -H\left(\frac{\partial^2 \hat{f}_{ice}}{\partial X^2} + \frac{\partial^2 \hat{f}_{ice}}{\partial Z^2}\right), \tag{2.44}$$

with the scaled time $\tau = \Lambda^{-1}\hat{t}$. A comparison between the solution of equations (2.43) and (2.44) and solutions of (2.35) and (2.36) is shown in figures 2.12(a) and 2.12(b). The symbols (o) are the solution of (2.43) and (2.44), while the dashed or solid lines are calculated from (2.35) and (2.36). Figure 2.12(a) shows that the solutions around the roughness for different large shear stress Λ and $H = 0.5$ are similar to those shown previously. In both figures 2.12(a) and 2.12(b), the solutions of (2.35) and (2.36) approach the limit solution of (2.43) and (2.44) as the parameter $\Lambda \rightarrow \infty$.

2.5 Some additional details for the solutions of the limit equations

2.5.1 An analytical solution of perturbed film equations as $\Lambda \rightarrow \infty$

As the air shear stress goes to infinity, i.e. $\Lambda \rightarrow \infty$, the limit solution of the film equation is discussed in section 2.4. A brief discussion of this analytical solution is given below. For simplicity, equations (2.43) and (2.44) in two-dimensional situations is considered here, i.e.

$$\frac{\partial f}{\partial t} + 2\frac{\partial f}{\partial x} = B - \frac{\partial^4 f_r}{\partial x^4}, \tag{2.45}$$

where the boundary condition is $f\left(+\infty,\, t\right) = f\left(-\infty,\, t\right) = 1$, f_r is the roughness surface which is a function of x, and B is an additional constant added to model the nondimensional mass deposition rate.

According to the properties of equation (2.45) and numerical solutions shown in figure 2.10, the exact solution is assumed to consist of a steady component and a unsteady component, i.e.

$$f(x,\, t) = 1 + s(x) + u(x,\, t)\,, \tag{2.46}$$

where $s(x)$ is the steady solution of thin films around the surface roughness, and $u(x,\, t)$ is composed of the traveling waves on the film surface, which are generated by the interaction between the surface roughness and the free water surface. From the boundary conditions of equation (2.45), it is easy to show that

$$u(+\infty,\, t) = u(-\infty,\, t) = 0 \quad \text{and} \quad s(+\infty) = s(-\infty) = 0. \tag{2.47a,b}$$

Equation (2.46) is substituted into equation (2.45), and the governing equation of the traveling wave becomes

$$\frac{\partial u}{\partial t} + 2\frac{\partial u}{\partial x} = B, \tag{2.48}$$

with the boundary conditions $u(+\infty,\, t) = u(-\infty,\, t) = 0$ and the initial conditions $u(x,\, 0) = f(x,\, 0) - s(x) - 1$, while for the steady solution the equation is

$$2\frac{\partial s}{\partial x} = -\frac{\partial^4 f_r}{\partial x^4}, \tag{2.49}$$

with the boundary conditions $s(+\infty) = s(-\infty) = 0$.

With the relation $U = u - Bt$, the wave equation (2.48) becomes a homogeneous wave equation, i.e.

$$\frac{\partial U}{\partial t} + 2\frac{\partial U}{\partial x} = 0, \tag{2.50}$$

and the classical solution of the wave equation (2.50) is

$$U(x,\, t) = G(x - 2t)\,, \tag{2.51}$$

where $G(\cdot)$ is a function determined by the initial condition $u(x,\, 0)$. Therefore, it is found that

$$u(x,\, t) = G(x - 2t) + Bt. \tag{2.52}$$

Furthermore, the steady solution of equation (2.49) is

$$s = -\frac{1}{2}\frac{\partial^3 f_r}{\partial x^3} + C, \tag{2.53}$$

where $C = 0$ from the boundary conditions. From the equations of the traveling wave and the steady solution, i.e. equations (2.52), (2.53) and the expansion (2.46), the solution of the equation (2.45) is

$$f(x,\, t) = 1 - \frac{1}{2}\frac{\partial^3 f_r}{\partial x^3} + G(x - 2t) + Bt. \tag{2.54}$$

If the initial condition of equation (2.45) is set to be $f(x,\, 0) = g(x)$, the function $G(\cdot)$ becomes

$$G(\cdot) = g(\cdot) + \frac{1}{2}\frac{\partial^3}{\partial x^3}\left[f_r(\cdot)\right] - 1 \tag{2.55}$$

Finally the solution of equation (2.45) is

$$f(x,\, t) = \frac{1}{2}\left\{\frac{\partial^3}{\partial x^3}\left[f_r(x - 2t)\right] - \frac{\partial^3}{\partial x^3}\left[f_r(x)\right]\right\} + g(x - 2t) + Bt, \tag{2.56}$$

where $g(x) = f(x,\, 0)$.

2.5.2 A solution with Fourier series as $H \to 0$

The numerical solutions as $H \to 0$ have been discussed in section 2.4. A discussion of one solution using Fourier series is given below. For simplicity, equations (2.39) and (2.40) in two-dimensions is considered here, i.e.

$$\frac{\partial f}{\partial t} + 2\Lambda\frac{\partial f}{\partial x} + \frac{\partial^4 f}{\partial x^4} = B - \frac{\partial^4 f_r}{\partial x^4}, \tag{2.57}$$

where the boundary condition is $f(+\infty,\, t) = f(-\infty,\, t) = 1$, f_r is again the roughness surface which is a function of x, and B is again a constant parameter used to model the nondimensional mass deposition rate.

Similarly, the perturbed film thickness f is written as

$$f(x,\, t) = 1 + s(x) + u(x,\, t), \tag{2.58}$$

where the boundary conditions of the unsteady component $u(x,\, t)$ and the steady component $s(x)$ are

$$u(+\infty,\, t) = u(-\infty,\, t) = 0 \quad \text{and} \quad s(+\infty) = s(-\infty) = 0. \tag{2.59a,b}$$

With the substitution of equation (2.58) into equation (2.57), the governing equation of the unsteady component $u\,(x,\,t)$ becomes

$$\frac{\partial u}{\partial t}+2\Lambda\frac{\partial u}{\partial x}+\frac{\partial^4 u}{\partial x^4}=B, \tag{2.60}$$

with the boundary conditions $u\,(+\infty,\,t)=u\,(-\infty,\,t)=0$ and the initial condition $u\,(x,\,0)=f\,(x,\,0)-s\,(x)-1$. For the steady component $s\,(x)$, the equation is

$$2\Lambda\frac{\partial s}{\partial x}+\frac{\partial^4 s}{\partial x^4}=-\frac{\partial^4 f_r}{\partial x^4}, \tag{2.61}$$

with the boundary conditions $s\,(+\infty)=s\,(-\infty)=0$.

Similarly, with the relation $U=u-Bt$, the wave equation (2.60) is rewritten as

$$\frac{\partial U}{\partial t}+2\Lambda\frac{\partial U}{\partial x}+\frac{\partial^4 U}{\partial x^4}=0. \tag{2.62}$$

With the Fourier expansion of the variable U, i.e.

$$U\,(x,\,t)=\sum_{n=-\infty}^{+\infty}a_n\,(t)\cdot\exp\,(i\alpha_n x)\,, \tag{2.63}$$

equation (2.62) becomes

$$\frac{da_n\,(t)}{dt}+\left(i\alpha_n 2\Lambda+\alpha_n^4\right)\cdot a_n\,(t)=0. \tag{2.64}$$

Finally, the solution of equation (2.62) is

$$U\,(x,\,t)=\sum_{n=-\infty}^{+\infty}C_n\cdot\exp\left(-\alpha_n^4 t\right)\cdot\exp\left[i\alpha_n\,(x-2\Lambda t)\right], \tag{2.65}$$

where the Fourier coefficients C_n are calculated from the initial boundary conditions $u\,(x,\,0)=g\,(x)$, i.e.

$$C_n=\sum_{n=-\infty}^{+\infty}g\,(x)\cdot\exp\,(-i\alpha_n x)\,. \tag{2.66}$$

Using Fourier series for the steady solution $s\,(x)$ and the roughness surface f_r, i.e.

$$s\,(x)=\sum_{n=-\infty}^{+\infty}b_n\cdot\exp\,(i\alpha_n x) \tag{2.67}$$

and

$$f_r\,(x)=\sum_{n=-\infty}^{+\infty}f_{rn}\cdot\exp\,(i\alpha_n x)\,, \tag{2.68}$$

the steady equation (2.60) becomes

$$i\alpha_n 2\Lambda b_n + (i\alpha_n)^4 b_n = -(i\alpha_n)^4 f_{rn}. \tag{2.69}$$

Finally, Fourier coefficients b_n in the steady solution $s(x)$ are

$$b_n = -\frac{\alpha_n^3 f_{rn}}{i2\Lambda + \alpha_n^3}. \tag{2.70}$$

Therefore, the solution of the equation (2.57) with Fourier transformation is

$$f(x,\, t) = 1 + s(x) + u(x,\, t), \tag{2.71}$$

with

$$s(x) = \sum_{n=-\infty}^{+\infty} \left\{ -\frac{\alpha_n^3 f_{rn}}{i2\Lambda + \alpha_n^3} \cdot \exp(i\alpha_n x) \right\} \tag{2.72}$$

and

$$u(x,\, t) = Bt + \sum_{n=-\infty}^{+\infty} \left\{ C_n \cdot \exp\left(-\alpha_n^4 t\right) \cdot \exp\left[i\alpha_n (x - 2\Lambda t)\right] \right\}, \tag{2.73}$$

where C_n and f_{rn} are given by equations (2.66) and (2.68), respectively.

The same method can be applied to the limit solution of a bead as $H_b \to 0$. The difference is that the steady solution is zero and the unsteady solution is completely determined by the initial conditions.

CHAPTER 3. Stability of film fronts

3.1 Problem formulation

A number of studies of have considered the stability of two-dimensional film fronts to three-dimensional disturbances. The experiments by Huppert (1982) and Cazabat *et al.* (1990) examined the instability of film fronts on inclined or vertical plates when the film was driven by gravity and Marangoni forces respectively. Brzoska, Brochard-Wyart & Rondelez (1992) considered a film driven by Marangoni forces on a horizontal plate, and concluded from experimental data that the width of the rim near the contact line plays a crucial role in the onset of the film front instability. Cazabat *et al.* (1992) and Kataoka & Troian (1997) also performed a linear stability analysis of a film front driven by Marangoni forces and gravity. For the films simply driven by the gravity, de Bruyn (1992) experimentally measured the unsteady film rivulet lengths and calculated the temporal growth when the films formed on inclined glass surface with small inclination angles, i.e. between 2^o and 21^o. Brenner (1993) estimated the temporal growth rate and the largest wavelength when the unstable film fronts were driven by gravity over an inclined surface. Experiments by Johnson et al. (1999) showed the instabilities of film fronts on inclined surfaces with a rang of inclination angles, i.e. between 7.2^o and 90^o. Diez & Kondic (2001) presented the numerical results of unstable film fronts.

In order to perform a stability analysis for shear driven films, the film equation (2.32) is first renormalized so that the upstream film thickness is 1 and the downstream film thickness is δ, which results in the equations (2.35) and (2.36). That is, a smooth jump exists in the initial film thickness along the flow direction. The region over which this height change occurs is the film front. The flow is assumed to be periodic in the spanwise direction, and the streamwise boundary conditions are taken to be

$$\left.\begin{array}{llll} X=-\infty: & f=1 & \text{and} & \partial f/\partial X=0 \\ X=\infty: & f=\delta & \text{and} & \partial f/\partial X=0 \end{array}\right\}. \tag{3.1}$$

The following section considers the three-dimensional stability of two-dimensional solitons of (2.35) and (2.36).

3.2 Solitons

In two-dimensions, the governing equations (2.35) and (2.36) can be simplified to give

$$\frac{\partial f}{\partial \tau}+\frac{\partial}{\partial X}\left(\Lambda f^2+\frac{\partial^3 f}{\partial X^3}f^3\right)=0. \tag{3.2}$$

The streamwise boundary conditions are given by the equation (3.1). If this two-dimensional film front is observed in a moving coordinate frame which has speed c, i.e.

$$\xi=x-c\tau, \tag{3.3}$$

and using $f\left(X,\tau\right)=g_0\left(\xi\right)$, then the two-dimensional film equation (3.2) becomes

$$\frac{\partial}{\partial \xi}\left[-cg_0+\Lambda g_0^2+g_0^3\frac{\partial^3 g_0}{\partial \xi^3}\right]=0, \tag{3.4}$$

and the boundary conditions (3.1) become

$$\left.\begin{array}{llll} \xi=-\infty: g_0=1 & & \text{and} & \partial g_0/\partial \xi=0 \\ \xi=\infty: & g_0=\delta & \text{and} & \partial g_0/\partial \xi=0 \end{array}\right\}. \tag{3.5}$$

Again, δ is an imposed jump discontinuity in the film thickness which is smoothed out within the soliton. Applying the boundary condition (3.5) to equation (3.4) after integration yields the wavespeed

$$c=\Lambda\left(1+\delta\right). \tag{3.6}$$

The wavespeed (3.6) is similar to the one found by Kataoka & Troian (1997). A fourth order Runge-Kutta method is used to solve soliton equation (3.4), where a fictitious time derivative of g_0 is added in order to stabilize the numerical solution, i.e.

$$\frac{\partial g_0}{\partial \bar{\tau}}+\frac{\partial}{\partial \xi}\left[-cg_0+\Lambda g_0^2+g_0^3\frac{\partial^3 g_0}{\partial \xi^3}\right]=0, \tag{3.7}$$

where $\bar{\tau}$ is the fictitious time. The boundary conditions are the same as equation (3.5). When the fictitious time $\bar{\tau}$ goes to infinity, i.e. $\bar{\tau} \rightarrow \infty$, the solutions of (3.7) will converge to the exact solutions of (3.4). Typical $\bar{\tau} \rightarrow \infty$ solutions are shown in figure 3.1(b) for the two different initial conditions $g_0(\xi, \bar{\tau} = 0)$ given in figure 3.1(a). The wavespeed is $c = 1.5$, the shear stress parameter is $\Lambda = 1$, the downstream film thickness is $\delta = 0.5$. The solutions of (3.4) stay near $\xi = 0$, while solutions of (2.35) and (2.36) move downstream. In figure 3.1(b) the solutions of (2.35) and (2.36) are shifted by a distance τc in order to make the comparison. Note that the final solutions of (3.4) shown in figure 3.1(b) are independent of the initial conditions shown in figure 3.1(a).

Figure 3.2(a) shows typical solutions of (3.4) with $\Lambda = 1$, when the downstream film thickness varies over the range $\delta = 0.1,\ 0.5,\ 0.9$. Solutions of (3.4) when the shear stress parameter Λ varies over the range $\Lambda = 1,\ 10,\ 100$ are shown in figure 3.2(b), with $\delta = 0.5$. Figures 3.2(a) and 3.2(b) also show comparisons between solutions of (3.4) and numerical solutions of (2.35) and (2.36). Again, the solutions of (2.35) and (2.36) are shifted by a distance τc in order to compare with the soliton solutions. For the different shear stress parameters Λ and downstream thickness parameters δ, there is good agreement between the solutions of (3.4) and the solutions of (2.35) and (2.36).

3.3 Stability analysis

The solitons of (3.4) shown in figure 3.2 are perturbed in the spanwise direction as follows

$$[f,\ p,\ f_{ice}] = [g_0(\xi),\ p_0(\xi),\ 0] + \epsilon\,[g_1(\xi,\tau),\ p_1(\xi,\tau),\ S_{ice}(\xi,\tau)]\, exp\,(i\beta z) + \text{c.c.}, \tag{3.8}$$

where $\epsilon \ll 1$, g_0 is a solution of (3.4) and the pressure is $p_0 = -\partial^2 g_0/\partial \xi^2$. β is the wavenumber in the z-direction (i.e. the direction across the two-dimensional wave front). The spanwise wavelength of the perturbation is $l = 2\pi/\beta$. When equation (3.8) is substituted into (2.35) and (2.36) the perturbations are found to satisfy

$$\frac{\partial g_1}{\partial \tau} + \frac{\partial}{\partial \xi}\left[\left(-c + 2\Lambda g_0 - 3g_0^2 \frac{\partial p_0}{\partial \xi}\right) g_1 - g_0^3 \frac{\partial p_1}{\partial \xi}\right] + \beta^2 g_0^3 p_1 = 0, \tag{3.9}$$

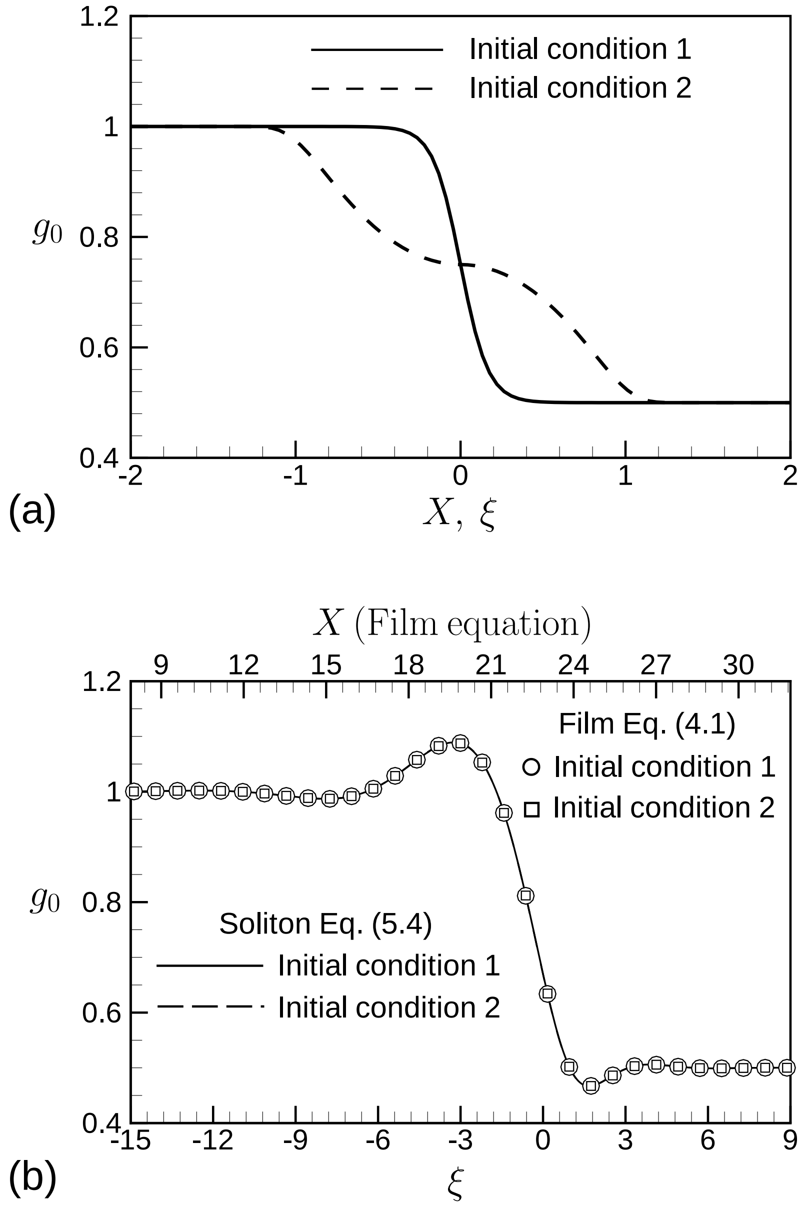

Figure 3.1 Comparisons of solutions of the nonlinear film equations (2.35) and (2.36) and solutions of the soliton equation (3.4). (a) Initial conditions near X = 0 and $\xi = 0$, (b) Solutions of equations (3.4), (2.35) and (2.36) using the initial conditions given in (a), where the solid and dashed lines plotted over each other in (b) are solutions of (3.4); the symbols (O) and (□) are solutions of (2.35) and (2.36) but shifted in X.

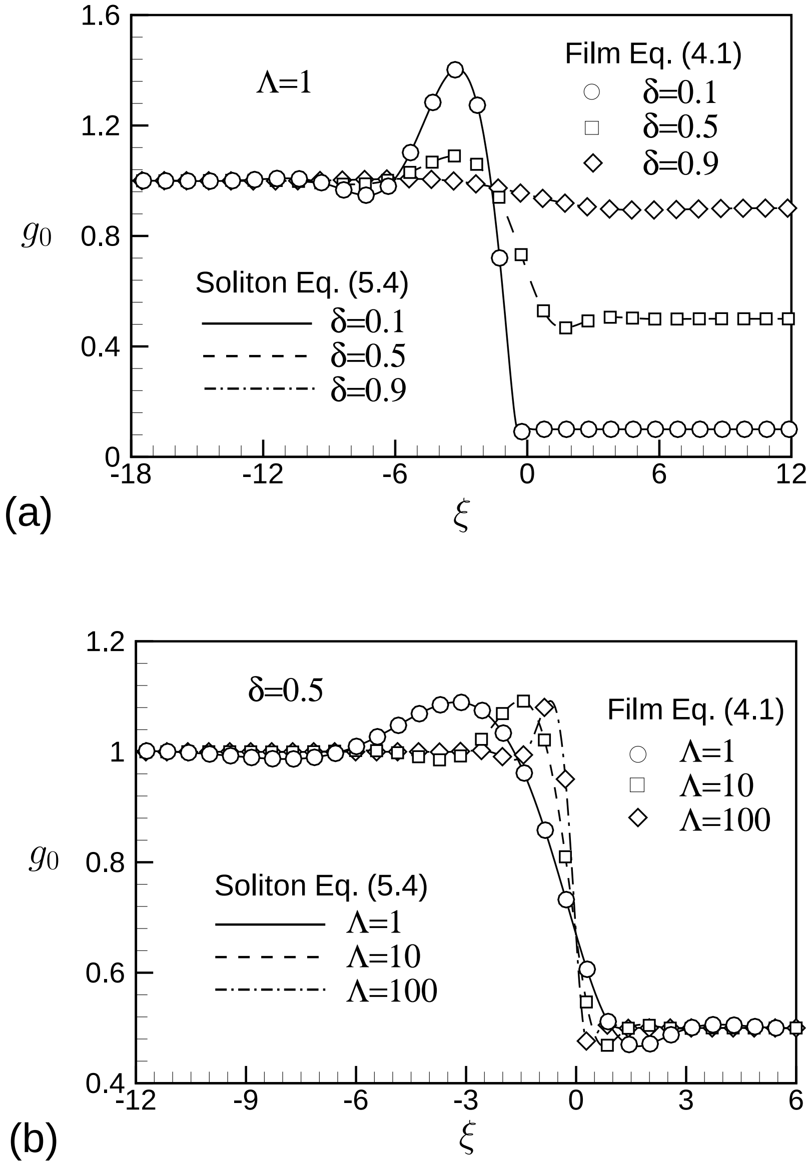

Figure 3.2 Typical solitons for different shear stress parameter Λ and different downstream film thickness parameters δ. In figures (a) and (b), (——, − − − −, − · − · − · −) are solutions of (3.4), while the symbols (O), (□) and (◊) are solutions of (2.35) and (2.36) .

with

$$p_1 = -\left[\frac{\partial^2}{\partial \xi^2}\left(g_1 + HS_{ice}\right) - \beta^2\left(g_1 + HS_{ice}\right)\right]. \tag{3.10}$$

The ice surface roughness can be assumed to be periodic in the spanwise direction with $F_{ice} = S_{ice}(\xi)\, exp\,(i\beta z) + \text{c.c.}$. However, solutions presented here assume that there is no underlying roughness, i.e. $S_{ice} = 0$.

In order to provide an example of the typical behavior encountered in this problem, smooth "perturbations" with different spanwise wavelengths are added to a two-dimensional soliton in figures 3.3(a) and 3.3(c). In the numerical solutions, a periodic boundary condition is applied in the spanwise direction at the same wavelength as the initial spanwise wave front perturbation. The spanwise perturbations are cosine functions, and their streamwise form is given by equation (2.33) or (2.34). Typical solutions of (2.35) and (2.36) with $\Lambda = 78.044$ and $\delta = 0.0323$ are shown in figures 3.3(b) and 3.3(d) (the two solutions arise from the initial conditions shown in figures 3.3(a) and 3.3(c) respectively). The contour variable shown in figures 3.3(b) and 3.3(d) is a film thickness difference, i.e. $f(X, Z, \tau) - f(X, Z, 0)$, where $f(X, Z, 0)$ is the initial condition shown in figures 3.3(a) and 3.3(c) and $f(X, Z, \tau)$ is the solution of (2.35) and (2.36). When the spanwise wavelength of the perturbation is sufficiently small the disturbance decays, as shown in figure 3.3(d). However, for sufficiently large spanwise disturbance wavelength the film front grows into rivulets, as shown in figure 3.3(b).

To establish the critical wavelengths at which rivulets can form, the stability equation (3.9) is solved using a fourth order Runge-Kutta method over a range of shear stress parameters, Λ, and downstream film thickness parameters, δ. Figure 3.4(a) shows four different initial conditions used to calculate the unstable disturbances of (3.9) which are shown in figure 3.4(b). Figure 3.4(b) shows the typical transient evolution of the largest linear perturbation $|\Delta g_1|_{max}(\tau)$, i.e. at a given time τ

$$|\Delta g_1|_{max} = \max_{\xi} |g_1(\xi, \tau) - g_1(\xi, 0)|, \tag{3.11}$$

for unstable disturbances with wavenumber $\beta = 1$, shear stress parameter $\Lambda = 10$ and downstream film thickness parameter $\delta = 0.1$. The temporal growth rates, σ_r, are extracted from

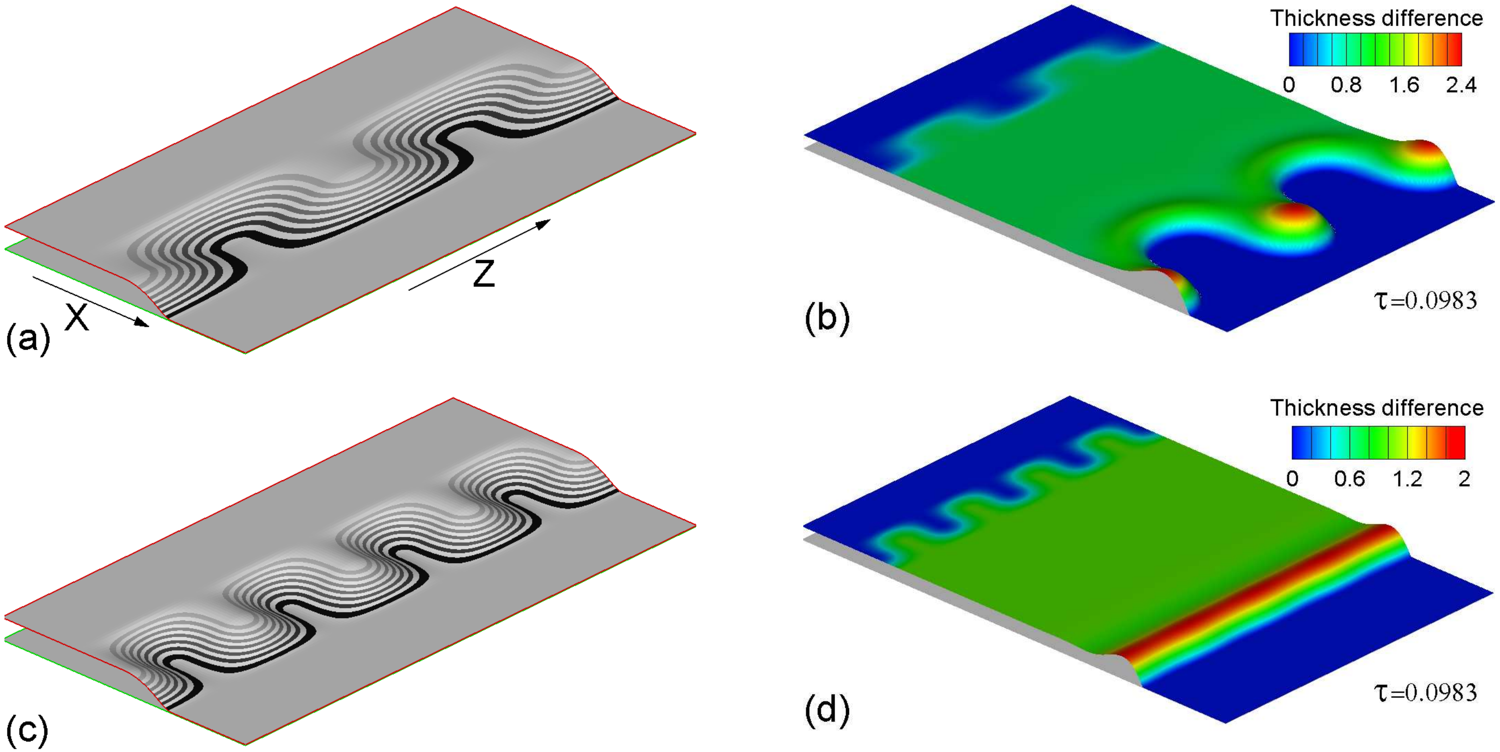

Figure 3.3 Typical solutions of the film front with spanwise perturbations. (a) Initial perturbations of the film front with wavenumber $\beta = \pi/2$, (b) unstable film front resulting from (a) showing the formulation of rivulets, (c) initial perturbations of the film front with wavenumber $\beta = \pi$, (d) stable film front resulting from (c) showing the return to a two-dimensional soliton. Note that the dimension of these figures in the Z-direction is $(-4, 4)$, and in the X-direction it is $(3, 7)$ for (a) and (c), (3,15) for (b) and (d).

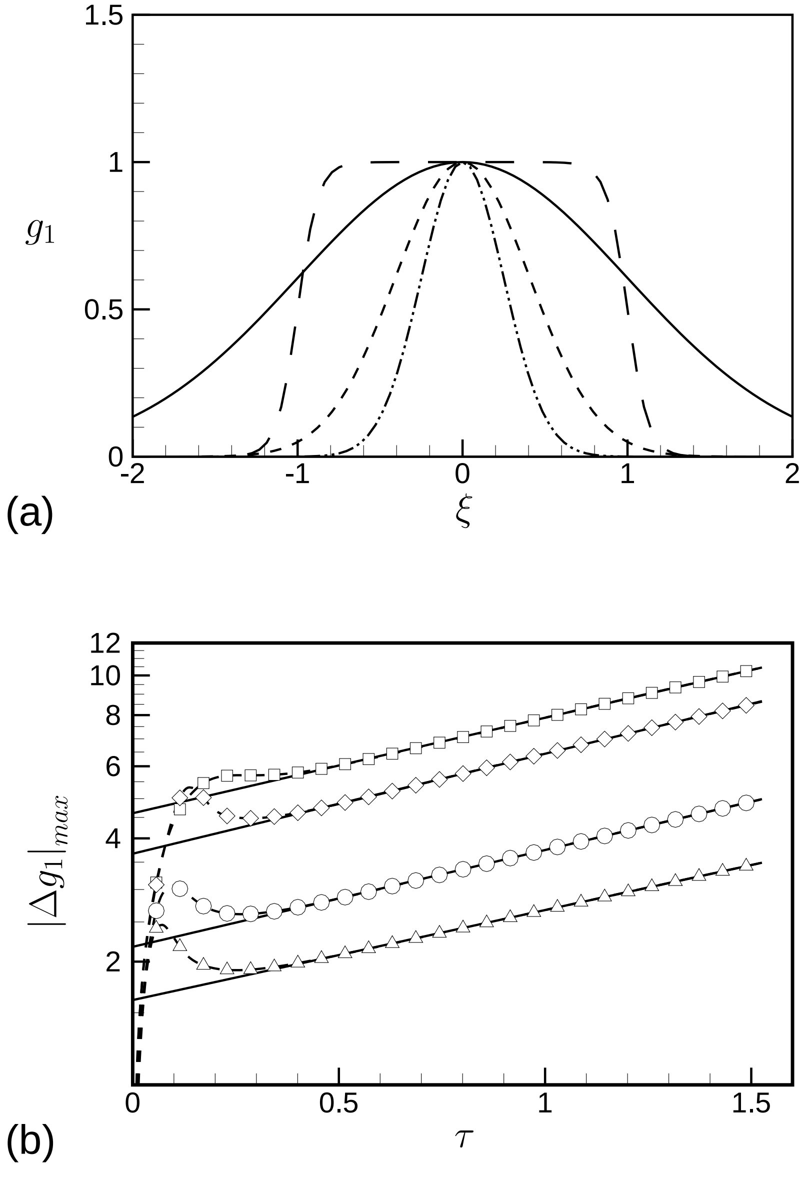

Figure 3.4 Typical time evolution of the perturbation film thickness for unstable disturbances with different initial conditions. (a) Four initial conditions used for equation (3.9), (b) transient solutions resulting from the initial condition of (a). The temporal growth rates, σ_r, are extracted from the slopes of the curves at large time.

the slopes of these curves at large time, i.e.

$$\sigma_r = \lim_{\tau \to \infty} \frac{d}{d\tau} \left(\log_{10} |\Delta g_1|_{max} \right). \tag{3.12}$$

The temporal growth rate σ_r of the four curves shown in figure 3.4(b) are found to be almost the same. For the remaining computations, the initial condition, $g_1(\xi, \tau = 0)$, is taken to be the long dashed line shown in figure 3.4(a).

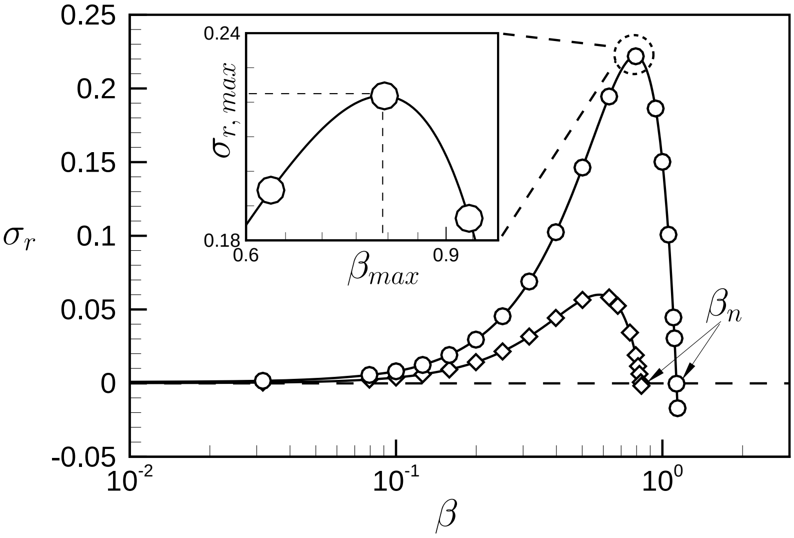

Figure 3.5 Typical temporal growth rate, σ_r, of the linear perturbation plotted against spanwise wavenumber, β. The line with symbols (O) is the solution with $\Lambda = 25.119$ and $\delta = 0.4$, and the line with symbols ($\Diamond$) is the solution with $\Lambda = 10$ and $\delta = 0.4$. The subfigure shows the definitions of the largest temporal growth rate, $\sigma_{r,max}$, and the most unstable wavenumber, β_{max}.

In figure 3.5, the typical temporal growth rate σ_r of the linear perturbation is calculated for different wavenumbers β when the shear stress parameter Λ is 10 and 25.119 with a downstream film thickness parameter $\delta = 0.4$. As the wavenumber β increases, the temporal growth rate σ_r reaches its peak value at the most unstable wavenumber β_{max} shown in figure 3.5. Disturbances at much shorter spanwise wavelength are found to be stable. In subsequent figures, the most unstable wavelength is $l_{max} = 2\pi/\beta_{max}$ and the neutral wavelength is $l_n = 2\pi/\beta_n$, where β_n is the neutral wavenumber shown in figure 3.5.

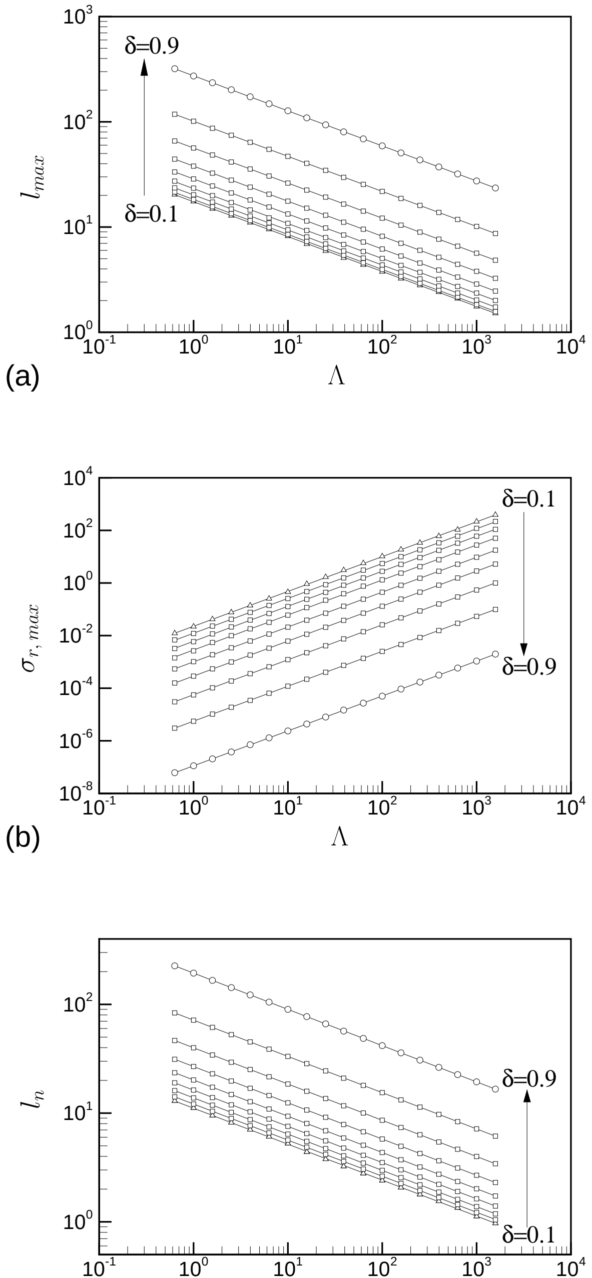

Figure 3.6 (a) The most unstable spanwise wavelength l_{max} and (b) the largest temporal growth rate $\sigma_{r,max}$, and (c) the neutral spanwise wavelength l_n, where the downstream film thickness parameter δ ranges from 0.1 to 0.9. The symbols are the numerically computed data points. The lines are least squares curve fits of the computed solutions.

The most unstable wavelength l_{max}, and the largest temporal growth rate $\sigma_{r,max}$ are plotted against the shear stress parameter Λ in figures 3.6(a,b) with δ ranging from 0.1 to 0.9. In these two figures, the numerically computed data points lie approximately along a straight line for a fixed value of δ, and the slopes of these lines are extracted using a linear least squares curve fit. A general formula which is found to fit the data points is

$$\Phi\left(\delta,\ \Lambda\right) = \psi\left(\delta\right) \cdot \Lambda^{a}, \tag{3.13}$$

where Φ is the variable being fitted, i.e. the most unstable wavelength l_{max}, the neutral wavelength l_n, or the largest temporal growth rate $\sigma_{r,max}$. It is plausible to guess that $\psi\left(\delta\right)$ is a function of the downstream film thickness δ only. A polynomial function of δ is used to complete the curve fit, i.e.

$$\log_{10}\psi\left(\delta\right) = \alpha_0 + \alpha_1\delta + \alpha_2\delta^2 + \alpha_3\delta^3 + \alpha_4\delta^4 + \alpha_5\delta^5, \tag{3.14}$$

where the coefficients α_i and the parameter a of equation (3.13) are given in Table 3.1, and are all calculated using a least squares method. It should be noted that a variety of polynomials were tested for the curve fit (both lower and higher order than equation (3.14)). Comparisons of the final curve fits with the numerically computed data points are shown in figures 3.6(a, b). From equations (3.13) and (3.14) together with the scales given in section 2.2, it is found that the dimensional spanwise wavelength at largest temporal growth rate is given by

$$l^*_{max} = \psi\left(\delta\right) \cdot \left[\frac{3}{2}\frac{\lambda^*}{\left(h^*\right)^2\sigma^*}\right]^{-1/3}, \tag{3.15}$$

where λ^* is the air shear stress, i.e. $\lambda^* = \mu^*\partial u^*/\partial y^*$. In addition, l^*_{max}, σ^*, and h^* are the most unstable spanwise wavelength, the surface tension, and the undisturbed film thickness, respectively. The parameter δ is the ratio of downstream to upstream film thickness.

3.4 Comparison with experimental data

The experiment by Cazabat *et al.* (1990) demonstrated the instability of a film front driven by a constant surface tension gradient, $\tau = \frac{d\gamma}{dx}$, which is induced by temperature gradients along the film surface on a vertical differentially heated flat wall (also see Ludviksson & Lightfoot

Table 3.1 Coefficients in equations (3.13) and (3.14).

	a	α_0	α_1	α_2	α_3	α_4	α_5
l_{max}	$-1/3$	1.19421	0.77073	-4.47281	15.44012	-20.11550	10.35426
$\sigma_{r,max}$	$4/3$	-1.16833	-6.80194	27.63429	-80.05700	98.82053	-48.29411
l_n	$-1/3$	0.98733	0.81263	-3.50422	12.45144	-16.83387	9.10138

(1971)). Though such flows are also termed Marangoni flows (see Levich (1962); Levich & Krylov (1969)), the driving force is equivalent to a surface shear stress driven film (see Eres *et al.* (2000)). Eres *et al.* (2000) derived a film equation where the film is driven by a constant surface tension gradient τ. If the gravity and the substrate velocity is zero, the film equation found by Eres *et al.* (2000) becomes

$$\frac{\partial h}{\partial t} = -\frac{\sigma}{3\mu} \bigtriangledown \cdot \left(h^3 \bigtriangledown \bigtriangledown^2 h\right) - \frac{\tau}{2\mu} \frac{\partial h^2}{\partial x}, \tag{3.16}$$

where h is the film thickness, σ is the surface tension, μ is the viscosity, and τ is the constant surface tension gradient $\tau = \frac{d\gamma}{dx}$. Equation (3.16) is similar to the film equation (2.32) and (2.30), though the types of driving forces are different. When the way shown by Eres *et al.* (2000) is used to derive the shear-driven or Marangoni-force-driven dimensional film equations, such dimensional equations will be in the same form without any differences. The mathematic properties of these two equations are close to each other due to their similarity. Without available experimental data on the instability of air-shear-stress driven films, a comparison with the surface-tension-gradient driven films is shown in Table 3.2, where μ^* is the dimensional viscosity, $\lambda^* = \tau$ is the dimensional surface tension gradient, h^* is the dimensional upstream film thickness, and l^*_{exp} is the dimensional wavelength measured in the experiments (see Cazabat *et al.* (1990); Cazabat *et al.* (1992)).

Figure 3.7 is the illustration of wavelengths l^* and the nondimensional downstream film thickness δ in the experiment (see Cazabat *et al.* (1990, 1992)). The symbols (—□—) are the experimental wavelengths, the symbols (– –O– –) are the most unstable wavelengths calculated from equation (3.15), and the symbols (—◇—) are the dimensional neutral wavelengths. This figure shows the differences between the experimental wavelength l^*_{exp} and the computed

Table 3.2 Comparisons of the experimental wavelength l^*_{exp} and the computed wavelength at largest temporal growth rate, l^*_{max}, in equation (3.15)

μ^*	λ^*	h^*	$\delta \cdot h^{*a}$	l^*_{exp}	$l^*_{max}{}^b$	$Error^c$
(mPa · s)	(Pa)	(μm)	(μm)	(μm)	(μm)	×100%
20	0.5	0.86	0.02	600^d	438.09	26.99
20	0.27	0.65	0.02	610^d	450.74	26.11
20	0.21	0.54	0.025	480	440.81	8.16
20	0.10	0.27	0.033	370	375.66	−1.53
20	0.054	0.17	0.05	340	383.32	−12.74
100	0.21	0.65	0.025^e	580	494.60	14.72
500	0.21	0.33	0.025^e	340	325.78	4.18

---

[a] $\delta \cdot h^*$ is the dimensional downstream film thickness, and the values of this parameter are the same as those of e_0 shown in Table 1 (see Cazabat *et al.* (1992)).

[b] The dimensional surface tension is $\sigma^* = 0.20 N \cdot m^{-1}$ shown in Table 1 (see Cazabat *et al.* (1992)).

[c] $Error = \frac{l^*_{exp} - l^*_{max}}{l^*_{exp}} \times 100\%$.

[d] The authors stated that the "Linear regime too short to give a precise reading" (see Cazabat *et al.* (1990)).

[e] There is no corresponding data in the paper by Cazabat *et al.* (1992).

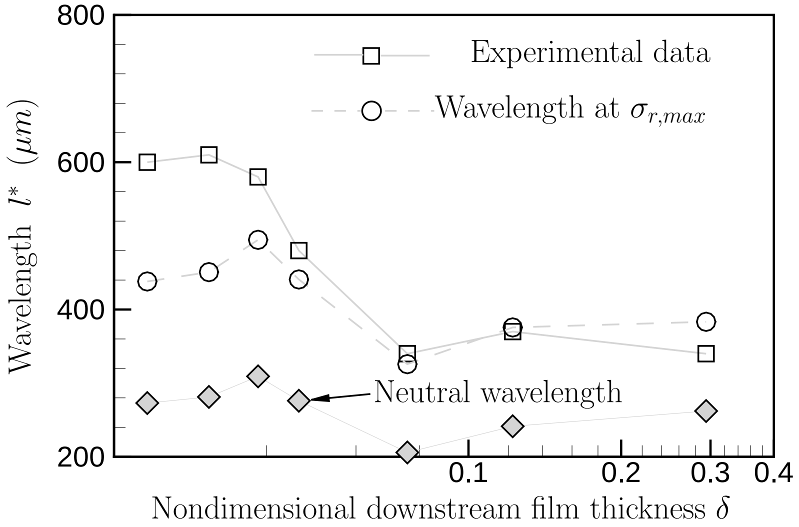

Figure 3.7 Illustration of wavelengths as a function of the nondimensional downstream film thickness δ.

wavelength at largest temporal growth rate, l^*_{max}, when they are plotted against the nondimensional downstream film thickness δ. The computed wavelengths quantitatively agree with the experimental values, even when δ is somewhat smaller than 0.1 which is the smallest δ as shown in figure 3.6.

3.5 Instability of film fronts moving through surface roughness

When a thin film flows over three-dimensional roughness, the film will be disturbed and spanwise perturbations of the film front will be generated by the roughness. For example, Kalliadasis & Homsy (2001) studied the stability of a thin film flowing over a trench which had a change in topography only in the streamwise direction. Using an energy analysis Kalliadasis & Homsy (2001) showed that the stability of a capillary ridge depended on the topography at small wavenumbers and the surface tension at high wavenumbers. In this study, spanwise perturbations of film fronts similar to those shown in figures 3.3(a) and 3.3(c) may be induced by three-dimensional roughness elements as shown in figure 3.8(a).

In figure 3.8(a), a film front is placed far upstream of a row of sinusoidal surface roughness elements with $H = h_{ice}/h = 3.226$, which is the ratio of roughness height h_{ice} and undisturbed upstream film thickness h. This film front is driven by the scaled air shear stress $\Lambda = 78.044$ and has a downstream film thickness $\delta = 0.0323$. Note that the spanwise wavelength of the sinusoidal roughness elements is $l = 4$, which is the same as that of spanwise perturbations of the film front shown in figure 3.3(a). Figure 3.8(b) shows the transient rivulet lengths which grow from the roughness induced perturbations of the two-dimensional film front. In this figure, the dashed lines with symbols (O) are the computed rivulet lengths $L\left(\tau\right)$ with $H = 0.161$ and 0.00323. The solid lines have the same slope as the solution of the stability analysis, i.e. the largest temporal growth rate σ_r as defined by equation (3.12). These two solid lines are shifted to lie along the computed nonlinear solutions $L\left(\tau\right)$ during the intervals when $L\left(\tau\right)$ obeys a power law (i.e. the relevant comparisons are the slopes of the lines). Figure 3.8(b) shows that the temporal growth rates of computed rivulets are correctly predicted by the stability analysis when the roughness height ratio H is sufficiently small. Figures 3.8(c)

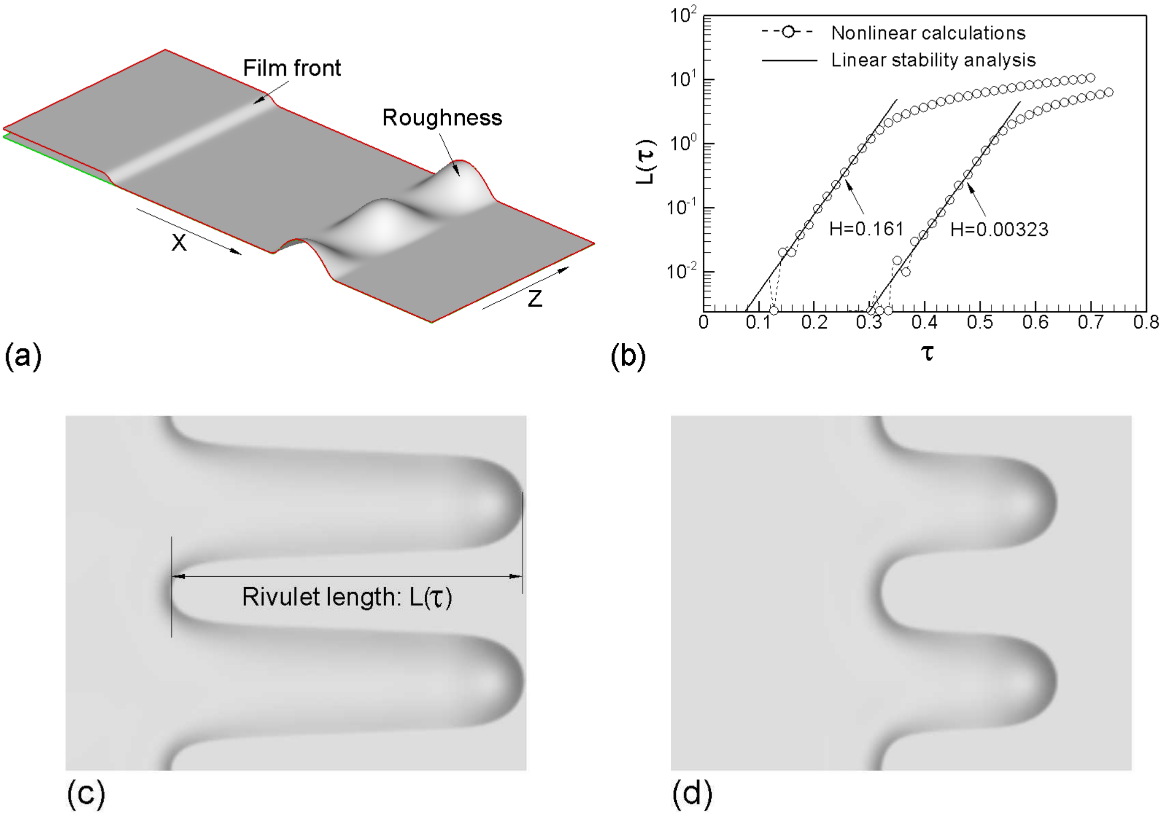

Figure 3.8 Typical results of film fronts interacting with sinusoidal surface roughness elements in the spanwise direction. (a) An initial film front and sinusoidal surface roughness elements with $H = 3.226$, (b) the computed rivulet lengths at selected times (O) and the rivulet lengths predicted by the stability analysis, (c) unstable film fronts at $\tau \approx 0.369$ resulting from the initial condition shown in figure 3.8(a) and the definition of a rivulet length $L(\tau)$, (d) unstable film fronts at $\tau \approx 0.369$ resulting from same surface roughness elements shown in figure 3.8(a) except that $H = 0.3226$. Note that the dimension of these figures in the Z-direction is $(-4, 4)$, and in the X-direction it is $(-5, 15)$ for (a), and $(22.67, 33)$ for (c) and (d).

and 3.8(d) show the rivulets which are generated as the film front moves over the roughness. The rivulets are similar to the ones shown in figure 3.3(b). The larger the roughness height ratio H, the faster the rivulets develop, as shown in figures 3.8(c) and 3.8(d).

The numerical results for the film fronts disturbed by smooth roughness elements have shown that the initial stages of spanwise perturbations on the film fronts are well predicted by the linear instability analysis if the the perturbations are small enough. These results also show that the higher the roughness elements, the stronger the nonlinear effects on the rivulets development. For example, the rivulet length in figures 3.8(c) develops faster than in figure 3.8(d). Some additional results for the evolution of disturbed film fronts are shown in the following figures. Figure 3.9 shows an array of isolated roughness elements locate downstream of a two-dimensional film front. Figure 3.9(a) shows the snapshots of the moving contact line, as the contact line is disturbed by the isolated roughness elements. The black dots are the top view of the roughness elements, and the solid lines are the contact lines. This figure shows that two rivulets are created as the spanwise disturbances on the contact lines grow. When the number of isolated roughness elements is 4, the number of rivulets is still 2 as shown in figure 3.9(d), though more disturbances are found on the moving contact lines. From the comparisons between figures 3.9(a) and 3.9(d), it is found that the disturbances at the largest temporal growth rate $\sigma_{r,\,max}$ will quickly grow into rivulets, while other disturbances at other temporal growth rates will eventually die out. It is obvious that the largest unstable wavelengths in figures 3.9(a) and 3.9(d) are both $l = 4$. From the linear instability analysis, i.e. equations (3.13) and (3.14), the largest unstable wavelength is $l_{max} = 3.838$, which is very close to the wavelengths measured from figures 3.9(a) and 3.9(d). The largest unstable wavelength explains why there are only two rivulets created in figure 3.9(d) even if there are more isolated roughness elements. Figures 3.9(b) and 3.9(c) show another row of isolated roughness elements placed downstream of the original roughness. The disturbances generated by the first row of roughness elements are driven by air through a second row of roughness elements, where new disturbances are created and interact with the oncoming disturbances. Due to the strong nonlinearity, the spanwise disturbances with the largest wavelength grow into rivulets, while others die out.

Figure 3.10 shows the evolution of thin film fronts driven by air through a random roughness field, where the roughness elements are isolated and have different sizes. The scaled air shear stress is $\Lambda = 78.044$ and the downstream film thickness is $\delta = 0.0323$. As the film fronts arrive at the roughness field as shown in figure 3.10(a), the fronts are disturbed and spanwise disturbances are created. When the disturbed film fronts move through the roughness field, the magnitude of the disturbances are small and the rivulet doesn't develop much as shown in figures 3.10(b) and 3.10(b). The rivulet lengths are measurable when the film fronts leave the roughness field as shown in figure 3.10(d). This figure also shows that a rivulet with a small wavelength located between $X = 4$ and $X = -2$ grows for a while, but soon merges with its neighbouring rivulets. Again, a disturbance will grow sooner than other disturbances if its spanwise wavelength is nearer the most unstable wavelength. Due to the different temporal growth rates, the rivulets have different lengths and the wavelengths vary a lot. The smallest wavelength in figures 3.10(e) and 3.10(f) is about $l = 2.9$. However, it is important to note that this smallest value is not smaller than the neutral wavelength $l_n = 2.396$ predicted with equations (3.13) and (3.14). The snapshots of the moving contact line are usually used to describe the moving film fronts, as shown in figure 3.11(a). The black dots are the top view of the roughness elements, and the solid lines are the top view of moving contact lines. Because of the random locations of the isolated roughness elements, the disturbances interact differently with the roughness elements and the disturbances moving downstream. The strong nonlinearity changes everything and fewer rivulets are created. Figures 3.11(b) and 3.11(c) are a spectrum analysis of the disturbed moving contact lines. These two figures are the three-dimensional view and the top view of the spectrum, where the magnitude of each wavenumber n is plotted against the time τ. As time progresses, the wavenumber of the largest magnitude becomes $n = 4$. In another word, the rivulet number is finally 4. With the spectrum analysis, it is much helpful to predicate the film fronts instability and measure the rivulet number.

Figure 3.12 is another example of the film fronts driven by air through a random roughness field, where more isolated roughness elements are placed downstream. The dimensions of the

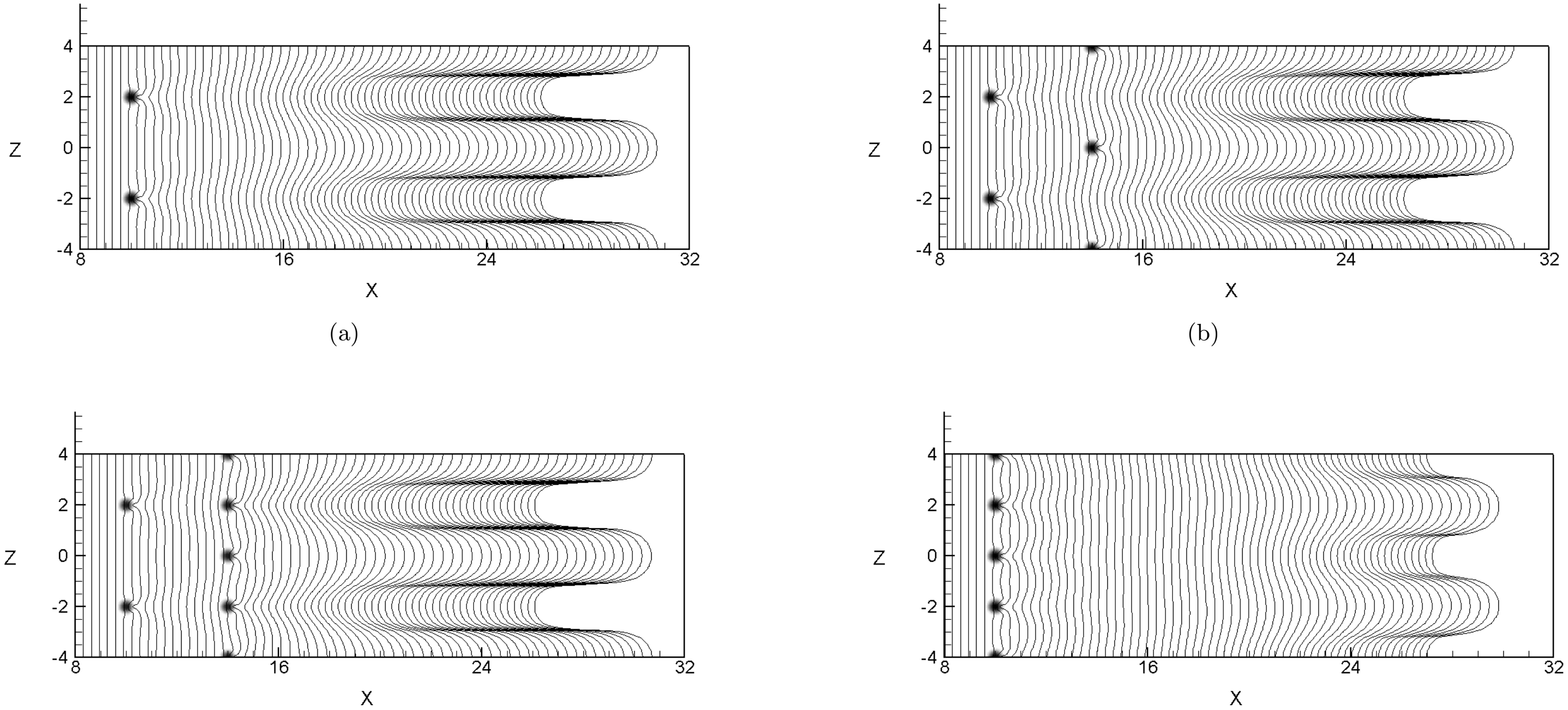

(a)

(b)

(c)

(d)

Figure 3.9 Typical solutions of the water film fronts driven by air through an array of isolated roughness elements and the evolution of disturbance interactions. Solid circles are the roughness elements, lines are the file fronts (moving in the x-direction).

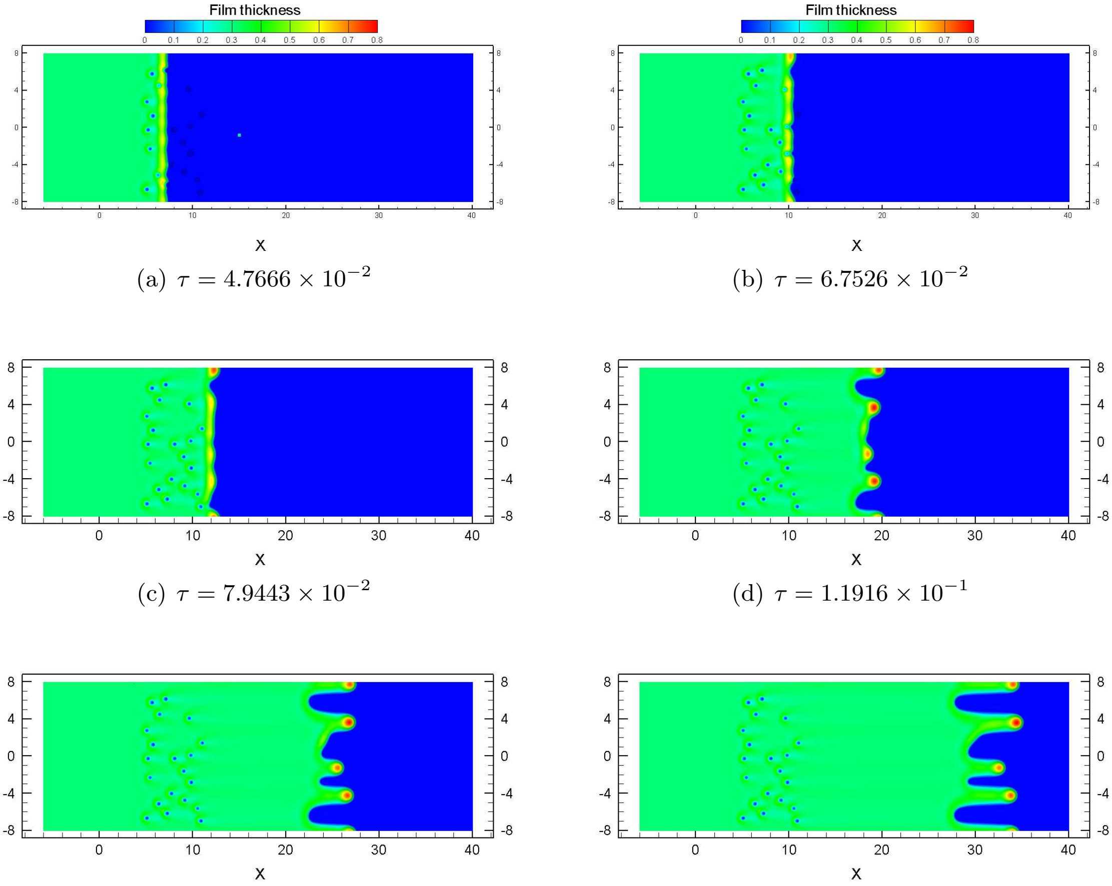

(a) $\tau = 4.7666 \times 10^{-2}$

(b) $\tau = 6.7526 \times 10^{-2}$

(c) $\tau = 7.9443 \times 10^{-2}$

(d) $\tau = 1.1916 \times 10^{-1}$

(e) $\tau = 1.5889 \times 10^{-1}$

(f) $\tau = 1.9861 \times 10^{-1}$

Figure 3.10 Typical solutions of water film fronts driven by air through a random roughness field shown at different time. The direction of water flow and air shear is from left to right. Note that the dimension of these figures in the X-direction is $(-6, 40)$, and in the Z-direction it is $(-8, 8)$.

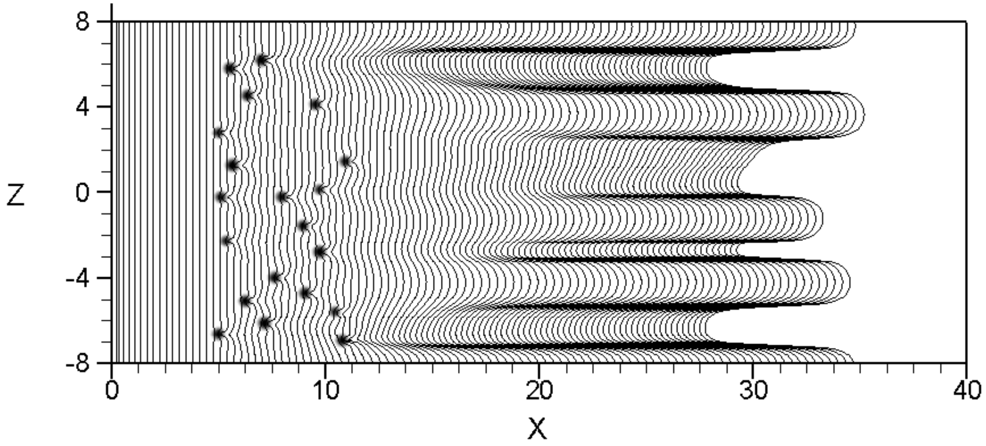

(a) Snapshots of the moving contact line

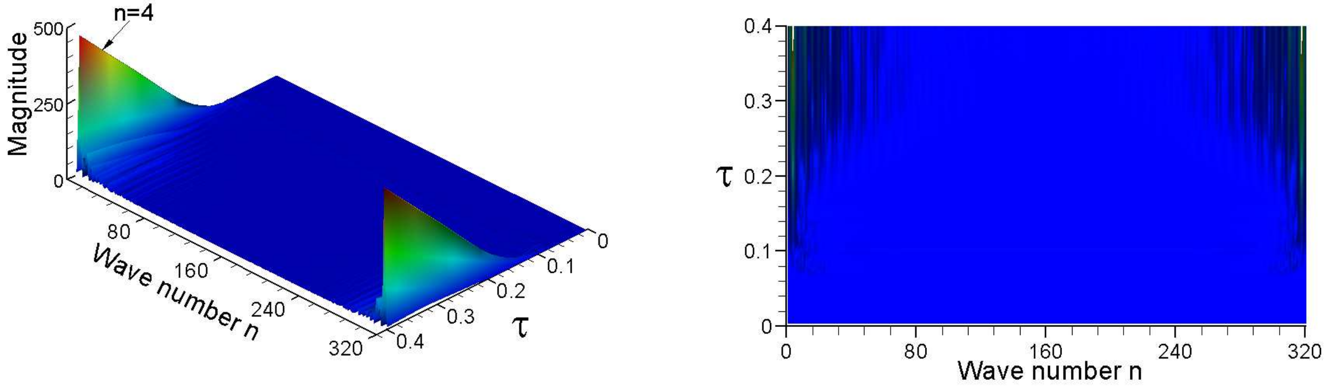

(b) 3D view of the wavenumber n

(c) Top view of the wavenumber n

Figure 3.11 Typical snapshots of the moving contact line as film fronts driven by air move through a random roughness field, and the evolution of the wavenumber n of the disturbed moving contact line and its corresponding magnitude.

computation domain in the Z-direction is $(-12, 12)$, and in the X-direction it is $(-6, 30)$, which is wider than that in figures 3.10 and 3.11. The scaled air shear stress is also $\Lambda = 78.044$ and the downstream film thickness is also $\delta = 0.0323$. Measured from figure 3.13(a), the average wavelength is still 4, though more rivulets are created than in figure 3.11(a). It is interesting to note that rivulet merging happens clearly between $X = -4$ and $X = -10.5$ in figures 3.12 and 3.13(a), where two neighbouring rivulets combine to form a larger rivulet. Figures 3.13(b) and 3.13(c) again are the spectrum analysis of the moving contact lines. The wavenumber of the largest magnitude at time τ is finally the same as that of the rivulet number, i.e. 6. This also indicates that not any disturbances can grow to form rivulets, only the ones whose wavelength is closest to the most unstable wavelength. The spectrum analysis helps reveal the evolution of the disturbances, especially when the roughness field is irregular.

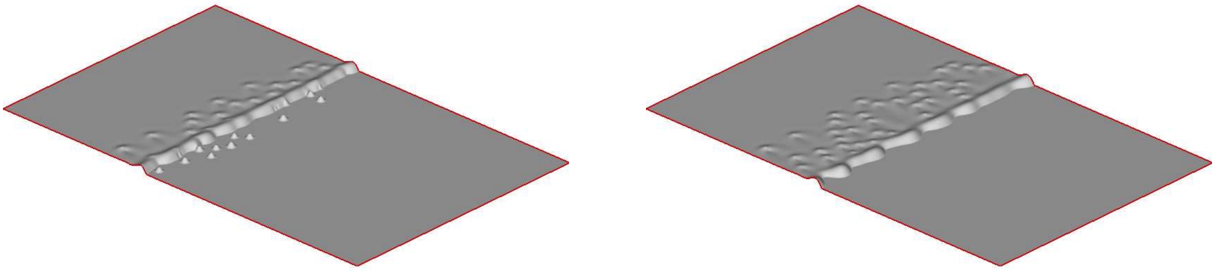

(a) $\tau = 0.1192$ (b) $\tau = 0.1589$

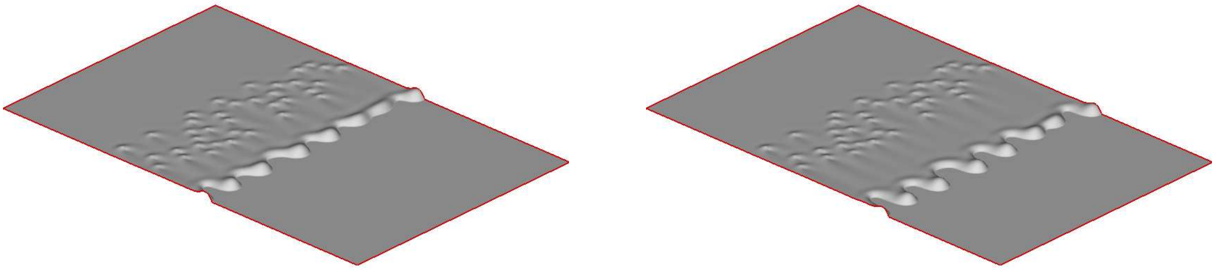

(c) $\tau = 0.1986$ (d) $\tau = 0.2383$

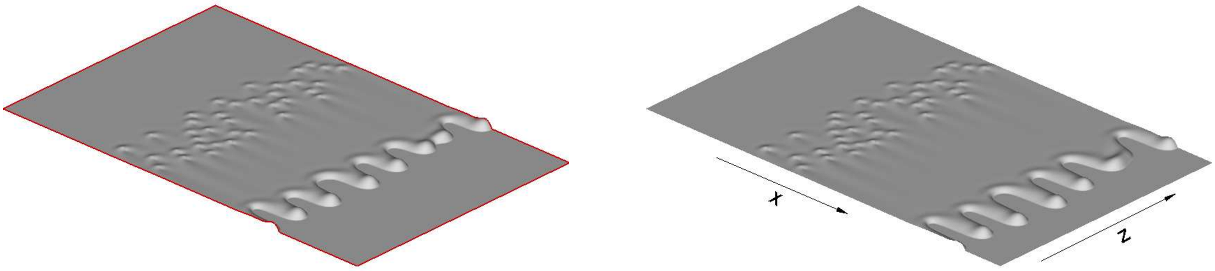

(e) $\tau = 0.2780$ (f) $\tau = 0.3297$

Figure 3.12 Typical solutions of water film fronts driven by air through a random roughness. The direction of water flow and air shear is from upper left to lower right. Note that the dimension of these figures in the Z-direction is $(-12, 12)$, and in the X-direction it is $(-6, 30)$.

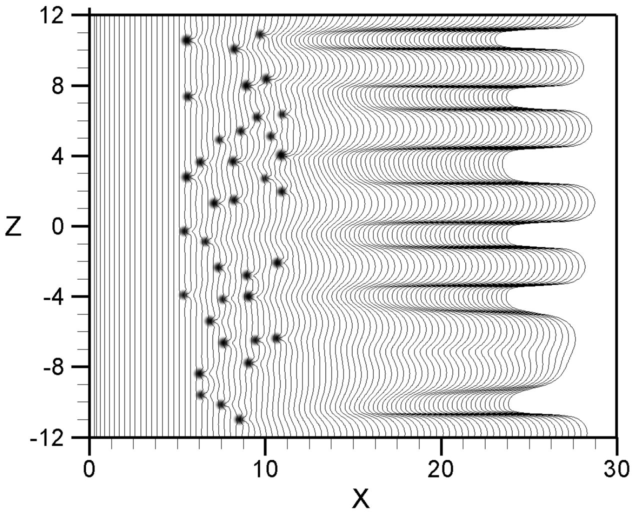

(a) Snapshots of the moving contact line

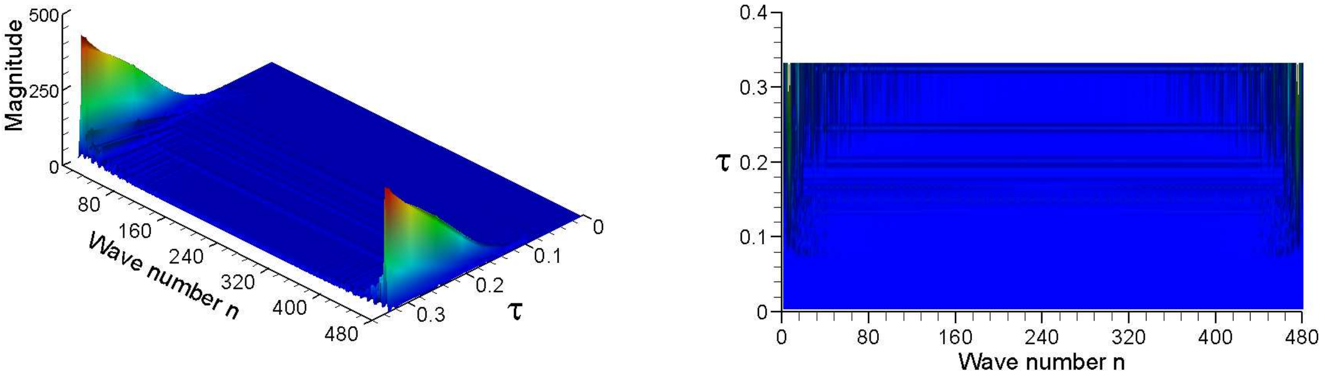

(b) 3D view of the wave number n

(c) Top view of the wave number n

Figure 3.13 Typical snapshots of the moving contact line as film fronts driven by air move through a random roughness field, and the evolution of the wave number n of the disturbed moving contact line and its corresponding magnitude.

CHAPTER 4. Surfactant transport within thin films

4.1 Problem formulation

A soluble and insoluble surfactant moving together with a film has been studied by Grotberg (1988, 1992, 1993) (also see Troian *et al.* (1989), Matar & Troian (1999), Warner *et al.* (2002), Edmonstone *et al.* (2005)). In these studies the viscosity is constant everywhere even when the surfactant concentration varies. However, surfactant diffusion and convection within a thin film will change the viscosity of the liquid mixture, especially when the liquid viscosity is strongly dependent on its concentration, as is the case with ethylene glycol and propylene glycol.

The surfactant glycol is usually used to de-ice/anti-ice wings. Bilanin & Anderson (1995) have also shown that surfactants which are contained in impinging water can have a significant effect on ice shapes. When considering de-icing and anti-icing applications, the surfactant will combine with the thin water film near the leading edge of an airfoil. For example, when ethylene glycol or propylene glycol is injected from holes at the leading edge of an airfoil it will mix with water and the viscosity of the mixture will vary everywhere within the film. The viscosity of ethylene glycol and water mixtures varies as a known function of percentage weight at $T = 293.15K$ (see Weast *et al.* (1986)). When the data points of Weast *et al.* (1986) are curve fit using a least squares method, the dynamic viscosity is found to be a simple function of the percentage weight of ethylene glycol, $w \times 100\%$, i.e.

$$\log_{10} \mu_m = kw + b, \tag{4.1}$$

where $k = 1.155$, $b = -7.70 \times 10^{-3}$, and μ_m is the mixture viscosity with units of $kg/\left(m \cdot s\right)$.

Table 4.1 Coefficients in equation (4.2)

A_1	A_2	A_3	A_4	A_5	A_6
-3.61359	986.519	127.861	-0.165301	-0.287325	1.10978

Table 4.2 Coefficients in equation (4.3)

Surfactant	A_1	A_2	A_3	A_4	A_5
Ethylene glycol	0.83818	-1.37620	-0.076729	1.07720	-0.20174
Propylene glycol	1.18886	-1.49110	-0.69682	1.13633	0.06735

Another viscosity formula for ethylene glycol and water mixtures is (see Sun & Teja (2003))

$$\ln \mu_m = w y_1 + (1-w)\, y_2 + (y_1 - y_2)\, w\,(1-w)\,(A_4 + A_5 w + A_6 \vartheta)\,, \tag{4.2}$$

where the dimensionless temperature difference is $\vartheta = (\theta^* - 273.15)\,/\,(1K)$, w is the percentage weight of ethylene glycol, $y_1 = A_1 + A_2/\,(\vartheta + A_3)$, and $y_2 = -3.750990 - 590.9808/\,(\vartheta + 137.2645)$. The coefficients in equation (4.2), i.e. $A_1 \leftrightarrow A_6$, are shown in Table 4.1. Equation (4.2) is taken from the experiment in the temperature range $\theta^* = 290K \leftrightarrow 450K$. A third viscosity formula for both ethylene glycol and propylene glycol (see ASHRAE (2001)) is

$$\ln \mu_m = A_1 + A_2 w + A_3 273.15/\theta^* + A_4 w 273.15/\theta^* + A_5\,(273.15/\theta^*)^2\,, \tag{4.3}$$

where θ^* is the dimensional temperature. The coefficients in equation (4.3), i.e. $A_1 \leftrightarrow A_5$, are shown in Table 4.2. Equations (4.1) and (4.2) are valid when the temperature is $\theta^* \geq 290K$, while equation (4.3) is valid when the temperature is $\theta^* \geq 223.15K$. Figure 4.1(a) shows a comparison of the viscosity of ethylene glycol calculated using the above three formulae, where the extended results of equation (4.2) are compared with the results of equation (4.3). Figure 4.1(b) shows the viscosity of propylene glycol calculated using equation (4.3).

In the first example, ethylene glycol and propylene glycol are injected into the film through small holes on the airfoil surface. The injection velocity is assumed to be small, and the local film thickness changes smoothly. The injection is applied as a boundary condition under the thin film. Using the scales of section 2.2, the lubrication equation with the surfactant injected

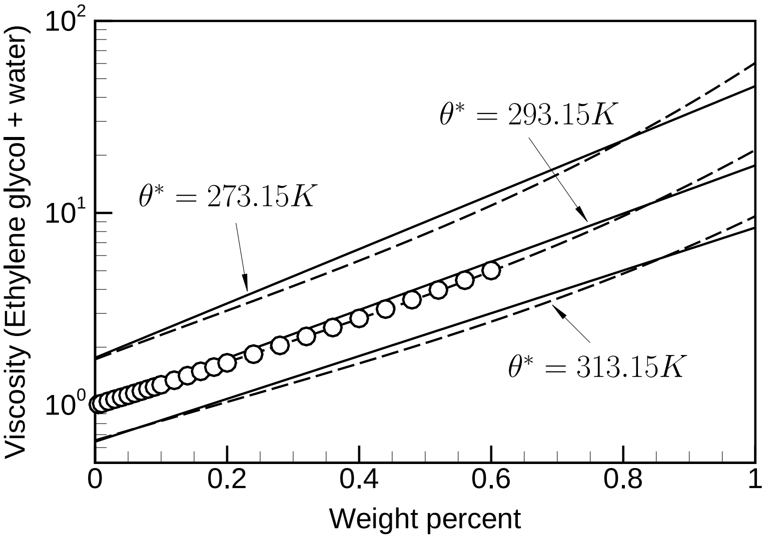

(a) Viscosity of ethylene glycol

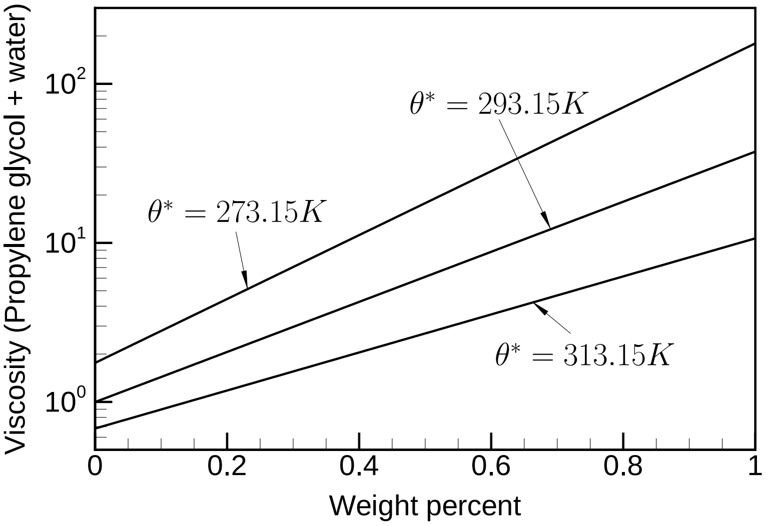

(b) Viscosity of propylene glycol

Figure 4.1 (a) Comparison of viscosity of ethylene glycol using equations (4.1), (4.2), and (4.3). Note that the result of equation (4.2) at $\theta^* = 273.15$ is out of the range of the experiment (see Sun & Teja (2003)). (b) The viscosity of propylene glycol. The symbol (O) is the result of equation (4.1), the solid lines are the results of equation (4.3), the dashed lines are the results of equation (4.2).

into the film is

$$\mu_m \frac{\partial F_{water}}{\partial T} + \frac{\partial}{\partial X}\left(\mu_m U_0 F + D_1 \frac{F^2}{2} - \frac{\partial P}{\partial X}\frac{F^3}{3}\right) + \frac{\partial}{\partial Z}\left(\mu_m W_0 F + D_3 \frac{F^2}{2} - \frac{\partial P}{\partial Z}\frac{F^3}{3}\right)$$
$$= \frac{\partial \ln \mu_m}{\partial X}\left(D_1 \frac{F^2}{2} - \frac{\partial P}{\partial X}\frac{F^3}{3}\right) + \frac{\partial \ln \mu_m}{\partial Z}\left(D_3 \frac{F^2}{2} - \frac{\partial P}{\partial Z}\frac{F^3}{3}\right)$$
$$+ \mu_m \left(V_0 - U_0 \frac{\partial F_{ice}}{\partial X} - W_0 \frac{\partial F_{ice}}{\partial Z}\right), \quad (4.4)$$

where $F = F_{water} - F_{ice}$. F_{water} is now the height of the water glycol mixture and

$$P = -\left(\frac{\partial^2 F}{\partial X^2} + \frac{\partial^2 F}{\partial Z^2} + \frac{\partial^2 F_{ice}}{\partial X^2} + \frac{\partial^2 F_{ice}}{\partial Z^2}\right). \quad (4.5)$$

The shear stresses including Marangoni forces due to the surfactant gradient are

$$D_1 = -\frac{A}{B}\frac{\partial \ln (A - B\Gamma)}{\partial X} + \lambda, \quad (4.6)$$

and

$$D_3 = -\frac{A}{B}\frac{\partial \ln (A - B\Gamma)}{\partial Z}, \quad (4.7)$$

where A and B are dimensionless variables obtained from a and b in the Langmuir equation (see Vold & Vold (1983)), i.e.

$$\Gamma^* = \frac{aC^*}{1 + bC^*}. \quad (4.8)$$

Γ is the dimensionless surface excess concentration from the Gibbs adsorption isotherm law (see Rosen (1989)), i.e.

$$\Gamma^* = -\frac{1}{R\theta^*}\frac{\partial \sigma^*}{\partial \ln C^*}, \quad (4.9)$$

where R is the gas constant, θ^* is the absolute temperature, σ^* is the surface tension, C^* is the bulk concentration, and Γ^* is the surface excess concentration. Note that the surface tension σ^* will be constant when the surfactant concentration is bigger than the critical micelle concentration (CMC) (see Islam & Kato (2003)). The dimensional surfactant transport equation is (see Stone (1990), Wong *et al.* (1996))

$$\left.\frac{\partial \Gamma^*}{\partial T^*}\right)_n + \Gamma^* W^* \bigtriangledown_s \cdot \overrightarrow{n} = - \bigtriangledown_s \cdot \left(\Gamma^* \overrightarrow{u_s^*}\right) + D_s^* \bigtriangledown_s^2 \Gamma^*. \quad (4.10)$$

Using the scales of section 2.2, equation (4.10) becomes

$$\frac{\partial \Gamma}{\partial T} + \frac{\partial (\Gamma U)}{\partial X} + \frac{\partial (\Gamma U)}{\partial Z} = D_s \left(\frac{\partial^2 \Gamma}{\partial X^2} + \frac{\partial^2 \Gamma}{\partial Z^2}\right), \quad (4.11)$$

where the velocities U and W from the film equation (4.4) are

$$\mu_m U = -\frac{\partial P}{\partial X}\frac{F^2}{2} + \mu_m U_0 + \left(-\frac{A}{B}\frac{\partial \ln (A - B\Gamma)}{\partial X} + \mu_{air}\lambda \right) F, \tag{4.12}$$

and

$$\mu_m W = -\frac{\partial P}{\partial Z}\frac{F^2}{2} + \mu_m W_0 + \left(-\frac{A}{B}\frac{\partial \ln (A - B\Gamma)}{\partial Z} \right) F. \tag{4.13}$$

Note that the Peclet number, $Pe = V_\infty L / D_s^*$, must satisfy $Pe^{-1} D_s \sim \triangle^{5/2}\sigma^{-3/2}Re^{3/4}$.

4.2 Numerical methods and solutions

The lubrication equation (4.4) is solved together the surfactant transport equation (4.11) using a 4th order Runge-Kutta method. A MUSCL difference scheme (see Van Leer (1979)) has been used to discretize the convection terms in equation (4.11), and the method of artificial compressibility (see Shapiro & Drikakis (2005)) is also used. The diffusion terms are central differenced. When the film mixes with the injected surfactant, a quick mixing model with a volume averaged method is used. In other words, it is assumed that the injected liquid mixes with the film quickly in the direction normal to the surface and the local concentration of surfactant comes quickly to its equilibrium value. The molarity of the ethylene glycol and water mixture, $C^{(inj)}$, is

$$C^{(inj)} = x^{(inj)} / \left[67.02 \cdot x^{(inj)}/1100 + 18.02 \cdot \left(1 - x^{(inj)}\right)/1000 \right], \tag{4.14}$$

where $x^{(inj)}$ is a mole function of the ethylene glycol injected into the film. Using a volume averaged method, the molarity of the ethylene glycol after quick mixing during the time interval ΔT is

$$C^{(new)} = \left[C^{(n)} \cdot F + C^{(inj)} \cdot \left| u^{(inj)} \right| \cdot \Delta T \right] / \left[F + \left| u^{(inj)} \right| \cdot \Delta T \right], \tag{4.15}$$

where $C^{(new)}$ is the molarity of the ethylene glycol and water mixtures, $C^{(n)}$ is the molarity of the ethylene glycol at $T = n\Delta T$, and water mixtures F is the film thickness, and $\left|u^{(inj)}\right|$ is the given speed of the liquid injected into the thin film through the holes on the solid wall. The mass of water, m_{water} with units of kg, is

$$m_{water} = \left| u^{(inj)} \right| \cdot \Delta T \cdot \left(1 - x^{(inj)}\right) y \cdot 18.02 + F \cdot \left(1 - C^{(n)} \cdot 67.02/1100\right) \cdot 1000, \tag{4.16}$$

and the mass of ethylene glycol, m_{EG} with units of kg, is

$$m_{EG} = \left|u^{(inj)}\right| \cdot \Delta T \cdot x^{(inj)} y \cdot 18.02 + F \cdot C^{(n)} \cdot 67.02, \tag{4.17}$$

where $y = x^{(inj)} \cdot 67.02/1100 + \left(1 - x^{(inj)}\right) \cdot 18.02/1000$. The viscosity μ_m of the ethylene glycol and water mixtures is calculated by equation (4.2) using the mass of ethylene glycol m_{EG} and water m_{water} in equations (4.1) and (4.2), respectively.

As shown in figure 4.3, a surfactant is injected into a thin water film with $\delta = 0.08$ through small holes on the wall. The surfactant mixes with the water quickly, convects and diffuses together with the thin film, which is driven by air shear stress through the aligned and offset roughness fields. The diffusion coefficient is $D_s = 0.1$ and the initial dimensionless molarity of the injected surfactant is $C^{(inj)} = 0.6$. Figures 4.2(a) and 4.3(a) show the film thickness at $T = 9.677$, and figures 4.2(b) and 4.3(b) show the surfactant concentration on the film surface at $T = 9.677$. The surfactant is transported with the water and changes the viscosity of the water/glycol mixture. It is found that the heads of rivulets in figure 4.3 are thinner than those in figure 2.5. Because the viscosity is larger within the injected streams that form the rivulets, the surfactant suppresses the formation of larger rivulet heads.

In figure 4.4, pure water droplets are statically and randomly placed onto a uniform thin film with thickness $\delta = 0.1$, where the concentration of ethylene glycol is initially $C = 0.2$. The sizes of beads are randomly given, but their geometry is controlled by an approximate ellipsoid formula (see Wang & Rothmayer (2005)) and their height, short-axis and long-axis vary from 0.2 to 0.4. When the beads are placed on the film of ethylene glycol, the surfactant will mix with the water beads due to the concentration gradients and convection. At the same time, the concentration of glycol in the film becomes non-uniform, as shown in figure 4.4(a). The blue is low concentration of ethylene glycol, while the red is high concentration. As shown in figure 4.4(b), when more pure water beads are placed into this region they are driven together by air shear stress. At the front of beads, the glycol concentration is found to be high, which leads to a high viscosity according to equations (4.1) and (4.2) and a thickening of the film. As shown in figure 4.4(b), a thinner film front is formed when the pure water beads are mixing and driven by air shear stress.

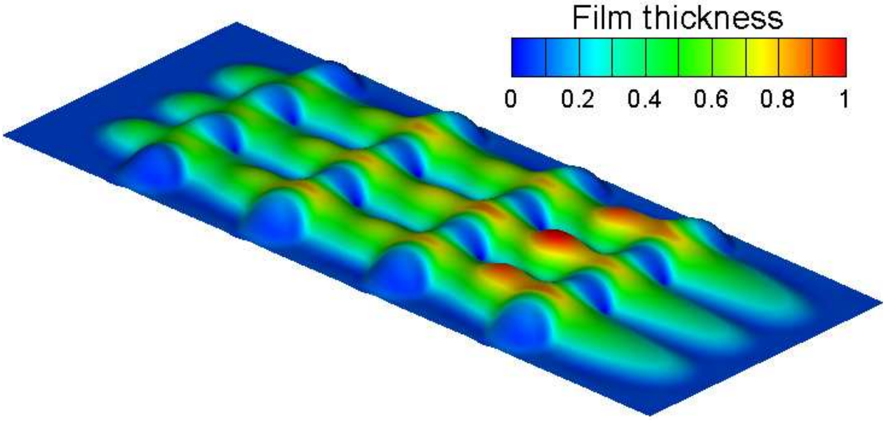

(a) Film thickness, aligned roughness

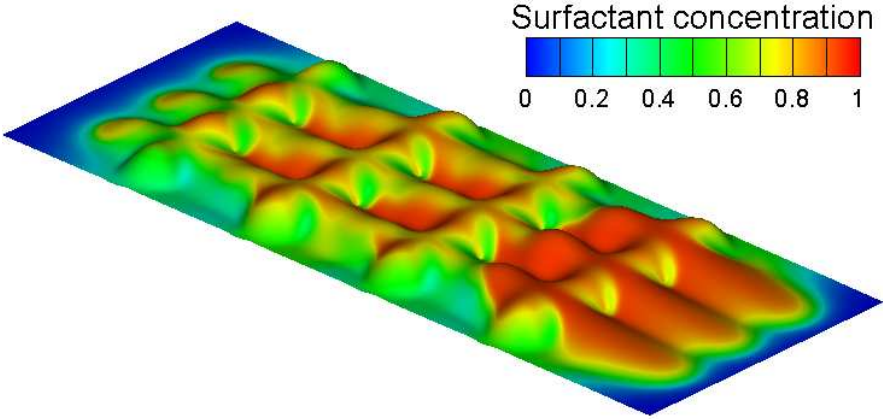

(b) Surfactant concentration, aligned roughness

Figure 4.2 Typical solutions of surfactant together with water injected into an aligned roughness field. (a) Film thickness and (b) surfactant concentration.

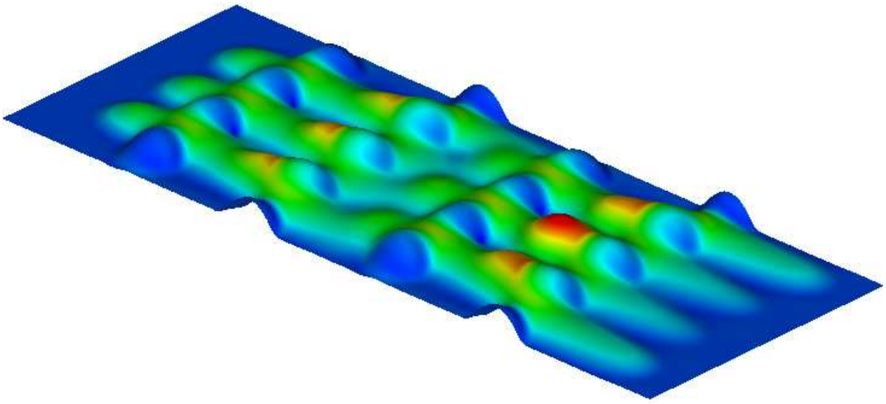

(a) Film thickness, offset roughness

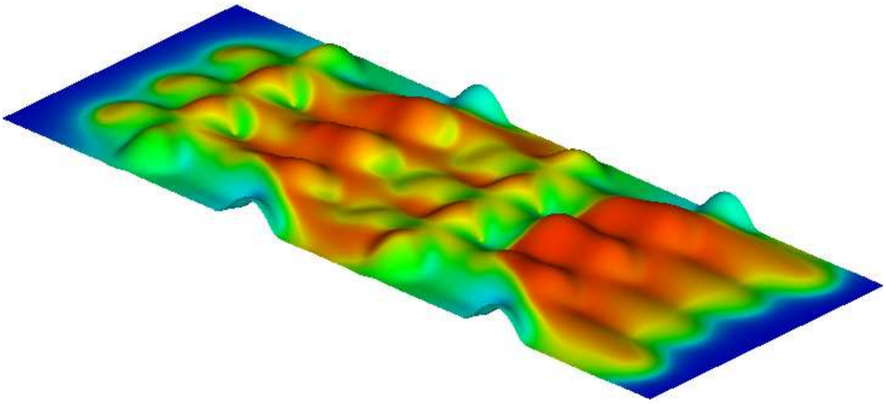

(b) Surfactant concentration, offset roughness

Figure 4.3 Typical solutions of surfactant together with water injected into an offset roughness field. (a) Film thickness and (b) surfactant concentration.

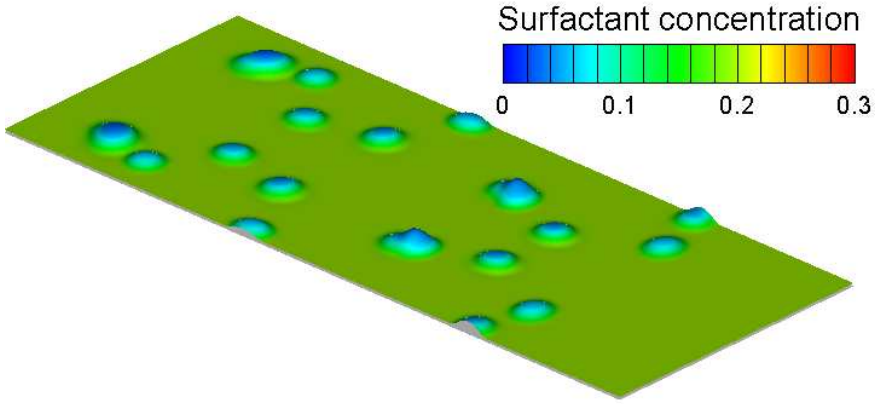

(a) $T = 0.20$

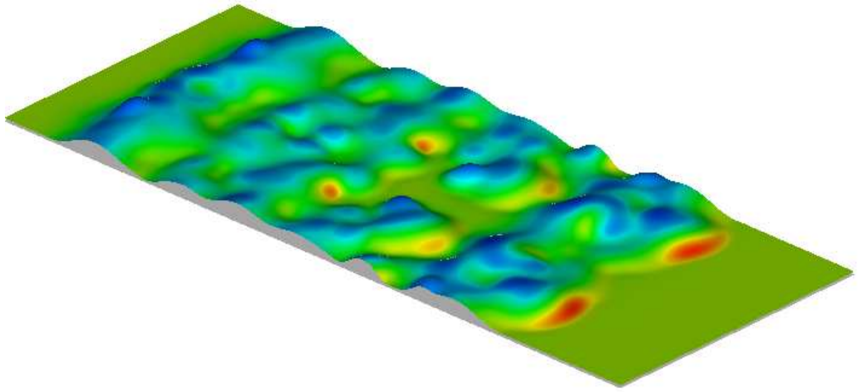

(b) $T = 1.47$

Figure 4.4 Evolution of pure water beads deposited onto a thin water film which has a uniform concentration of ethylene glycol, $C = 0.2$. The film is driven by the air shear stress $\lambda = 1$.

CHAPTER 5. Water films and droplets motion near a stagnation line

5.1 Multiple scales near a stagnation line

5.1.1 Scale derivation

Rothmayer (2006) developed a multiscale and multiphase method for handling air, water and ice surface interactions on different time scales near a stagnation line. Starting from Rothmayer's (2006) theory, a thin water film driven by air past surface roughness near a stagnation line is studied here. For the icing application, the density is assumed to be $\hat{\rho} \sim 1 + \Theta\hat{R} + \cdots$ at the leading edge of an airfoil. The length, velocities, temperature and pressure expansions in the air near a stagnation line (see Rothmayer (2006)) are

$$\hat{x}_i = Re^{-1/2}\hat{X}_i, \tag{5.1}$$

$$\hat{v}_i \sim Re^{-1/2}\hat{V}_i + \cdots , \tag{5.2}$$

$$\hat{\theta} \sim 1 \mp \Theta + M_\infty^2 \hat{\vartheta} + \cdots , \tag{5.3}$$

and

$$\hat{p} \sim P_B + Re^{-1}\hat{P} + \cdots , \tag{5.4}$$

where P_B is the pressure at the stagnation point. The time scale in the air is

$$\hat{t} \sim \hat{\tau}. \tag{5.5}$$

Water films flowing over solid ice surfaces near the stagnation line are assumed to be formed by uniformly impacting droplets, and the magnitude of the film thickness at equilibrium is (see Rothmayer (2003))

$$f_{water} \sim LWC^{1/2} Re^{-1/4} D_{aw}^{-1/4} F_{water} + \cdots , \tag{5.6}$$

where LWC is the dimensionless liquid water content, i.e. $LWC = LWC^*/\rho^*_{water}$. If $LWC \sim O\left(Re^{-1/2}D_{aw}\right)$ (see Rothmayer (2003)), then the length scales in the water become

$$(x, y, z) = \left(Re^{-1/2}X,\ Re^{-1/2}D_{aw}^{1/4}Y,\ Re^{-1/2}Z\right), \tag{5.7}$$

and the expansions of velocities, temperature and pressure at leading order are

$$(u, v, w) \sim \left(Re^{-1/2}D_{aw}^{3/4}U, Re^{-1/2}D_{aw}V, Re^{-1/2}D_{aw}^{3/4}W\right) + \cdots, \tag{5.8}$$

$$\theta \sim 1 \mp \Theta + D_{aw}^{3/4}M_\infty^2\vartheta + \cdots, \tag{5.9}$$

$$p \sim P_B + Re^{-1}D_{aw}^{-1/4}P + \cdots. \tag{5.10}$$

Note that the dimensionless surface tension σ is $\sigma = Re^{-1/2}D_{aw}^{-1/2}\Sigma$. The time scale in water is

$$t \sim D_{aw}^{-3/4}\tau, \tag{5.11}$$

which is much larger than that in the air, i.e. equation (5.5). As shown in equations (5.5) and (5.11), the time scale in the water is about 178 times larger than that in the air if the density ratio is $D_{aw} \simeq 10^{-3}$. To take the different time scales into account, the method developed by Rothmayer (2006) is used here. The multiple time scales are

$$t_0 = t \quad \text{and} \quad D_{aw}^{-3/4}t_1 = t, \tag{5.12}$$

i.e.

$$\partial t \sim \partial t_0 + D_{aw}^{3/4}\partial t_1 + \cdots. \tag{5.13}$$

Expansions of water film thickness, velocities, pressure and temperature in air/water system are

$$f_{water} \sim Re^{-1/2}D_{aw}^{1/4}F_0\left(t_0, t_1, x_i\right) + Re^{-1/2}D_{aw}F_1\left(t_0, t_1, x_i\right) + \cdots, \tag{5.14}$$

$$v \sim Re^{-1/2}D_{aw}V_0 + Re^{-1/2}D_{aw}^{5/4}V_1 + \cdots, \tag{5.15}$$

$$(u, w) \sim Re^{-1/2}D_{aw}^{3/4}\left(U_0, W_0\right) + Re^{-1/2}D_{aw}\left(U_1, W_1\right) + \cdots, \tag{5.16}$$

$$p \sim P_B + Re^{-1}D_{aw}^{-1/4}P_0 + Re^{-1}D_{aw}^{1/2}P_1 + \cdots \tag{5.17}$$

and

$$\theta \sim 1 \mp \Theta + D_{aw}^{3/4}\Theta\vartheta_0 + D_{aw}\Theta\vartheta_1 + \cdots . \tag{5.18}$$

After above expansions are substituted into the dimensionless kinematic boundary condition

$$v = \frac{\partial f_{water}}{\partial t} + u\frac{\partial f_{water}}{\partial x} + w\frac{\partial f_{water}}{\partial z}, \tag{5.19}$$

At the leading order, i.e. $O\left(Re^{-1/2}D_{aw}^{1/4}\right)$, the equation is

$$\frac{\partial F_0}{\partial t_0} = 0. \tag{5.20}$$

Note that equation (5.20) shows that F_0 is independent of the short time scale t_0. From the definition of pressure P_0, it is easy to determine that $P_0 = P_0\left(t_1, \cdots\right)$, while at order $O\left(Re^{-1/2}D_{aw}\right)$ the kinematic boundary condition becomes

$$V_0 = \frac{\partial F_1}{\partial t_0} + \frac{\partial F_0}{\partial t_1} + U_0\frac{\partial F_0}{\partial X} + W_0\frac{\partial F_0}{\partial Z}. \tag{5.21}$$

The mass conservation, momentum conservation and energy conservation equations at leading order in the water become

$$\frac{\partial U_0}{\partial X} + \frac{\partial V_0}{\partial Y} + \frac{\partial W_0}{\partial Z} = 0, \tag{5.22}$$

$$\frac{\partial U_0}{\partial t_0} = -\frac{\partial P_0}{\partial X} + \frac{\partial^2 U_0}{\partial Y^2}, \tag{5.23}$$

$$0 = \frac{\partial P_0}{\partial Y}, \tag{5.24}$$

$$\frac{\partial W_0}{\partial t_0} = -\frac{\partial P_0}{\partial Z} + \frac{\partial^2 W_0}{\partial Y^2}, \tag{5.25}$$

$$\frac{\partial \vartheta_0}{\partial t_0} = \frac{1}{Pr}\frac{\partial^2 \vartheta_0}{\partial Y^2}. \tag{5.26}$$

Note that the entire film is now an interface layer, as defined in Rothmayer (2006). The time-averaged lubrication equation near a stagnation line is then found to be

$$\frac{\partial F_0}{\partial t_1} + \frac{\partial}{\partial X}\left(\bar{\lambda}_X\frac{F^2}{2} - \frac{\partial P_0}{\partial X}\frac{F^3}{3}\right) + \frac{\partial}{\partial X}\left(\bar{\lambda}_Z\frac{F^2}{2} - \frac{\partial P_0}{\partial Z}\frac{F^3}{3}\right) = 0, \tag{5.27}$$

where $\bar{\lambda}_X$ and $\bar{\lambda}_Z$ are the time averaged air shear stresses in the streamwise and spanwise directions respectively, i.e.

$$\left(\bar{\lambda}_X,\, \bar{\lambda}_Z\right) = \lim_{T_0\to\infty}\frac{1}{T_0}\int_{t_0=t_a}^{t_0=T_0+t_a}\left(\lambda_X,\, \lambda_Z\right)dt_0, \tag{5.28}$$

where t_a is the initial time value and the time interval T_0 is assumed to be sufficiently large. The air streamwise and spanwise shear stresses, i.e. λ_X and λ_Z, can be nonlinear functions of t_0 and t_1. The film thickness F is $F = F_0 - F_{ice}$, and the pressure is

$$P_0 = -\Sigma K = -\Sigma \left(\frac{\partial^2 F_0}{\partial X^2} + \frac{\partial^2 F_0}{\partial Z^2} \right) . \qquad (5.29)$$

For simplicity, $\Sigma = 1$ is used in the following calculations. The above analysis says that the stagnation line film responds as a lubrication equation to an average applied air shear stress. This final result may be readily seen by noting that the film shape F_0 does not respond to the faster air time scale. A time average of the Stokes layer equations within the film, i.e. equations (5.22-5.26), over the fast air time scale yields the same steady Stokes equations which produce the standard lubrication equation used in previous sections, but now on the slower water time scale. In the following sections, the numerical boundary conditions of equation (5.27) are taken to be

$$\partial F_0 / \partial X = 0 \quad \text{as } X \to \pm\infty \, . \qquad (5.30)$$

Equation (5.27) shows that the effects of high frequency nonlinear air disturbances can be neglected within the context of the multiscale problem. Furthermore, the air shear stress near the stagnation line for a self-similar solution (see Schlichting & Gersten (1999), Rothmayer (2003)) is a well-known power function of the distance from the stagnation point. For simplicity, the air shear stress is taken to be a linear function, i.e. the pressure gradient parameter is $\beta = 1$ in the self-similar solution near a stagnation line.

5.1.2 Numerical results

When a film with a uniform thickness on a flat surface is driven by air near a stagnation line, the air shear stress is assumed to be $\lambda = kX$ and the exact solution of equation (5.27) for the decrease of the stagnation film height when no additional water mass is deposited on the surface is

$$\left[F_0 \left(t_1 \right) \right]^{-1} = k t_1 / 2 + \left[F_{0,\, initial} \right]^{-1} , \qquad (5.31)$$

where $F_{0,\, initial} = F_0 \left(t_1 = 0 \right)$. Figures. 5.1 and 5.2 show comparisons of exact solutions of equation (5.31) and numerical solutions of equation (5.27). As shown in figure 5.1(a), initial film thicknesses are different, i.e. $\delta = 0.04$, 0.1, 0.4, and the air shear stress is a linear function of location X, i.e. $\lambda = 2X$. In this figure the solid lines are solutions of equation (5.31), while the symbols are the numerical solutions of equation (5.27), which agree well with the exact solutions. In figure 5.1(b), the slopes of air shear stress are different, i.e. $k = 0.2$, 1, 2, 10, 20, where exact solutions of equation (5.31) are shown as the solid lines and these agree well with numerical solutions of equation (5.27) which are shown as the symbols. If the shear stress is a more complicated nonlinear function of X, for example $\lambda = 100 \tanh(0.02X)$, it approaches the shear stress $\lambda = 2X$ in the region of $10 \leq X \leq 10$ as shown in figure 5.2(a). However, this nonlinear shear stress $\lambda = 100 \tanh(0.02X)$ will approach the constant values $\lambda = \pm 100$ when $X \rightarrow \pm\infty$, i.e. this shear stress will be constant and its derivatives will be zero when $X \rightarrow \pm\infty$, which means that the boundary condition (5.30) can be used for this applied shear profile. Thicknesses with $\lambda = 2X$ and $\lambda = 100 \tanh(0.02X)$ are compared at $X = 0$ and $X = \pm 25$ as shown in figure 5.2(b).

Figures 5.3 and 5.4 show three-dimensional droplets which are driven by air with $\lambda = 0.1X$ to both sides of stagnation line, i.e. the red lines. In figure 5.3(a), smaller sized droplets are deposited on the left side of the stagnation line, and bigger droplets are placed at the stagnation line and to the right of the stagnation line. As shown in figures 5.3(b) and 5.3(c) at $t_1 = 3.13$ and 6.25 respectively, the droplets' shapes and locations are almost the same if the precursor film thicknesses are $\delta = 0.001$ and 0.0001. It is clear that the droplets at the stagnation line do not change much. However, the further the droplets are from stagnation line the faster they will run back. In figure 5.4, droplets are driven by different shear stresses, i.e. $\lambda = 0.1X$ and $\lambda = 0.01X$. As shown in figures 5.4(b) and 5.4(c), the larger the slope of shear stress, the faster the droplets will run back at the same location. However, the droplets maintain almost constant shape at the stagnation line, i.e. when $\lambda = 0$.

Randomly deposited three-dimensions droplets driven by air near a stagnation line are shown in figure 5.5. figure 5.5(a) shows the different roughness elements which are randomly placed near the stagnation line. The water droplets are randomly and continuously deposited onto this region, and driven by air toward both sides of the stagnation line, as shown in

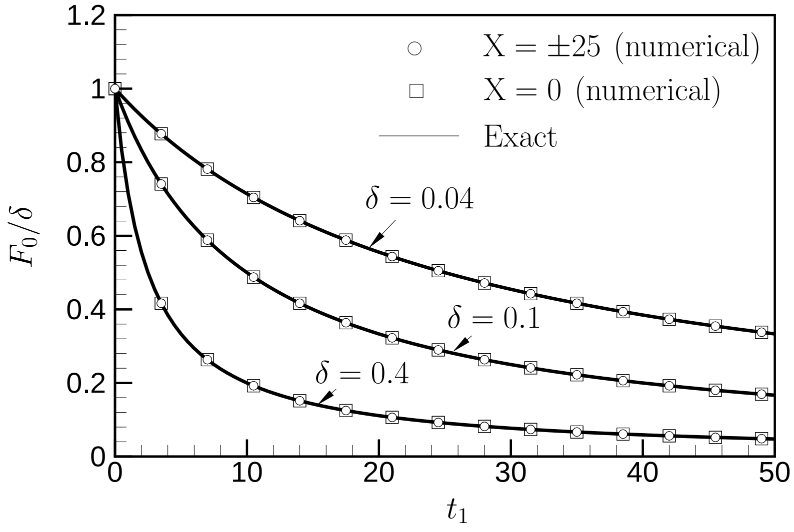

(a) Different δ

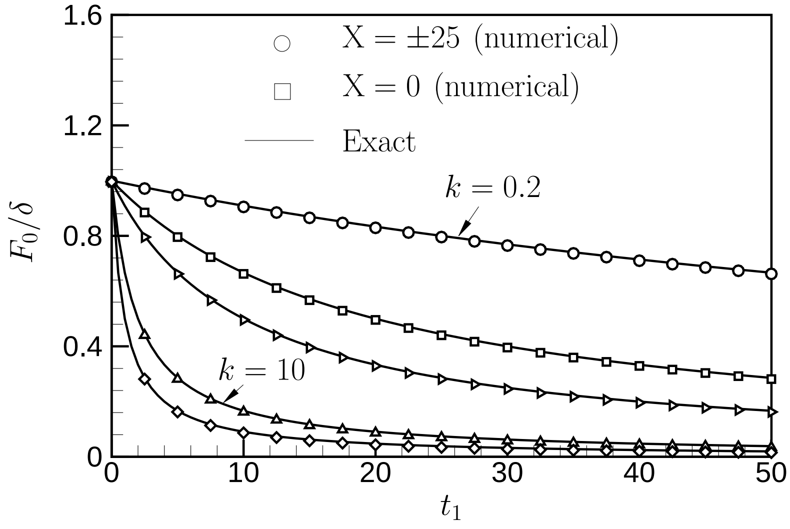

(b) Different k

Figure 5.1 Comparisons between exact solutions and numerical solutions for a flat film driven by air near the stagnation line. (a) Solutions with different initial film thickness δ, (b) solutions with different slopes, k, of the shear stress $\lambda = kX$ when $\delta = 0.1$. Note that δ is $\delta = F_{0,\, initial}$, and the coefficient k is in the sequence, i.e. $k = 0.2$, 1, 2, 10, 20.

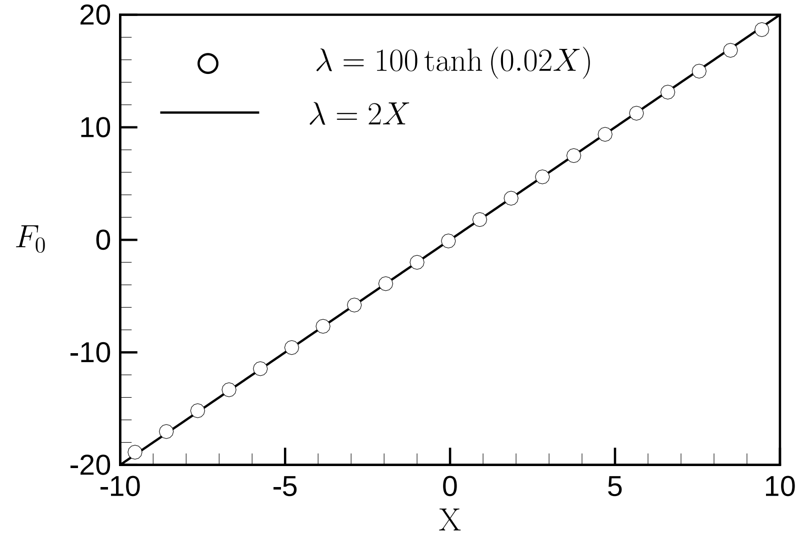

(a) Linear/nonlinear air shear stresses

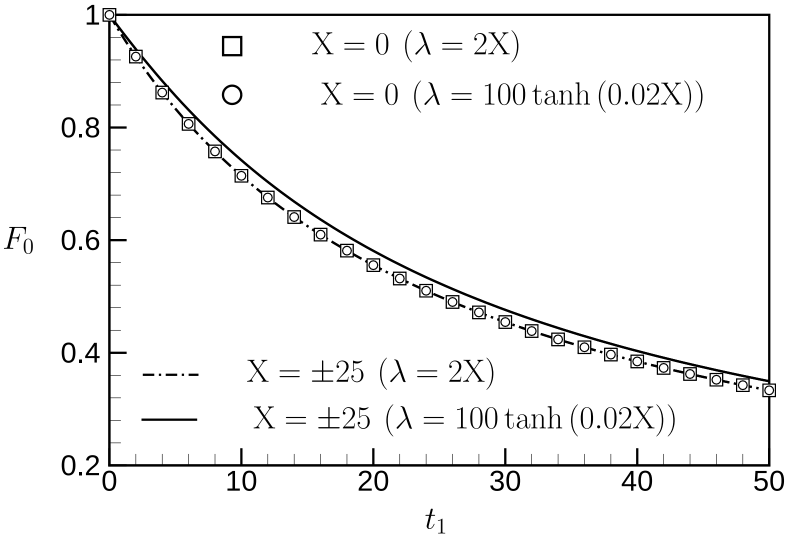

(b) Film thickness

Figure 5.2 Comparisons of numerical solutions when the air shear stress is chosen to be a linear and a nonlinear function of X. X is the distance from the stagnation line.

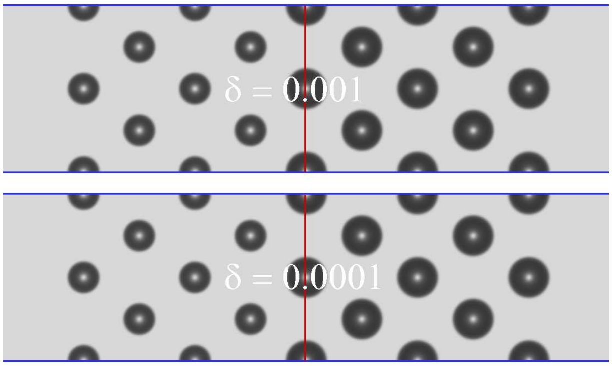

(a) $t_1 = 0$

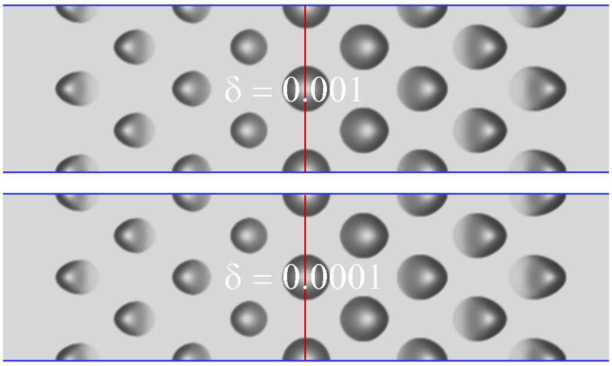

(b) $t_1 = 3.13$

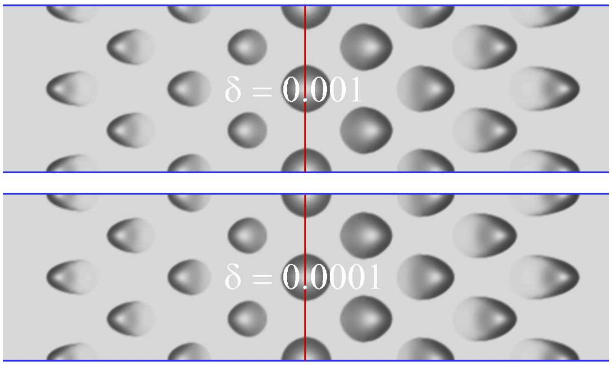

(c) $t_1 = 6.25$

Figure 5.3 Typical solutions of droplets deposited on a flat plate near a stagnation line and driven by air to both sides. The precursor film thickness is $\delta = 0.001$ (top three figures) and $\delta = 0.0001$ (bottom three figures).

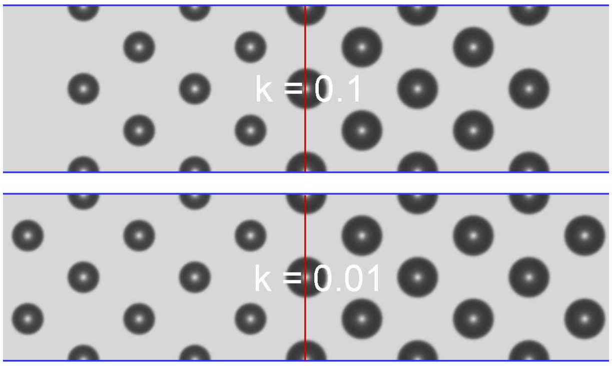

(a) $t_1 = 0$

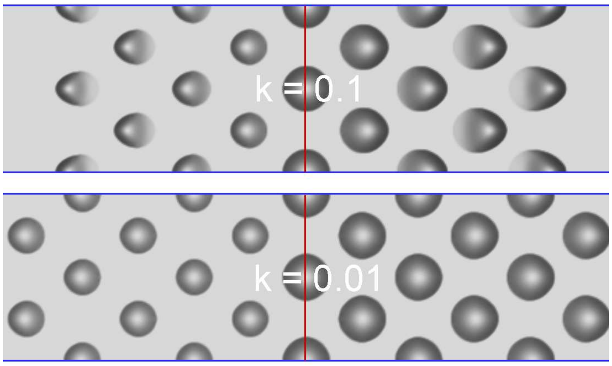

(b) $t_1 = 3.13$

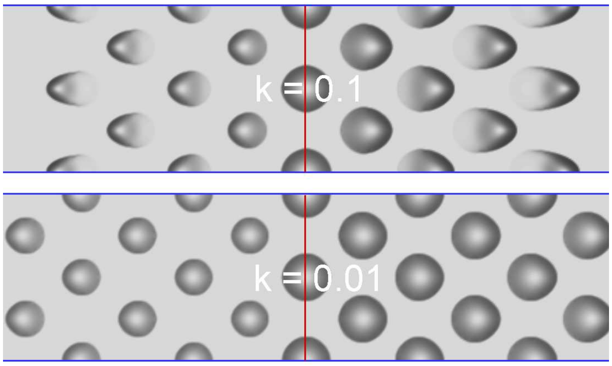

(c) $t_1 = 6.25$

Figure 5.4 Typical solutions of droplets deposited on a flat plate near a stagnation line and driven by air to both sides. The shear stress rate is $k = 0.1$ (top three figures) and $k = 0.01$ (bottom three figures).

figures 5.5(b) and 5.5(c). Due to the interaction between roughness elements and droplets, the patterns of rivulets look quite different on either side of the stagnation line. Because the shear stress is small at the stagnation line, the droplets merge together there and the water thickness increases when droplets are continuously deposited.

5.2 Thin films with a disjoining pressure model

5.2.1 Disjoining pressure models

When the thickness of a thin film is about $0.1 \sim 1\mu m$, it can be still treated as a continuous media (see de Gennes (1985)). However, van der Waals forces can come into play and their effect is called a disjoining pressure, Π (see Deryagin & Churaev (1976), Frumkin (1938)). When the film thickness is small enough, a disjoining pressure dominates, and the stability and wettability are also controlled by this effect (see Wu & Wong (2004)). Williams & Davis (1982) studied thin liquid films effected by molecular forces using long wave theory, and showed that film rupture is accelerated due to the nonlinear effects. Burelbach, Bankoff & Davis (1988) studied the long wave evolution equation effected by the van der Waals attractions and the Marangoni force. Usually, the disjoining pressure Π contains total intermolecular pair potentials per unit area, which consists of intermolecular attractive and repulsive potentials. Similar intermolecular pair potentials can be derived with a microscopic density functional theory (see Bauer & Dietrich (1999), Dietrich & Napiorkowski (1991)). For a more general power-law potential, a dimensionless formula of a disjoining pressure Π in a thin film, i.e. $P_0 = -\Sigma K - \Pi$ (see equation (5.29)), is often written as

$$\Pi = B_m \left(\frac{\delta}{F}\right)^m - B_n \left(\frac{\delta}{F}\right)^n, \tag{5.32}$$

where m and n are integers, and $m > n > 1$. B_m and B_n are dimensionless coefficients of repulsive and attractive terms, which are related to the droplet dynamic contact angle (see Schwartz & Eley (1998)). F is the thickness of the film at a given position X, and δ is the precursor film thickness used in this paper. The integer pair (m, n) is often set to be $(m, n) = (3, 2)$ (see Schwartz & Eley (1998), Eres, Schwartz & Roy (2000)), $(m, n) = (4, 3)$

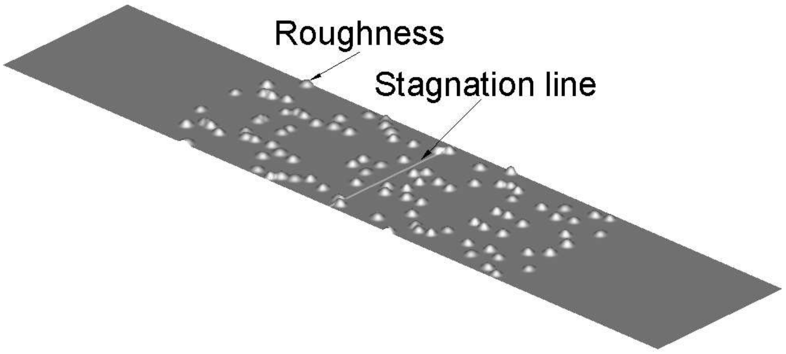

(a) $t_1 = 0$

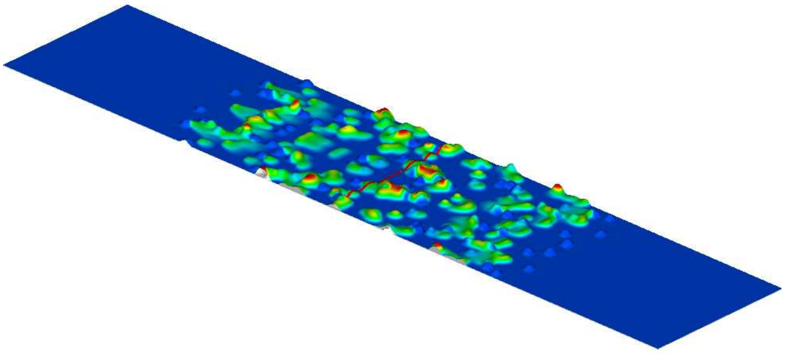

(b) $t_1 = 0.64$

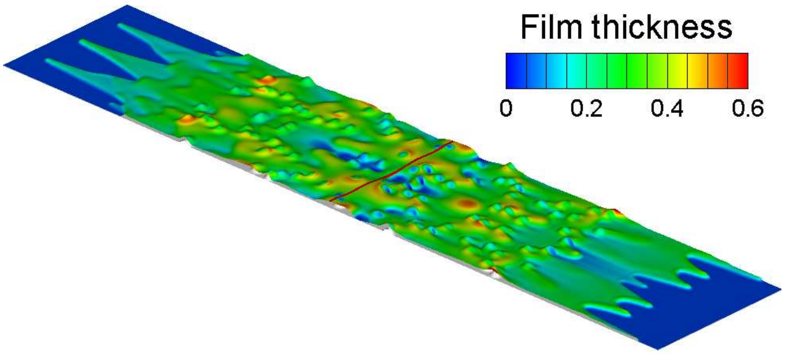

(c) $t_1 = 3.2$

Figure 5.5 A typical solution of droplets randomly deposited on a roughness field near the stagnation line and driven by air towards both directions. The roughness elements are randomly placed near the stagnation line. Note that the shear stress is $\lambda = 2X$ and the initial uniform film thickness is $\delta = 0.05$.

(see de Gennes (1985), Oron & Bankoff (1999), Schwartz & Eley (1998), Glasner (2003)), $(m, n) = (6, 3)$ (see Pismen & Thiele (2006)), and $(m, n) = (9, 3)$ (see Khanna & Sharma (1997)).

Hocking (1993) derived a disjoining pressure which is dependent on the contact angle α at equilibrium, but allowed the slope of the value $\partial F/\partial X$ to be different from the equilibrium value, i.e.

$$\Pi = \frac{B}{F^3}\left(\alpha^4 - \frac{\partial^4 F}{\partial X^4}\right). \tag{5.33}$$

Starting from the minimum total energy in a droplet, Wu & Wong (2004) derived a slope-dependent disjoining pressure, i.e.

$$\Pi = \frac{B}{F^3}\left(\alpha^4 - \frac{\partial^4 F}{\partial X^4} + 2F\left(\frac{\partial F}{\partial X}\right)^2 \frac{\partial^2 F}{\partial X^2}\right), \tag{5.34}$$

where α is a contact angle and B is a material constant. Wu & Wong (2004) argued that the higher-order term in the disjoining pressure (5.34), i.e. $2B/F^2\left(\partial F/\partial X\right)^2 \partial^2 F/\partial X^2$, prevents a contact line from moving without slip. To evaluate the effects of a disjoining pressure model on droplet motion, the disjoining pressure (5.32) is used in this study.

In the icing problem, the water film thickness is on the order of $20 \sim 40\mu m$, and sometimes it is a lot thinner due to the phase change. Droplets and beads are found to remain near the stagnation line or move along the water film when they are far from the stagnation line (see Olsen & Walker (1987)).

5.2.2 Numerical results

A typical example of the effect of the disjoining pressure is shown in figure 5.6(a), where a short rivulet at a film front is driven by air shear stress. The upstream film thickness is h = 0.3 and downstream film thickness is $\delta = 0.1$, and the air shear stress is $\lambda = 2$. The parameters in the disjoining pressure model (5.32) are $(m, n) = (3, 2)$ and $B_m = B_n = 30$. Figure 5.6(b) shows that when the short rivulet is broken into droplets by the disjoining pressure, the corresponding perturbation at the film front propagates back into the deeper film. At the same time "holes" form in the film near the film front, and more isolated droplets are formed from the film breakup.

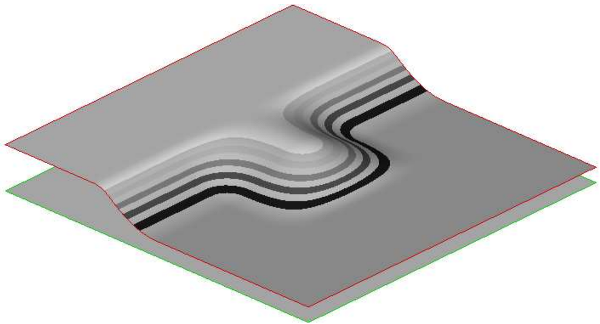

(a) $t_1 = 0$

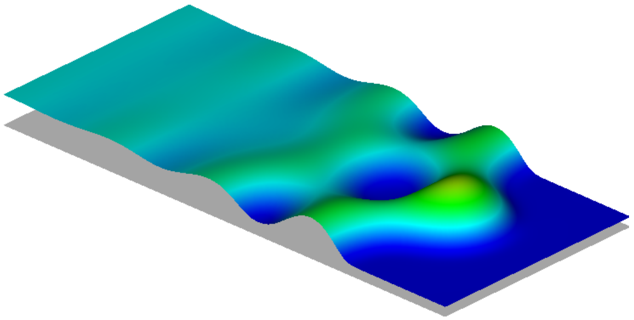

(b) $t_1 = 20$

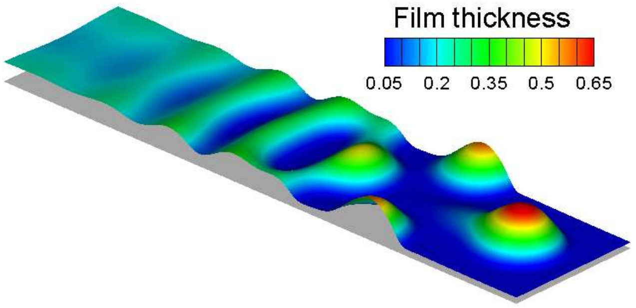

(c) $t_1 = 40$

Figure 5.6 Typical solutions using a disjoining pressure model, with rivulets driven by air which are broken into droplets. Note that the dimension of these figures in Z-direction is $(-2, 2)$, and in X-direction it is $(-2, 2)$ for figure 5.6(a), $(0, 9)$ for figure 5.6(b), and $(1, 18)$ for figure 5.6(c).

When droplets move near the stagnation line at the leading edge of wing, the solid ice surface is usually not flat due to the growth of ice roughness elements. The droplets move through these roughness fields, and their behavior will be examined when the disjoining pressure is large. Figure 5.7(a) shows a droplet which is deposited in front of three roughness elements which are labeled $1, 2, 3$, and the direction of droplet movement is shown in 5.7(b). Figures 5.7(c-h) show the interaction between the droplet and the three roughness elements. At $t_1 = 0.096$, the droplet touches the roughness 1, and begins to deform under the air shear force, disjoining pressure and capillary force. At $t_1 = 0.256$, the droplet moves into the gap between the roughness elements 1 and 2, and at $t_1 = 0.448$, it has been stopped for a while in the gap between the three roughness elements. The droplet continues to deform, as shown in figure 5.7(f), but it also slides around the roughness 3 and eventually leaves the roughness field as shown in figure 5.7(h). At this point, the droplet shape returns to a circle (as seen from the top view). Note that the parameters in the disjoining pressure model (5.32) are $(m, n) = (3, 2)$ and $B_m = B_n = 400$, and the shear stress is $\lambda = 2$, all of which are the same for results shown in figures 5.7-5.9.

Two droplets of the same size are placed upstream of a roughness field and are driven by air in figure 5.8. The droplets are trapped between the gap of roughness elements in figure 5.8(b) at $t_1 = 0.5$, and they do not move for a while. At $t_1 = 2$ as shown in figure 5.8(c), the stable status is broken and two droplets begin to move around the roughness. At $t_1 = 3.4$, they merge and are stopped by the roughness elements again.

In figure 5.9, three droplets with the same size as those droplets shown in figures 5.8 are placed upstream of an offset roughness field. The droplets are stopped by the roughness at $t_1 = 0.768$, and they merge together into a larger droplet at $t_1 = 0.896$. Due to the disjoining pressure and the effect of roughness the bigger water droplet is split into two droplets as shown in figure 5.9(d). These two droplets will move forward as they are driven by air.

Finally, figure 5.10 shows a comparison of droplet motion near a stagnation line with and without a disjoining pressure model. As shown in figure 5.10(a), the water droplets merge together and more thin films are observed than when a disjoining pressure model is used in

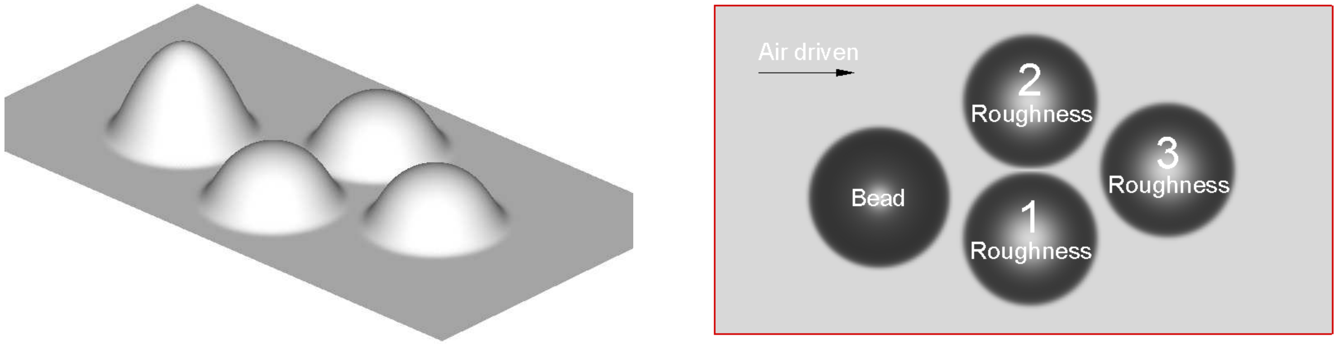

(a) 3D view

(b) Top view as $t_1 = 0$

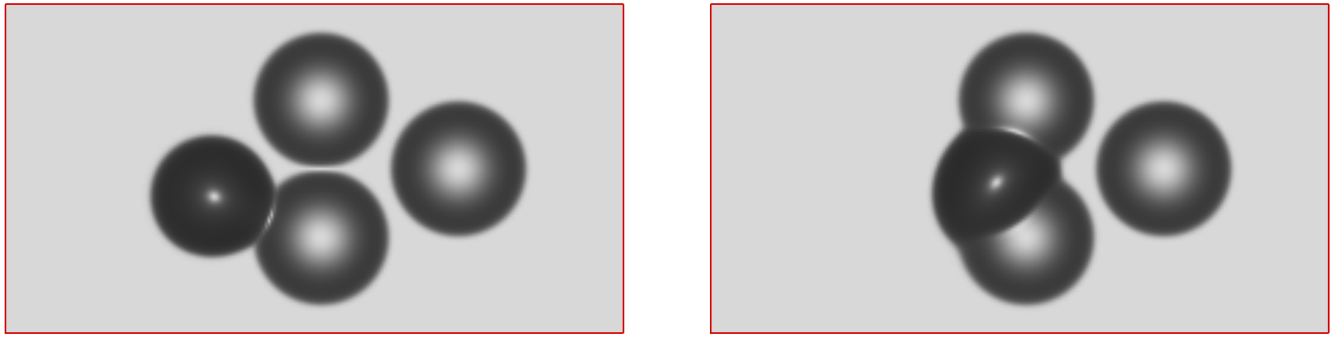

(c) $t_1 = 0.096$

(d) $t_1 = 0.256$

Figure 5.7 Typical solution of a single droplet interacting with roughness elements, moving around the roughness elements and leaving the roughness field when driven by air and with a large disjoining pressure.

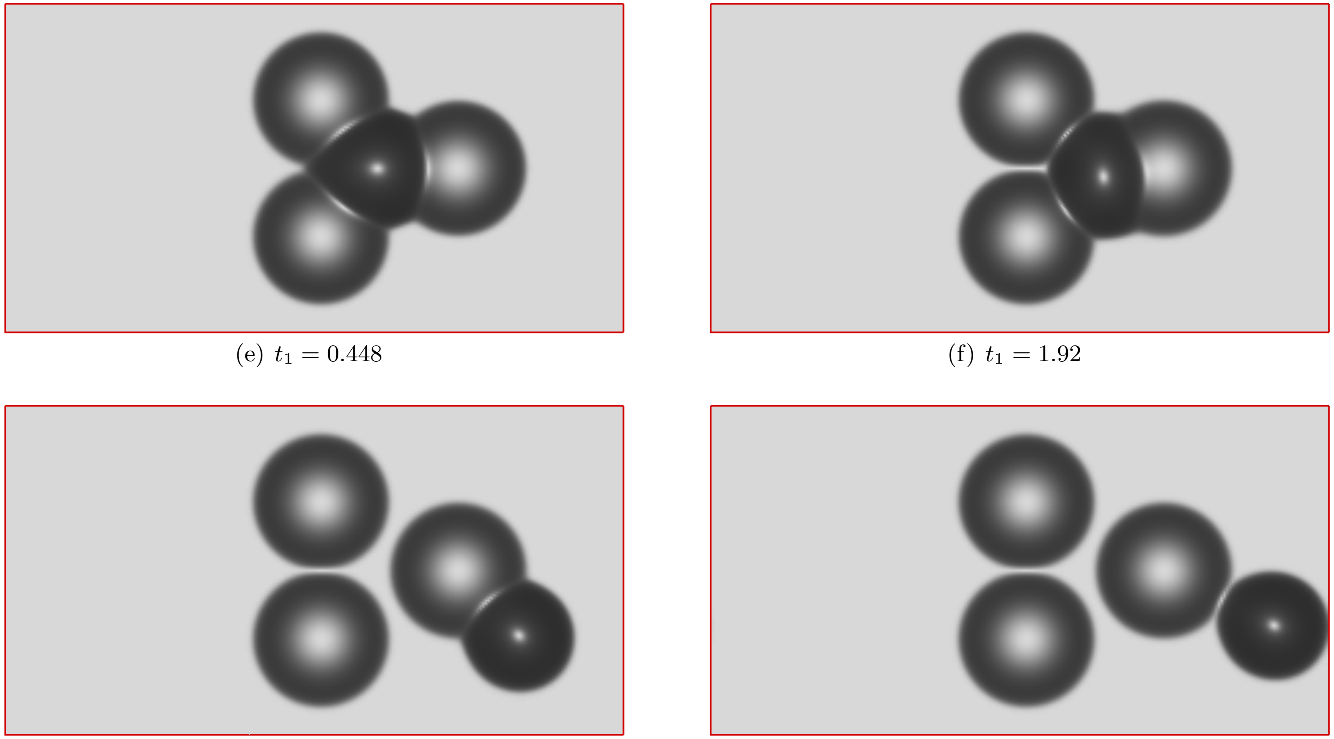

(e) $t_1 = 0.448$

(f) $t_1 = 1.92$

(g) $t_1 = 2.688$

(h) $t_1 = 2.848$

Figure 5.7 cont. Typical solution of a single droplet interacting with roughness elements, moving around the roughness elements and leaving the roughness field when driven by air and with a large disjoining pressure.

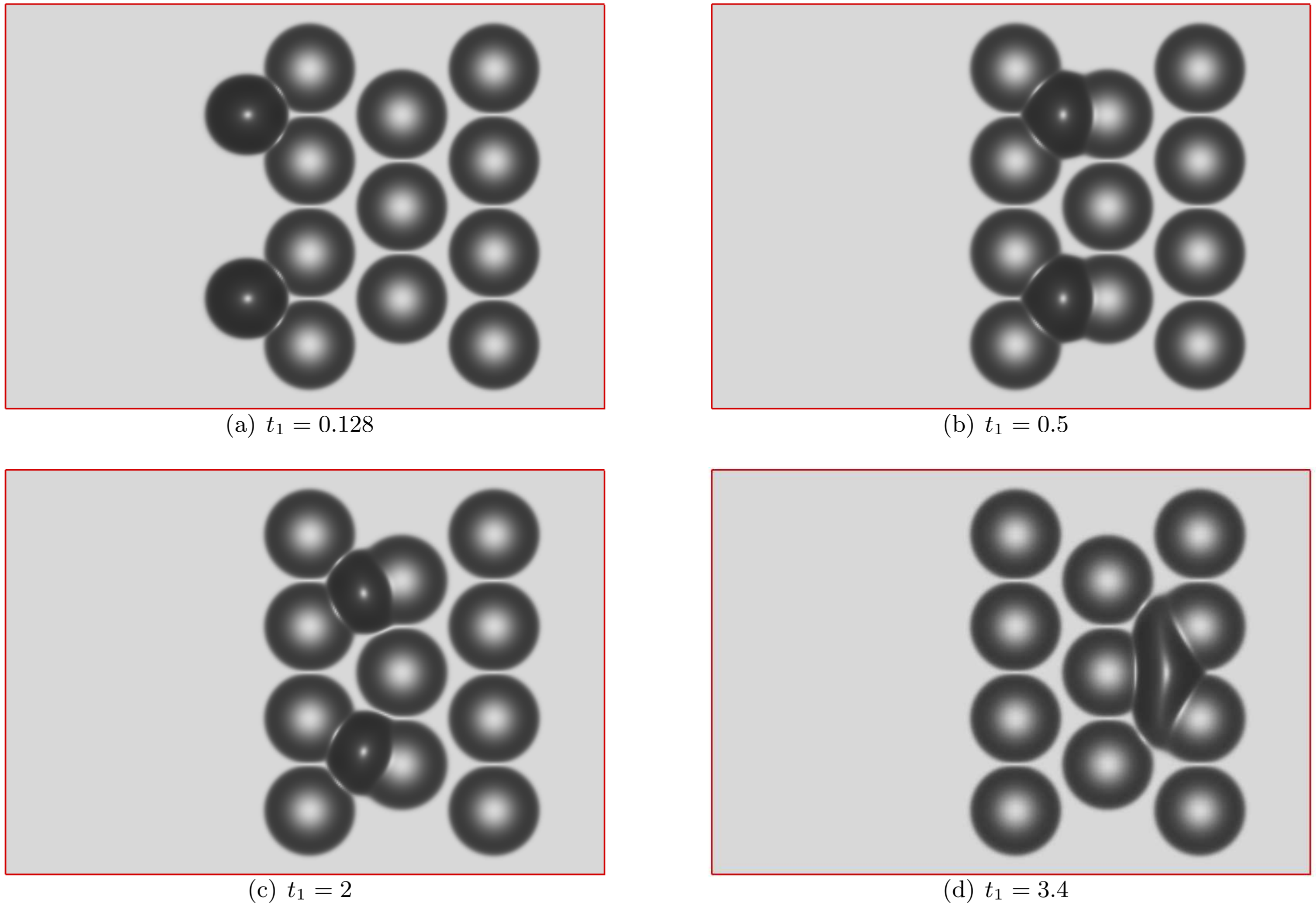

(a) $t_1 = 0.128$

(b) $t_1 = 0.5$

(c) $t_1 = 2$

(d) $t_1 = 3.4$

Figure 5.8 Typical solutions of droplets driven by air through an offset roughness field with a large disjoining pressure, where two droplets are stopped by roughness elements and later merge.

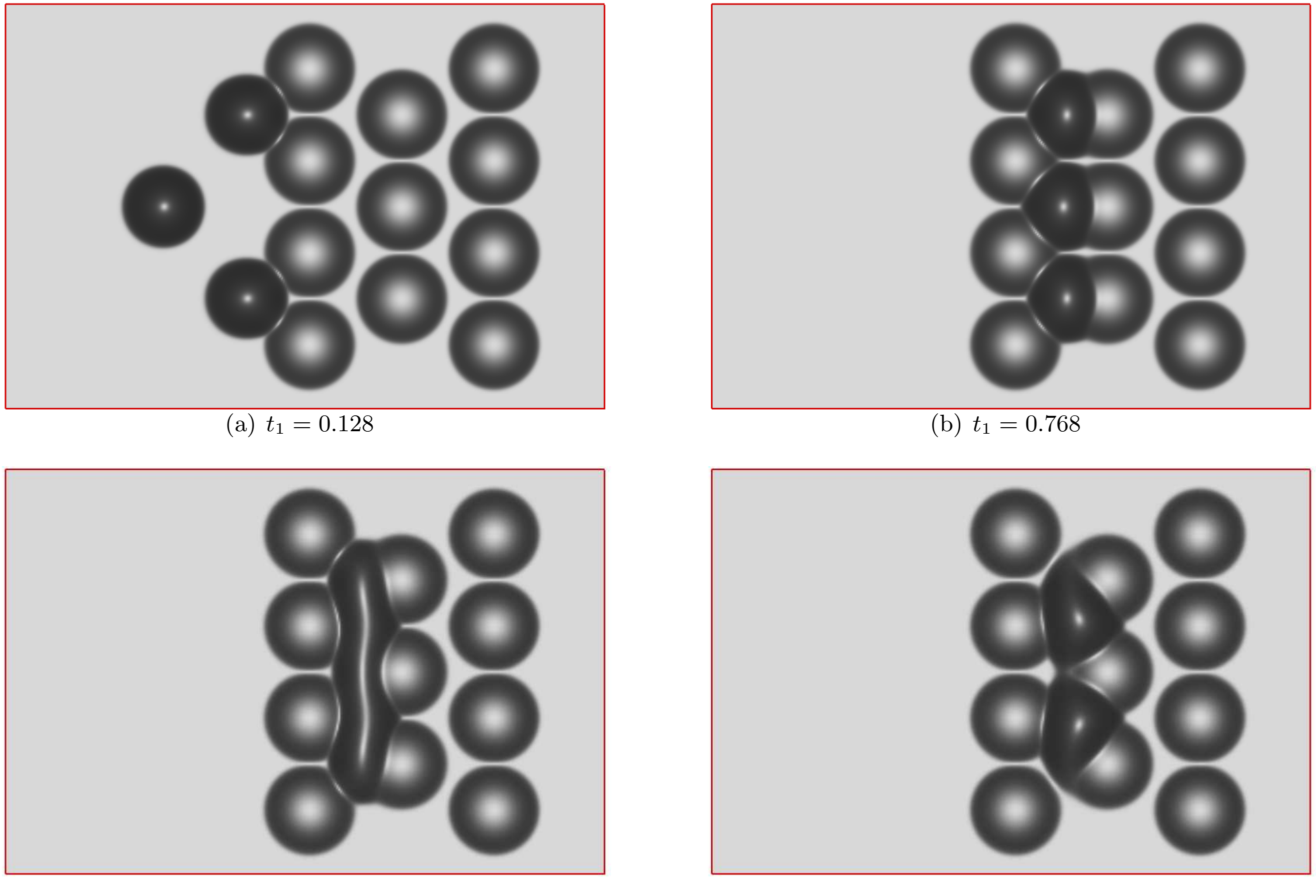

(a) $t_1 = 0.128$

(b) $t_1 = 0.768$

(c) $t_1 = 0.896$

(d) $t_1 = 0.96$

Figure 5.9 Typical solution of droplets driven by air through an offset roughness field with a large disjoining pressure, where the droplets interact with roughness elements, merge together and separate into two droplets.

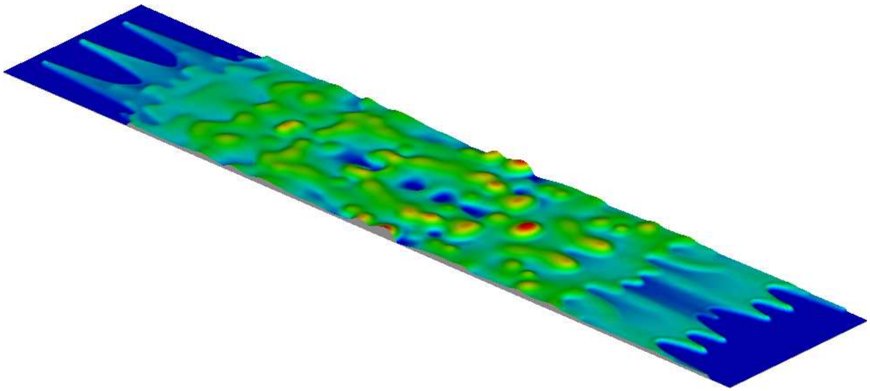

(a) Coefficient $B_m = B_n = 0$

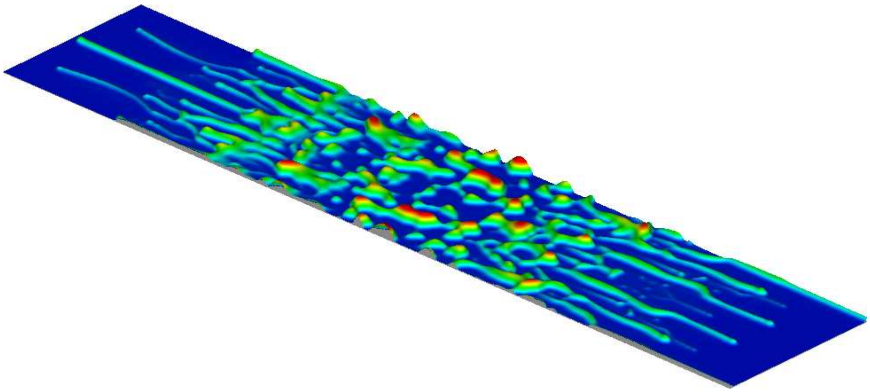

(b) Coefficient $B_m = B_n = 20$

Figure 5.10 Comparison of the film, droplet and rivulet patterns as water is driven by air near a stagnation line with/without the disjoining pressure model with $(m, n) = (3, 2)$, $\delta = 0.01$ and $\lambda = 2X$.

figure 5.10(b). With a disjoining pressure model, more isolated droplets are observed, and the droplets tend to remain near the stagnation line, pile together, and interact with each other to form well-defined meandering rivulets.

5.3 A new disjoining pressure model

5.3.1 Surface thermodynamics of droplets on precursor films

A droplet on a dry surface is shown in figure 5.11, where the contact lines (in two-dimensional situations) are the red points in this two-dimensional schematic diagram. The

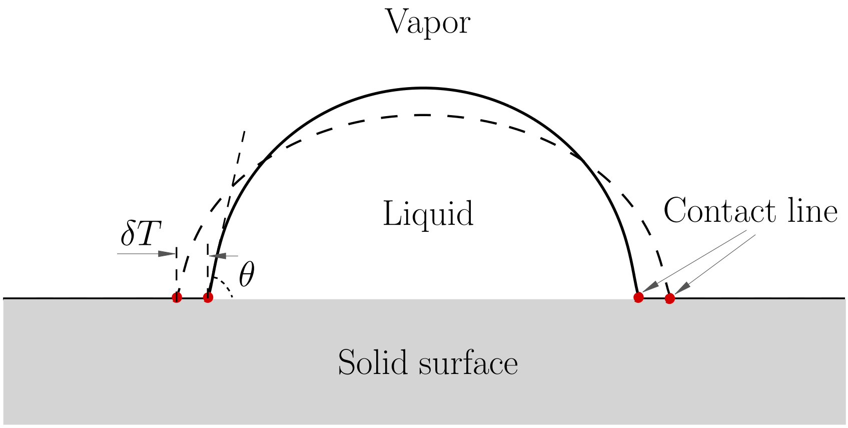

Figure 5.11 A virtual variation of a droplet on dry surface from an equilibrium state.

contact angle is θ and the geometry is symmetric when the driving force is zero in the streamwise direction and gravity is neglected. The symbol δT is the virtual displacement of the contact lines. These models (see Laplace (1806) and Young (1805)) can be derived from the Helmholtz free energy using a virtual displacement method (see Johnson (1950); Roura (2004, 2005); Lanczos, (1966)). The Laplace equation (see Laplace (1806)) is

$$P_L - P_V = \gamma_{LV}\left(\frac{1}{r_1} + \frac{1}{r_2}\right), \tag{5.35}$$

where P_L and P_V are the pressure in the liquid and vapor phases, respectively. γ_{LV} is the surface tension between the liquid and vapor phase, i.e. on the liquid droplet surface. r_1 and r_2 are the principal radii of the droplet shape. The Young equation (see Young (1805)) is,

$$\gamma_{LV} \cos\theta = \gamma_{SV} - \gamma_{SL}, \tag{5.36}$$

where γ_{ij} is the surface tension between the *ith* phase and the *jth* phase, and the indices i, j are those of the liquid, vapor and solid phases. Johnson (1950) pointed out that the energy of a droplet is a minimum value when both the Laplace and Young equations are satisfied, when the droplet is on a dry solid surface.

However, Hardy (1919) found that a precursor liquid layer is created during the droplet deformation before the droplet moves (also see Beaglehole (1989); Cazabat (1987); de Gennes (1985)). Such a precursor layer clearly exists in the experimental photos taken by Albrecht, Otto & Leiderer (1992). The model of a droplet on a precursor film shown in figure 5.12 is used in this study, where the solid surface is covered by a precursor film with a thickness δ. The assumptions of this model are:

1. the rigid solid surface is smooth, isotropic, homogeneous, and insoluble in the liquid;
2. the film, vapor and solid surface are simple thermodynamic phases, respectively;
3. these three phases are homogeneous and not subject to any chemical or interactions with external fields.

When the solid surface is covered by a thin precursor layer, the contact line/point shown in figure 5.11 becomes the nominal contact line/point shown in figure 5.12. The contact angle is defined as the angle between the tangent line of the macroscopic droplet shape and the flat precursor film surface. The same model was used by Li & Neumann (1991) to present the surface thermodynamics of a droplet on a precursor film (also see Neumann & Spelt (1996)). One mechanical equilibrium condition derived by Li & Neumann (1991) is

$$\Pi = p_v, \tag{5.37}$$

where p_v is the pressure of the bulk vapor phase, and Π is the disjoining pressure named by Derjaguin & Churaev (1976) (also see Frumkin (1938)). The vapor pressure p_v in the air is bigger than zero. However, the classical disjoining pressure, i.e. the long-range van der Waals force shown in equation (5.32), is less than zero when the dimensionless coefficients B_m and B_n of repulsive and attractive terms in (5.32) are the same. The second disadvantage of the classical disjoining pressure model (5.32) is that an effective length of the precursor layer should be introduced into the analysis and simulation if the film thickness goes to zero (see Owens *et al.* (1978); Mitchell & Richmond (1974); Glasner (2003); Butt & Stark (2005)). To avoid these problems in the classical disjoining pressure models, e.g. equation (5.32), a new model is presented here,

$$\Pi = B\left[T\left(F\right)^{m} - T\left(F\right)^{n}\right], \tag{5.38}$$

where the function $T\left(F\right)$ is a hyperbolic tangent function of the droplet thickness, i.e.

$$T\left(F\right) = \tanh\left[\left(\frac{\delta}{F}\right)^{k}\right], \tag{5.39}$$

where k is usually defined as an integer, though it might be a real number. Note that $k = 2$ is used in this study. The profiles of the new and classical models are plotted in the figure 5.13, where the green line is the profile of the new disjoining pressure model, and the red line is the profile of the classical disjoining pressure model. The classical disjoining pressure Π goes to negative infinity as the the thickness F goes to zero, whereas the new disjoining pressure Π goes to zero. This means that (5.38) can be applied to a droplet on a dry solid surface without any extra assumptions, such as the effective film thickness. The values of both models become the same, and will approach zero, when the film thickness F goes to infinity. Figure 5.14 shows the difference between the functions $y = \frac{1}{F}$ and $y = \tanh\left(\frac{1}{F}\right)$, which also shows the tendency of the new and classical pressure models to approach each other as $F \to \infty$.

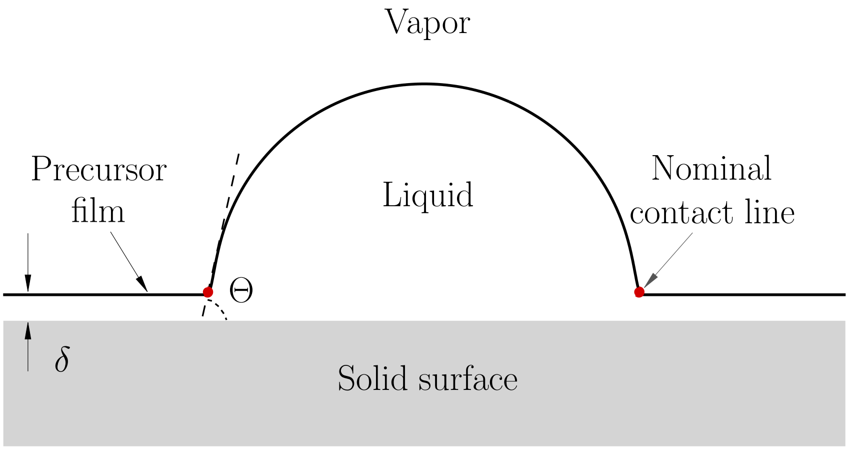

Figure 5.12 Schematic diagrams of droplets on a wet surface when the precursor layer thickness is δ

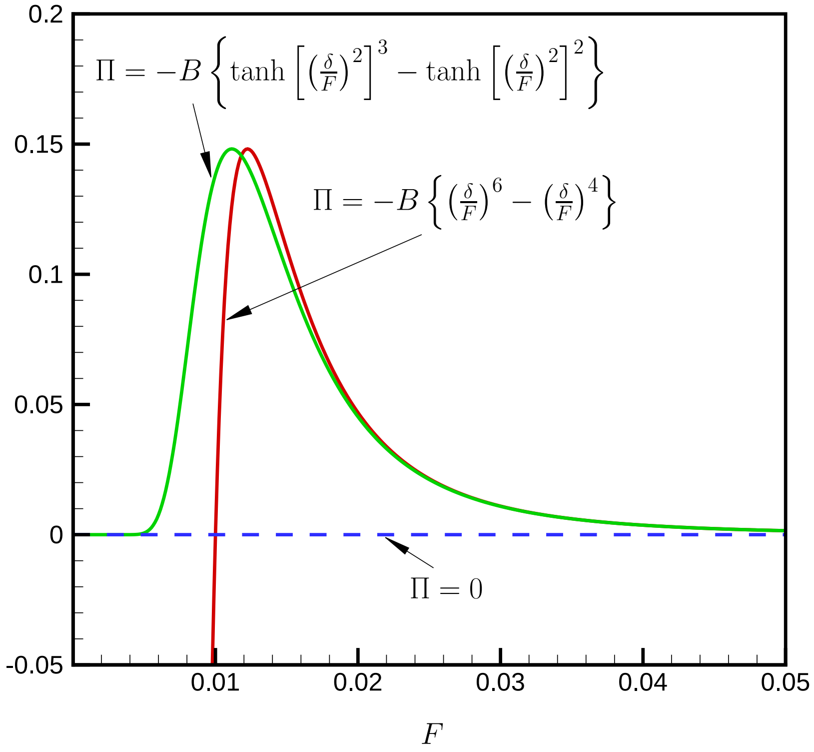

Figure 5.13 The comparisons between the classical disjoining pressure model (5.32) and the new model (5.38). The coefficients are $B = 1$ in both models. Note that the parameters m, n and k in these two models are arbitrarily selected simply to illustrate the qualitative difference between the models.

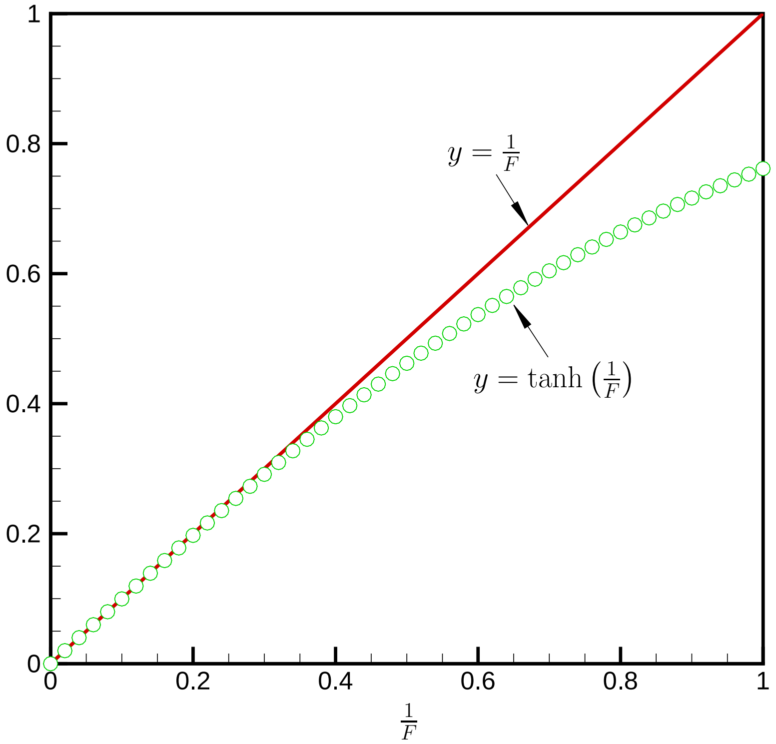

Figure 5.14 A comparison of the difference between $y = \frac{1}{F}$ and $y = \tanh\left(\frac{1}{F}\right)$

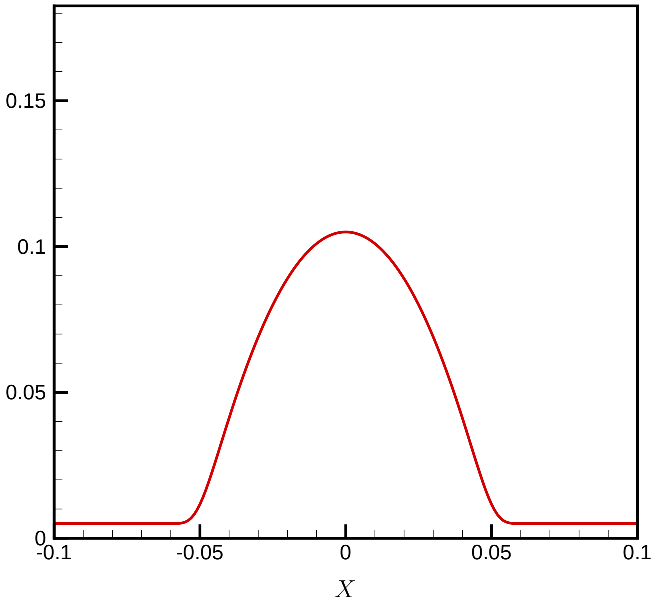

(a) Initial droplet shape

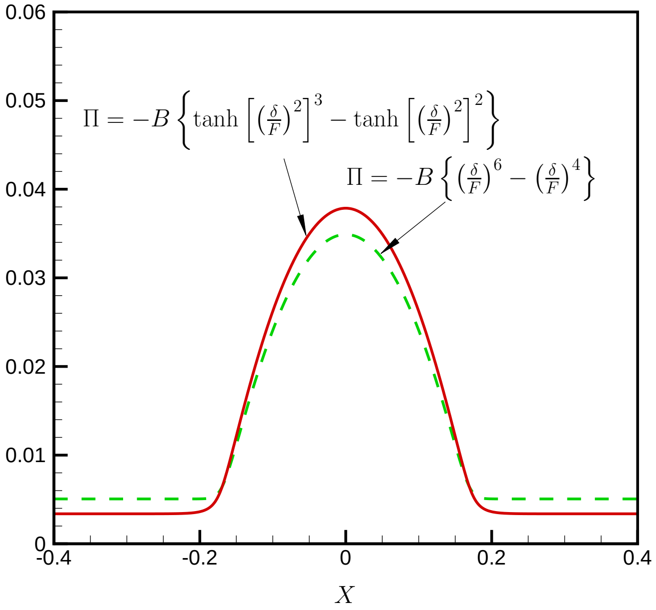

(b) Steady droplet shape as $T \to \infty$

Figure 5.15 The typical solutions of a droplet on a precursor layer without any driving force when the new disjoining pressure model and the classical disjoining pressure model are used. Note that the initial droplet profile is shown in figure 5.15(a).

Consider an example of a droplet lying on a precursor layer, with the driving forces zero everywhere. Both the classical disjoining pressure model and the new disjoining pressure model are used in the simulation. The initial droplet shape is shown in figure 5.15(a), which is approximately a parabola. The steady solutions using the two disjoining pressure models are shown in figure 5.15(b). The droplet profile with higher maximum height is the solution using the new disjoining pressure (5.38). The lower one is the solution using the classical disjoining pressure model (5.32). Figure 5.15(b) shows that the classical disjoining pressure model increases the precursor film thickness when the droplet reaches its steady state, while the new disjoining pressure model decreases the precursor film thickness. Moreover, the final droplet geometries are slightly different when the classical and new disjoining pressure models are used.

5.3.2 Inhomogeneous disjoining pressure empirical model

Often droplets or beads don't move when they are statically deposited on a real solid surface, such as glass windows and metal surfaces. However, the droplet will move if a sufficiently large driving force is applied. A formula is constructed here to simulate a stationary droplet sticking to a solid surface if the droplet is driven by air or gravity using the new disjoining pressure model (5.38). The coefficient of the disjoining pressure is a function of the film thickness and its derivatives, i.e. the coefficients of inhomogeneous disjoining pressure model (5.45) are taken to be

$$B = B_0 + \triangle B \cdot \left[U\left(F\right) + W\left(F\right) \right], \tag{5.40}$$

where

$$U\left(F\right) = \tanh\left[-\beta F_x \left(\frac{\delta}{F} \right)^k \right] \tag{5.41}$$

and

$$W\left(F\right) = \tanh\left[\beta \left(F_x\right)^2 \left(\frac{\delta}{F} \right)^k \right]. \tag{5.42}$$

With this formula, the edge of the droplet on the precursor film will be detected automatically. If a proper value of the parameter $\triangle B$ is chosen then the droplet will become stationary.

Another possible pair of formulae for W and U are

$$U\left(F\right)=\tanh\left[-\beta FF_x\left(\frac{\delta}{F}\right)^k\right] \tag{5.43}$$

and

$$W\left(F\right)=\tanh\left[\beta\left(F_x\right)^2\left(\frac{\delta}{F}\right)^k\right]. \tag{5.44}$$

Note that both of these two pairs of coefficients were tested in the numerical simulation, and both could simulate stationary droplets on a solid surface. However, the grid independence study shows that the grid size must not be too large. To limit the discussion, one pair of inhomogeneous coefficients W and U, i.e. (5.41) and (5.42), is applied to the film equation, e.g. equation (5.27) and (5.29). In the following simulations, the disjoining pressure is added to the film equation in the form

$$\frac{\partial F}{\partial t}+\frac{\partial}{\partial X}\left(\lambda_X\frac{F^2}{2}-\frac{\partial P}{\partial X}\frac{F^3}{3}\right)+\frac{\partial}{\partial X}\left(\lambda_Z\frac{F^2}{2}-\frac{\partial P}{\partial Z}\frac{F^3}{3}\right)=0, \tag{5.45}$$

where

$$P=-\Sigma K-\Pi=-\Sigma\left(\frac{\partial^2 F}{\partial X^2}+\frac{\partial^2 F}{\partial Z^2}\right)-\Pi, \tag{5.46}$$

$$\Pi=\left[B+\Delta B\left(U+W\right)\right]\cdot\left[T\left(F\right)^m-T\left(F\right)^n\right], \tag{5.47}$$

$$T\left(F\right)=\tanh\left[\left(\frac{\delta}{F}\right)^k\right], \tag{5.48}$$

and m, n and k are defined previously.

5.4 Numerical solutions and comparisons

An empirical model, i.e. film equation (5.45) and (5.46) together with the inhomogeneous coefficient (5.47), is presented in the above sections. To validate this model, droplets on an inclined surface and droplets near a stagnation line at the leading edge of an airfoil are simulated using an ADI-Iteration method and pseudo-linear method discussed in appendices A and B. Appendix A gives the numerical algorithm for the two dimensional film equation, which is solved as a system of pentadiagonal difference equations. The boundary conditions in both the streamwise and spanwise directions are periodic, while the non-periodic boundary conditions are used in the film front direction of motion. The difference equations of the inhomogeneous coefficients (5.47) are given in Appendix B, which are linearized using the functional derivative (see Oron & Bankoff (1999)).

A. Comparison with Hansman & Turnock's experiment

The experiment of Hansman & Turnock (1988) shows that the average of the advancing and receding contact angle depends on temperature. In their experiment, the inclination angle is 30^o, and the droplet's volume is increased by continuously injecting water into the droplet until the droplet moves. Rothmayer & Tsao (2001) applied the above experiment to a model that simulates droplet motion near a stagnation line. In this section, a droplet on an inclined surface is simulated using the empirical formulae (5.40), (5.43) and (5.44), when the advancing and receding contact angles are different.

In the experiment of Hansman & Turnock (1988), the contact angle of a droplet on an inclined surface was not presented as a function of the droplet geometrical parameters, such as the droplet volume, height or diameter. Instead, Hansman & Turnock (1988) found a relation between the temperature and contact angles when the droplet was driven by gravity. This process is simulated in figures 5.16 to 5.20. The solutions are parametrized by a variable, i.e. ΔB, in the empirical formulae 5.40, 5.43 and 5.44, because ΔB is analogous to temperature in the Hansman & Turnock's experiment (1988).

Figure 5.16(a) shows the definition of the contact angle used in this study. When a droplet is on an inclined surface, it is driven by the gravity force. The arrow with the acceleration g shows the direction of the driving force. The droplet deforms but does not move away from the original position, providing that it is sufficiently small. When the droplet is almost stationary, the receding/advancing contact angles, i.e. Θ_R and Θ_A can be measured in the macroscopic view, which is indicated with the tangent lines near the contact points. Figure 5.16(b) shows the definition of droplet height and diameter. Initially, a symmetric parabolic shape is placed on a surface which is inclined to an angle of 30^o. The volume of the droplet is calculated using the initial droplet height and diameter. Therefore, the initial droplet height is the only parameter needed to determine the droplet volume. The effect from the precursor film thickness, δ, is negligible in the volume calculation, because δ is much smaller than H. Note that the approximate parabolic shape in this study is given by equation (2.34).

Figure 5.17 shows the calculation of the contact angle, where the angle is defined as the angle between the tangent line at any point on the droplet surface and the x-axis, i.e.

$$\Theta = \arctan\left(\frac{\partial F}{\partial X}\right). \tag{5.49}$$

The receding contact angle, Θ_R, and the advancing contact angle, Θ_A, in figure 5.18, at initial $Height = 1$ in this case, are defined as the absolute values of the maximum and minimum values shown in figure 5.17, respectively.

Figure 5.18(a) shows the difference between Θ_A and Θ_R, which is transformed into a function of temperature T. As defined in figure 5.17(a), Θ_A is the advancing contact angle, and Θ_R is the receding contact angle. The solid squares are the experimental results, which are obtained from the Hansman & Turnock's experimental data (1988). The line is the least squares linear fit of the experimental results as well as the numerical results (see discussion below), where the parameter ΔB used in the disjoining pressure model is transformed to the temperature T through the equation (5.50)

$$\Delta B = -12.27866 \cdot T - 13.64195. \tag{5.50}$$

Note that the least squares linear fit of the contact angle difference for the numerical data is

$$\Theta_A - \Theta_R = 0.10076 \cdot \Delta B + 2.69979, \tag{5.51}$$

while for the experimental data, it is

$$\Theta_A - \Theta_R = -1.23724 \cdot T + 1.32519. \tag{5.52}$$

Equation (5.50) is the solution of equations (5.51) and (5.52). Note that equation (5.50) is selected to give exact agreement with the experimental data. The "numerical data" in figure 5.18 are the actual results obtained when using (5.50) in the simulations. Figure 5.18(b) shows the average advancing and receding contact angles of the water droplet, i.e. $(\Theta_A + \Theta_R)/2$.

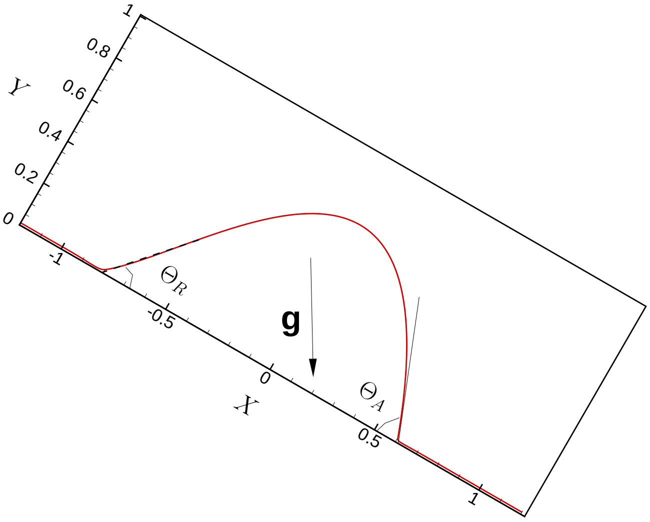

(a) Contact angle

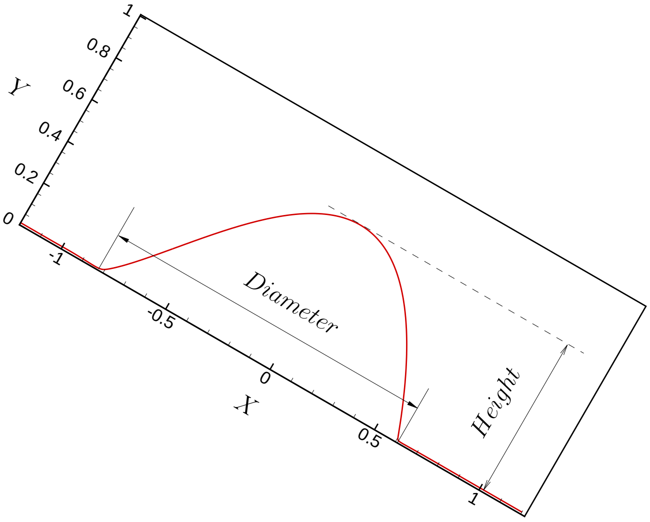

(b) Diameter and height

Figure 5.16 Example of the contact angle, height and diameter computed in this study.

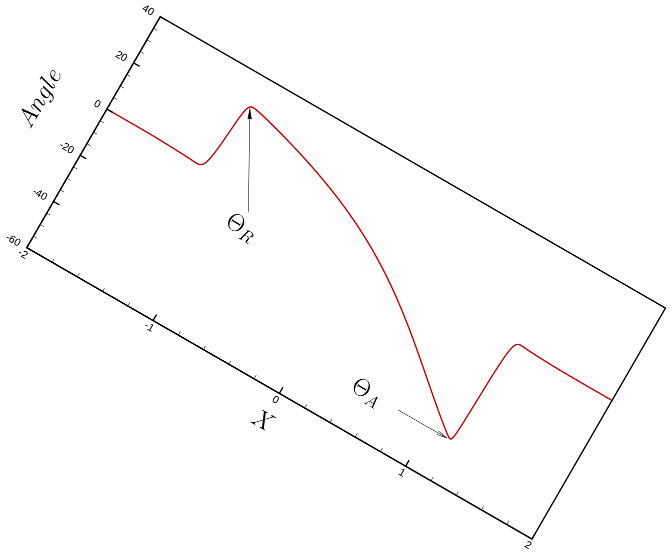

Figure 5.17 Diagram of the contact angle calculation in this study.

When the relation 5.50 is applied into the linear fit of the numerical results, the average of the advancing and receding contact angles becomes a function of the temperature, i.e.

$$(\Theta_A + \Theta_R)/2 = -1.40950 \cdot T + 21.93939, \tag{5.53}$$

while the least square linear fit of the experimental results is

$$(\Theta_A + \Theta_R)/2 = -1.60041 \cdot T + 9.89117. \tag{5.54}$$

Note that two formulae similar to equations (5.52) and (5.54) are used by Rothmayer & Tsao (2001), though the coefficients are slightly different.

Figure 5.19 shows the droplet shapes in the simulation when they are placed on an inclined surface and driven by gravity. All numerical data shown in this comparison are found from these droplet shapes, and the least squares linear fit all depends on this data. As the droplet size changes the parameter ΔB changes, which is analogous to the temperature T, as shown in figure 5.20.

Algorithm for computing bead runback:

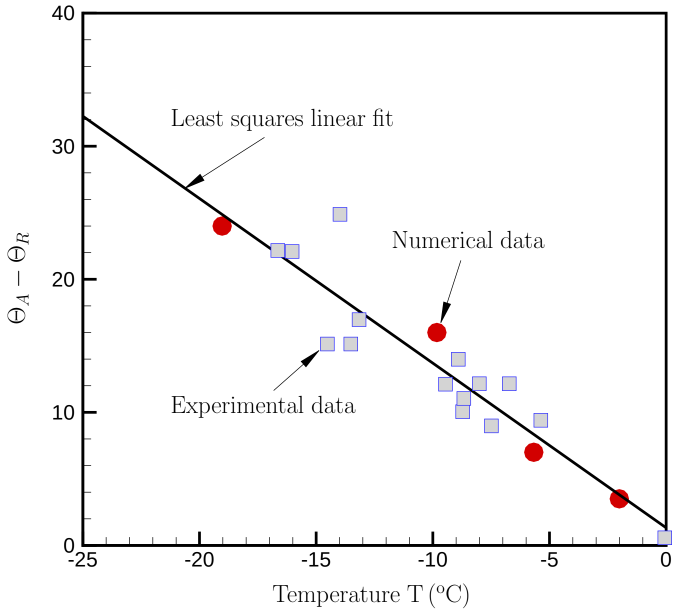

(a) Advancing and receding contact angle hysteresis

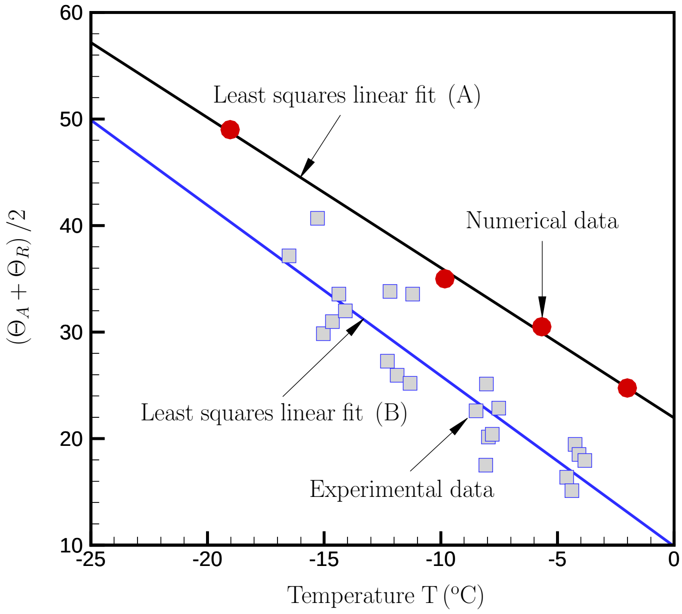

(b) Average of advancing and receding contact angles

Figure 5.18 The advancing and receding contact angles when the empirical formulae (5.40), (5.43) and (5.44) are used to simulate droplets on an inclined surface. Note that the least squares linear fit (A) is from equation (5.53), while the least squares linear fit (B) is from equation (5.54).

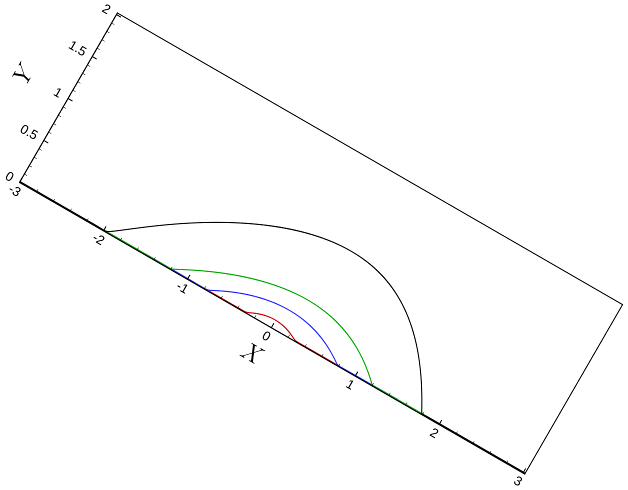

Figure 5.19 Droplets calculated with the new disjoining pressure model, i.e. (5.45), (5.46) and (5.47)

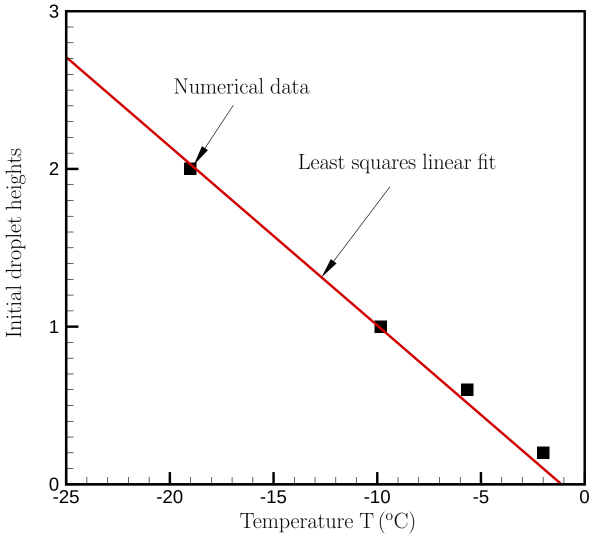

Figure 5.20 The least squre linear fit to show the relation between the droplet heights and the temperature in the experiment by Hansman & Turnock (1988)

1. Initialize a droplet on an inclined surface.

   A finite volume droplet is created on an inclined surface, where the inclination angle is 30 degrees. The initial droplet shape is approximately parabolic. The figure 5.16(a) shows the definition of the advancing and receding contact angles. The definition of the droplet height and diameter is shown in figure 5.16(b).

2. Search for an appropriate value of ΔB.

   For a given droplet volume, ΔB is found so that the droplet remains stationary on the inclined surface for a long time. Because the droplet continues deforming, the stationary status is only reached after a long time if a correct ΔB can be found.

3. Calculating the contact angles

   The advancing and receding contact angles are calculated through the definition in equation (5.49). These are also shown in figure 5.17(a).

4. Changing the droplet volume

   The droplet volume is gradually increased, and steps 3 and 4 are repeated for each droplet. The contact angles and droplet volume are determined from the last solution which remaining steady.

5. Data fitting and comparison

   A least squares linear fit is used for the data fitting. The contact angle is a function of ΔB, which is analogous to temperature in the Hansman & Turnock's experiment. As shown in figures 5.18, two equations are found from the least squares fit. One is used for the transformation between the temperature T and the variable ΔB. The comparison between the experimental data and numerical data is also shown in figures 5.18.

B. Comparison with Olsen & Walker's experiment

To validate the empirical formulae, a comparison is made with the experimental data of Olsen & Walker (1987), which are above freezing experiments of droplet runback on a smooth surface. The sizes of the water droplets in the experiment are given at the different distance from the stagnation line, which are used as the initial input in the simulations. A fixed ΔB is used in this comparison, which amounts to fixing the contact angle of the droplets (note that in Olsen & Walker's (1987) experiment the contact angles were approximately constant). The steps used in the comparison are given below. The precursor film thickness is 0.01 in all simulations, which is negligible in the volume calculation. The parameters $m = 3$ and $n = 2$ in equation (5.38) are used in this study, though others could be used.

To translate the diameters from a dimensionless variable D to a dimensional variable D^*, the scales in section 2.2 are used. For the thin water film, the scale Δ is less than the condensed layer value of Rothmayer & Tsao (2000) but larger than the near wall Navier-Stokes scale, i.e.

$$Re^{-3/4} \ll \Delta \ll Re^{-9/14} \sigma^{-3/7}. \tag{5.55}$$

With $\sigma = \Sigma D_{aw}^{-1/2}$, $Re = 10^4$ and $D_{aw} = 10^{-3}$, the inequality (5.55) becomes

$$10^{-3} \ll \Delta \ll 1.1788 \times 10^{-2}. \tag{5.56}$$

The arithmetic average of the scale Δ is used to estimate the droplets diameter transformation, i.e.

$$\overline{\Delta} = \frac{1}{2}\left(1.1788 \times 10^{-2} + 10^{-3}\right) \approx 6.4 \times 10^{-3}. \tag{5.57}$$

The characteristic length L^* is the diameter of the nose at the leading edge of an airfoil, i.e. $L^* = 3.8\, cm$ (see Olsen & Walker (1988)). The final diameter transformation becomes

$$D^* = L^* \Delta D \approx 3.8 \times 10^{-2} \times 6.4 \times 10^{-3} \times D = 243.2 \cdot D\, \mu m. \tag{5.58}$$

The algorithm used in the comparison with Olsen & Walker's experiment is

1. Initialize a droplet at the leading edge of an airfoil

   A finite volume droplet is created on a flat surface, and the droplet shape is approximately parabolic. The droplet volume is calculated from the experimental value. For example, at $s^* = 9mm$, the droplet diameter is about $160\mu m$, and the ratio of its height and diameter is 0.26 (see Olsen & Walker (1988)). A dimensionless droplet is placed on flat surface using the non-dimensionalization and the scale transformation.

2. The shear stress λ

   An empirical formula based on the laminar flow is used for the shear stress calculation (see Rothmayer & Tsao (2001)), i.e.

   $$\lambda = 3.19 \left\{ 1.66 \left(\frac{s^*}{19mm} \right) - \left(\frac{s^*}{19mm} \right)^2 \right\} \tag{5.59}$$

   At $s^* = 9mm$, the shear stress is $\lambda = 1.793$. A shear driven thin film equation is solved together the empirical formula.

3. Set parameters in the empirical formula

   $B_0 = 100$ is fixed for all simulations. ΔB is an unknown constant. A droplet at $s^* = 9mm$ is first simulated using a series of ΔB. For example, an initial droplet shape (rescaled dimensionless $H = 1.404$) is shown as a solid red line in figure 5.21(a). $\Delta B = 326$ in the empirical formula is used in this simulation. Due to the shear stress and the capillary force, the droplet starts to deform as $t > 0$, and it eventually becomes stationary as t goes to ∞. The stationary solution is the green line shown in figure 5.21(a). Figure 5.21(b) shows that the deformation number ζ of a typical solution is a function of time. The definition of ζ is shown in equation (5.60). When $t < 1$ the droplet deformes a lot. When $t > 1$ it becomes almost stationary. The same ΔB, i.e. $\Delta B = 326$, is fixed for all other simulations in this comparison. The deforming time, i.e. $\tau_d = 1$, in this simulation is used as a reference time to evaluate the deformation time of the other simulations in this comparison.

4. The droplet deformation and displacement

   It is known that the droplet deforms anytime and anywhere, but it is hard to observe such a micro deformation in short time. In this study, an equation (5.60) is used to measure the amount of the droplet deformation and displacement:

   $$\zeta = \frac{\int_{-\infty}^{+\infty} |F(X,T) - F(X,t=0)| \, dX}{\int_{-\infty}^{+\infty} F(X,t=0) dX} \tag{5.60}$$

   Note that $\zeta = 0$ is the initial state. One limit solution as $\zeta = 1$ is the droplet becomes completely flat and the thickness approaches zero, but that will not happen in this

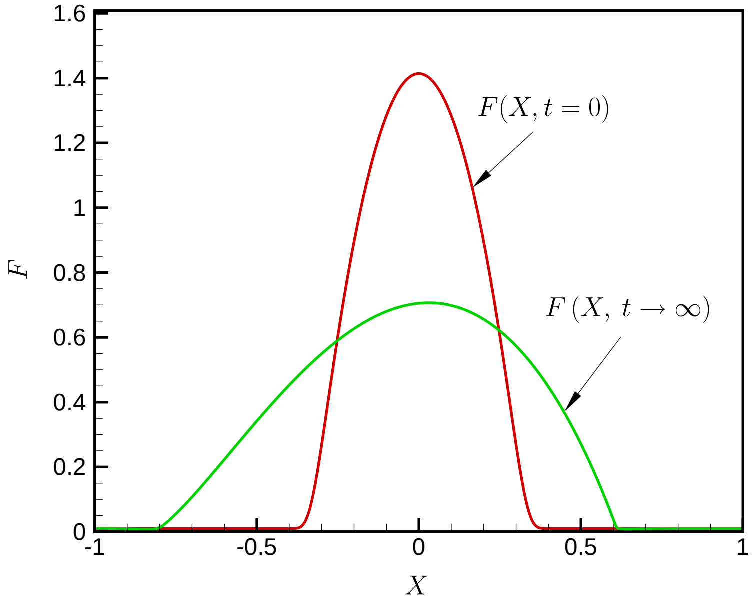

(a) Typical stationary droplet

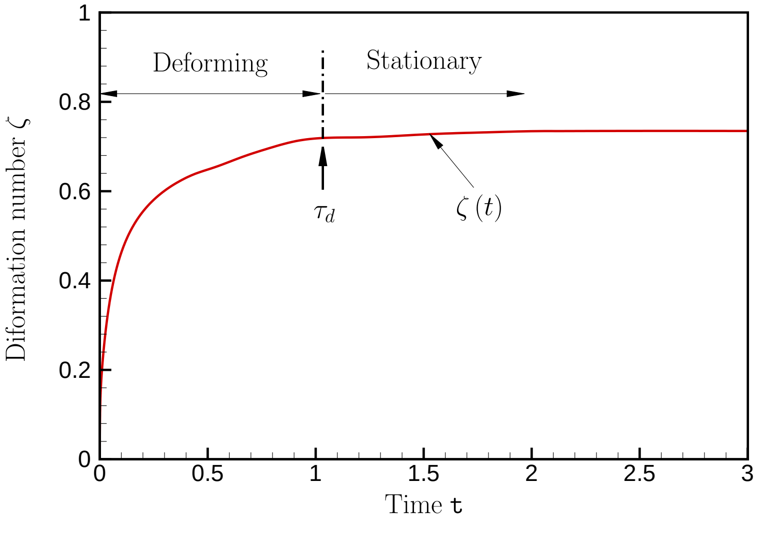

(b) Typical $\zeta\,(t)$ profile

Figure 5.21 Typical deformation number ζ of a single droplet driven by a shear stress $\lambda = 1.793$. Note that $\Delta B = 326$ is used in the empirical formula. τ_d is the deformation time, i.e. $\frac{\zeta(t=\tau_d)}{\zeta(t\to\infty)} \geq 0.95$. ζ is defined in equation (5.60).

comparison. $\zeta = 2$ occurs when the droplet completely moves away from its initial location, which is schematically shown in the diagram 5.22. In this study, the droplet is assumed to be stationary if the deformation number ζ is in the following range while the deformation time is within a time interval $(\tau_d - \Delta\tau) \leq t \leq (\tau_d + \Delta\tau)$, i.e.

$$(\zeta_s - \Delta\zeta) \leq \zeta \leq (\zeta_s + \Delta\zeta)\,, \tag{5.61}$$

where the time τ_d is determined by the step 3, at which time the deforming number ζ_s is $\zeta_s = \zeta\,(t = \tau_d)$. $\Delta\tau$ is a fixed time interval, which is kept constant in this comparison. Similarly, $\Delta\zeta$ is a fixed value for all other simulations.

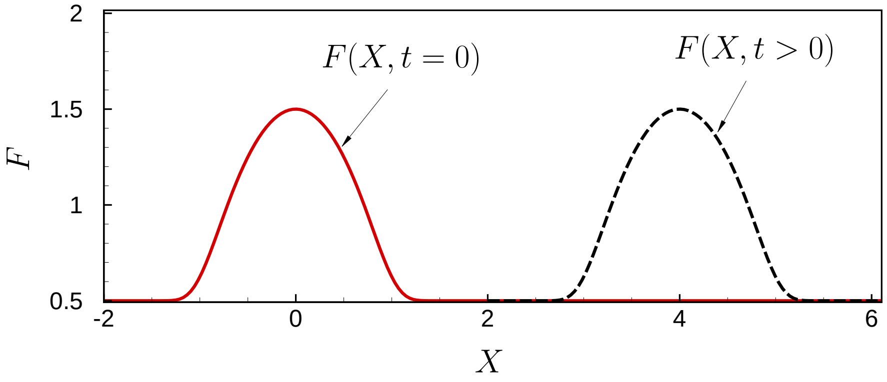

Figure 5.22 Diagram of a solution which would produce a deformation number $\zeta \approx 2$, as a droplet moves away from its initial location.

5. Droplets at the same location s^*

   Different size droplets are simulated at the same location, and they are driven by the same shear stress λ. If the droplets deformation number ζ is within the range defined in step 4, the droplets are stationary. Otherwise, they will be marked as moving droplets.

6. Droplets at the different locations s^*

   At different locations, the shear stress λ is different. Several different size droplets are again simulated using the same parameters in the empirical formula but using the different shear stress.

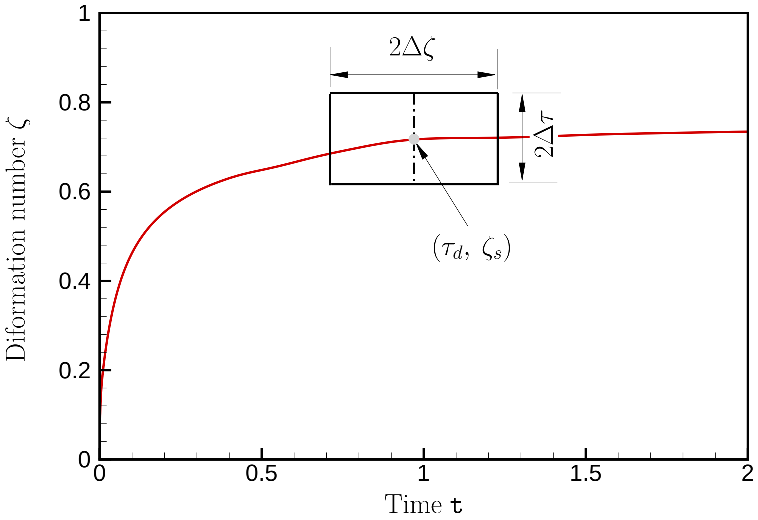

Figure 5.23 A schematic diagram of the parameter window used to define a pseudo-stationary droplet. For example, a droplet is marked as a stationary droplet if the deformation time is within the interval, $(\tau_d - \Delta\tau) \leq t \leq (\tau_d + \Delta\tau)$, and the deforming number is within the interval, $(\zeta_s - \Delta\zeta) \leq \zeta \leq (\zeta_s + \Delta\zeta)$ at the same time.

7. Comparison with the experiment

   After steps 1 to 6 are finished, the numerical diameters are compared with the experimental results, which are shown in figures 5.24. Figure 5.24(a) shows the droplet diameters at different locations when those droplets are driven by the shear stress near the leading edge of the airfoil. The discrete diameters at the different locations show that the droplets can be stationary when the criteria (5.61) is used. $\Delta\tau$ is about 50% of τ_d, and $\Delta\zeta$ is about 10% of ζ_s shown in step "The droplet deformation and displacement". As the droplet size increases, the probability of moving away from its initial location becomes large. The large diameter drops will move first, though sometime the deforming number ζ is still small. Hence, the droplet profile, i.e. figure 5.24(b), is used to show the droplet motion. The reasonable trend of the droplet diameters at different locations is found when a series of different size droplets are simulated with one fixed parameter $\Delta B = 326$.

   In summary, it is convenient to use this empirical formula to simulate the droplets driven by the air shear stress when the parameter ΔB is a fixed number, provided that it is selected correctly. The computational cost of this simulation is quite high.

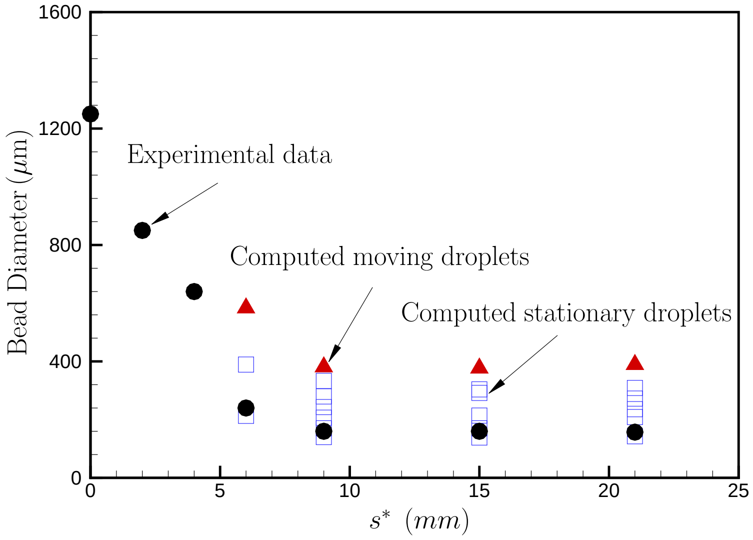

(a) Diameters of droplets along the Olsen & Walker airfoil

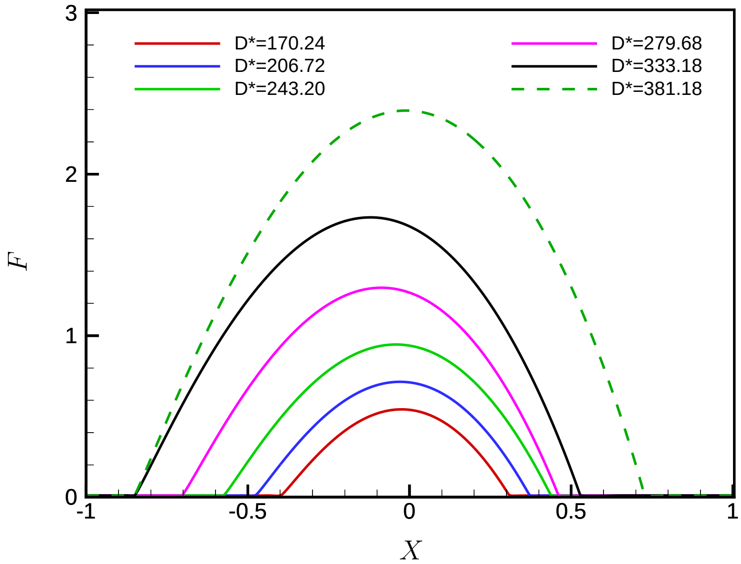

(b) Droplet profiles at a distance $s^* = 9$ (mm)

Figure 5.24 Comparison between Olsen & Walker' experimental data and the numerical solutions when the empirical formulae (5.40), (5.43) and (5.44) are applied.

CHAPTER 6. Conclusions

An asymptotic theory is applied to thin water films flowing past small roughness when the thin viscosity-dominated films are driven by the air shear stress in the context of a high Reynolds number boundary layer theory. Some properties of this model are explored in different settings, such as transport and interaction of water in a roughness field, perturbed heat transfer of film/roughness combinations and films with surfactant. For the water transport around the surface roughness, different roughness patterns induce the different water pooling as the water mass is redistributed through the interactions. When the ambient leading order heat flux is fixed, the analysis shows the amount of change of the perturbed heat flux due to the non-uniform water surface though perturbed heat flux is not significantly effected. Based on a linear instability analysis, a general formula has been developed for the instability of film fronts and rivulet creation by film front perturbations and surface roughness. It also shows that rivulets can be formed from instabilities of very thin films. After analysis of bead runback near stagnation lines, it is found that the disjoining pressure model is required for the accurate simulation of water beads and rivulets. a new modified disjoining pressure model is developed together with an empirical formula, which is validated through comparisons with experimental data from aircraft icing tests.

APPENDIX A. ADI-Iterative method and its algorithm

This method is used in section 3.5, Instability of film fronts moving through surface roughness, and chapter 5 as well as water films and beads motion near a stagnation line.

A.1 Linearization and ADI-Iterative method

The thin film equation with a precursor layer is:

$$F_t + \bigtriangledown \cdot \left(\overrightarrow{\lambda} F^2\right) + \bigtriangledown \cdot \left(H\left(F\right) \bigtriangledown P\right) = 0, \tag{A.1}$$

where the coefficient $H\left(F\right)$ is $H\left(F\right) = \frac{1}{3}F^3$ and $P = -\bigtriangledown^2\left(F + r\right) - \Pi$. r is the surface roughness function, and Π is the disjoining pressure. The classical disjoining pressure $\Pi = -B\left[\left(\frac{\delta}{F}\right)^m - \left(\frac{\delta}{F}\right)^n\right]$ is used as the example here. Equation (A.1) is rewritten as

$$F_t = -g\left(F\right), \tag{A.2}$$

where the function $g\left(F\right)$ is $g\left(F\right) = \bigtriangledown \cdot \left(\overrightarrow{\lambda} F^2\right) + \bigtriangledown \cdot \left(H\left(F\right) \bigtriangledown P\right)$.

A general algorithm of the Crank-Nicolson method (see Crank J. & Nicolson P. (1947); Tannehill, Dale & Pletcher (1997)) is used in this study, i.e.

$$F^{n+1} - F^n = -\Delta t \cdot \left[\theta \cdot g\left(F^{n+1}\right) + \left(1 - \theta\right) \cdot g\left(F^n\right)\right], \tag{A.3}$$

where θ is a constant and $0 \leq \theta \leq 1$. The above equation becomes

$$F^{n+1} + \Delta t \cdot \theta \cdot g\left(F^{n+1}\right) = F^n - \Delta t \cdot \left(1 - \theta\right) \cdot g\left(F^n\right), \tag{A.4}$$

where $g\left(F\right) = \bigtriangledown \cdot \left(\overrightarrow{\lambda} \cdot F^2\right) + \bigtriangledown \cdot \left(H\left(F\right) \bigtriangledown \bigtriangledown^2\left(F + r\right)\right) - \bigtriangledown^2\left(H\left(F\right)\Pi\right)$. Its linearization is

$$g\left(F\right) = g\left(\widetilde{F}\right) + g_F\left(\widetilde{F}\right) v + \cdots\cdots, \tag{A.5}$$

where $g_F\left(\widetilde{F}\right)v$ is the functional derivative (see Oron & Bankoff (1999)), or the Jacobian of the function $g(F)$, i.e.

$$g_F(F)\,v = \triangledown\cdot\left(2\overrightarrow{\lambda}Fv\right)+\triangledown\cdot\left(H_F v\triangledown\triangledown^2(F+r)+H\triangledown\triangledown^2 v\right)-\triangledown^2\left(P_{DisjP,v}\right), \qquad \text{(A.6)}$$

where $P_{DisjP,v}=\left(H\left(F^{n+1}\right)\Pi\right)_F v$ and $v=F-\widetilde{F}$. $\widetilde{F}$ is the guess value in the linearization, which is updated in inner iterations till it is convergent to a criteria. The equation (A.4) finally becomes

$$v+\theta\cdot\Delta t\cdot g_F\left(\widetilde{F}^{n+1}\right)v=-\left(\widetilde{F}^{n+1}-F^n\right)-(1-\theta)\cdot\Delta t\cdot g\left(F^n\right)-\theta\cdot\Delta t\cdot g\left(\widetilde{F}^{n+1}\right), \qquad \text{(A.7)}$$

where

$$g(F)=\triangledown\cdot\left(\overrightarrow{\lambda}\cdot F^2\right)+\triangledown\cdot\left(H(F)\triangledown\triangledown^2(F+r)\right)-\triangledown^2\left(H(F)\Pi\right), \qquad \text{(A.8)}$$

and

$$g_F(F)\,v=\triangledown\cdot\left(2\overrightarrow{\lambda}Fv\right)+\triangledown\cdot\left(H_F v\triangledown\triangledown^2(F+r)+H\triangledown\triangledown^2 v\right)-\triangledown^2\left(P_{DisjP,F}v\right). \qquad \text{(A.9)}$$

To accelerate the calculation of the thin film equation, the pseudo-linear factorization method (see Witelski & Bowen (2003)) is applied in this study. Finally, the above difference equation (A.7) becomes

$$\widetilde{L}_x w=-\left(\widetilde{F}^{n+1}-F^n\right)-(1-\theta)\cdot\Delta t\cdot g\left(F^n\right)-\theta\cdot\Delta t\cdot g\left(\widetilde{F}^{n+1}\right), \qquad \text{(A.10)}$$

$$\widetilde{L}_z v=w, \qquad \text{(A.11)}$$

$$\widetilde{F}^{n+1}_{(k+1)}=\widetilde{F}^{n+1}_{(k)}+v, \qquad \text{(A.12)}$$

where

$$\widetilde{L}_x=I+\theta\cdot\Delta t\left(\widetilde{B}_x+\widetilde{D}_x+\widetilde{E}_x+\widetilde{G}_x\right), \qquad \text{(A.13)}$$

$$\widetilde{L}_z=I+\theta\cdot\Delta t\left(\widetilde{B}_z+\widetilde{D}_z+\widetilde{E}_z+\widetilde{G}_z\right), \qquad \text{(A.14)}$$

$$\widetilde{B}_x=\partial_x\left[2\lambda_x\widetilde{F}^{n+1}\right], \qquad \text{(A.15)}$$

$$\widetilde{B}_z=\partial_z\left[2\lambda_z\widetilde{F}^{n+1}\right], \qquad \text{(A.16)}$$

$$\widetilde{D}_x=\partial_x\left[H\left(\widetilde{F}^{n+1}\right)\partial_{xxx}\right], \qquad \text{(A.17)}$$

$$\widetilde{D}_z = \partial_z \left[H\left(\widetilde{F}^{n+1}\right) \partial_{zzz} \right], \tag{A.18}$$

$$\widetilde{E}_x = \partial_x \left[H_F \partial_{xxx} \left(\widetilde{F}^{n+1} + r\right) \right], \tag{A.19}$$

$$\widetilde{E}_z = \partial_z \left[H_F \partial_{zzz} \left(\widetilde{F}^{n+1} + r\right) \right], \tag{A.20}$$

$$\widetilde{G}_x = \partial_{xx}, \tag{A.21}$$

and

$$\widetilde{G}_z = \partial_{zz}. \tag{A.22}$$

A.2 Finite difference equations

1. x-direction

   Here is the summary of the finite difference equations in x-direction used in the simulations.

$$\begin{aligned} \widetilde{L}_x w &= \left[I + \theta \cdot \Delta t \left(\widetilde{B}_x + \widetilde{D}_x + \widetilde{E}_x + \widetilde{G}_x \right) \right] w \\ &= -\left(\widetilde{F}^{n+1} - F^n \right) - (1-\theta) \cdot \Delta t \cdot g\left(F^n\right) - \theta \cdot \Delta t \cdot g\left(\widetilde{F}^{n+1}\right), \end{aligned} \tag{A.23}$$

$$\begin{aligned} \widetilde{L}_x w &= \left[I + \theta \cdot \Delta t \left(\widetilde{B}_x + \widetilde{D}_x + \widetilde{E}_x + \widetilde{G}_x \right) \right] w \\ &= -\left(\widetilde{F}^{n+1} - F^n \right) - (1-\theta) \cdot \Delta t \cdot g\left(F^n\right) - \theta \cdot \Delta t \cdot g\left(\widetilde{F}^{n+1}\right), \end{aligned} \tag{A.24}$$

   where

$$\widetilde{B}_x = \partial_x \left[2\lambda_x \widetilde{F}^{n+1} \right], \tag{A.25}$$

$$\widetilde{D}_x = \partial_x \left[H\left(\widetilde{F}^{n+1}\right) \partial_{xxx} \right], \tag{A.26}$$

$$\widetilde{E}_x = \partial_x \left[H_F \partial_{xxx} \left(\widetilde{F}^{n+1} + r\right) \right], \tag{A.27}$$

   and

$$\widetilde{G}_x = \partial_{xx}. \tag{A.28}$$

   - Shear stress terms

$$term1 = Bw_{i-1,k} + Dw_{i+1,k} \tag{A.29}$$

where

$$B = -\frac{2\lambda_{xi-1,k} F_{i-1,k}}{2 \triangle x}, \tag{A.30}$$

$$D = -\frac{2\lambda_{xi+1,k} F_{i+1,k}}{2 \triangle x}. \tag{A.31}$$

- The highest order nonlinear terms with $F_w = F + r$

$$term2 = Aw_{i-2,k} + Bw_{i-1,k} + Cw_{i,k} + Dw_{i+1,k} + Ew_{i+2,k}, \tag{A.32}$$

where

$$A = \frac{1}{(\triangle x)^4} a_m, \tag{A.33}$$

$$B = \frac{1}{(\triangle x)^4} \left(-3a_m - a_p\right), \tag{A.34}$$

$$C = \frac{1}{(\triangle x)^4} \left(3a_m + 3a_p\right), \tag{A.35}$$

$$D = \frac{1}{(\triangle x)^4} \left(-a_m - 3a_p\right), \tag{A.36}$$

$$E = \frac{1}{(\triangle x)^4} a_p, \tag{A.37}$$

with

$$a_p = \begin{cases} \left(\widetilde{F}_{i,k}^{n+1}\right)^3, & \text{if } \widetilde{F}_{i,k}^{n+1} = \widetilde{F}_{i+1,k}^{n+1}; \\ \frac{2\left(\widetilde{F}_{i,k}^{n+1} \widetilde{F}_{i+1,k}^{n+1}\right)^2}{\widetilde{F}_{i,k}^{n+1} + \widetilde{F}_{i+1,k}^{n+1}}, & \text{otherwise,} \end{cases} \tag{A.38}$$

and

$$a_m = \begin{cases} \left(\widetilde{F}_{i,k}^{n+1}\right)^3, & \text{if } \widetilde{F}_{i,k}^{n+1} = \widetilde{F}_{i-1,k}^{n+1}; \\ \frac{2\left(\widetilde{F}_{i,k}^{n+1} \widetilde{F}_{i-1,k}^{n+1}\right)^2}{\widetilde{F}_{i,k}^{n+1} + \widetilde{F}_{i-1,k}^{n+1}}, & \text{otherwise.} \end{cases} \tag{A.39}$$

- Mixed derivatives

$$term31 = \frac{1}{(\triangle x)^4} a_p \left(F_{w,i+2,k} - 3F_{w,i+1,k} + 3F_{w,i,k} - F_{w,i-1,k}\right), \tag{A.40}$$

and

$$term32 = \frac{1}{(\triangle x)^4} a_m \left(F_{w,i-2,k} - 3F_{w,i-1,k} + 3F_{w,i,k} - F_{w,i+1,k}\right). \tag{A.41}$$

Then

$$term31 = Cw_{i,k} + Dw_{i+1,k}, \tag{A.42}$$

where

$$C = \begin{cases} \left(\widetilde{F}_{i,k}^{n+1}\right)^3 C_{4p}, & \text{if } \widetilde{F}_{i,k}^{n+1} = \widetilde{F}_{i+1,k}^{n+1}; \\ C_{3p}C_{4p}, & \text{otherwise,} \end{cases} \tag{A.43}$$

$$D = \begin{cases} 0, & \text{if } \widetilde{F}_{i,k}^{n+1} = \widetilde{F}_{i+1,k}^{n+1}; \\ C_{2p}C_{4p}, & \text{otherwise,} \end{cases} \tag{A.44}$$

and

$$C_{4p} = \left(F_{w,i+2,k} - 3F_{w,i+1,k} + 3F_{w,i,k} - F_{w,i-1,k}\right). \tag{A.45}$$

$$term32 = Bw_{i-1,k} + Cw_{i,k}, \tag{A.46}$$

with

$$B = \begin{cases} 0, & \text{if } \widetilde{F}_{i,k}^{n+1} = \widetilde{F}_{i-1,k}^{n+1}; \\ C_{3m}C_{4m}, & \text{otherwise,} \end{cases} \tag{A.47}$$

$$C = \begin{cases} \left(\widetilde{F}_{i,k}^{n+1}\right)^3 C_{4m}, & \text{if } \widetilde{F}_{i,k}^{n+1} = \widetilde{F}_{i-1,k}^{n+1}; \\ C_{2m}C_{4m}, & \text{otherwise,} \end{cases} \tag{A.48}$$

and

$$C_{4m} = \left(F_{w,i-2,k} - 3F_{w,i-1,k} + 3F_{w,i,k} - F_{w,i+1,k}\right). \tag{A.49}$$

In above equations, the functions $C_2\left(x, y\right)$and $C_3\left(x, y\right)$ are

$$C_2\left(x, y\right) = 2\frac{xy^2}{x+y}\left(2 - \frac{x}{x+y}\right) = C_3\left(y, x\right). \tag{A.50}$$

- Disjoining pressure terms

Here is an example as $m = 4$ and $n = 3$ for the classical disjoining pressure, i.e.

$$\Pi = B_m\left(\frac{\delta}{F}\right)^m - B_n\left(\frac{\delta}{F}\right)^n. \tag{A.51}$$

One difference equation of the disjoining pressure terms is

$$term4 = Bw_{i-1,k} + Cw_{i,k} + Dw_{i+1,k}, \tag{A.52}$$

where

$$B = \frac{B_{coeff,DisJP}}{(\triangle x)^2}\left(\frac{-4\delta^4}{F_{i-1,\,k}^2} + \frac{3\delta^3}{F_{i-1,\,k}}\right), \tag{A.53}$$

$$C = \frac{B_{coeff,DisJP}}{(\triangle x)^2}\left(\frac{-4\delta^4}{F_{i,\,k}^2} + \frac{3\delta^3}{F_{i,\,k}}\right), \tag{A.54}$$

$$D = \frac{B_{coeff,DisJP}}{(\triangle x)^2}\left(\frac{-4\delta^4}{F_{i+1,\,k}^2} + \frac{3\delta^3}{F_{i+1,\,k}}\right). \tag{A.55}$$

For the new disjoining pressure model with the inhomogeneous coefficients, there will be details later.

2. z-direction

$$\widetilde{L}_z v = \left[I + \theta \cdot \Delta t \left(\widetilde{B}_z + \widetilde{D}_z + \widetilde{E}_z + \widetilde{G}_z\right)\right] v = w, \tag{A.56}$$

where

$$\widetilde{B}_z = \partial_z \left[2\lambda_z \widetilde{F}^{n+1}\right], \tag{A.57}$$

$$\widetilde{D}_z = \partial_z \left[H\left(\widetilde{F}^{n+1}\right)\partial_{zzz}\right], \tag{A.58}$$

$$\widetilde{E}_z = \partial_z \left[H_F \partial_{zzz}\left(\widetilde{F}^{n+1} + r\right)\right], \tag{A.59}$$

$$\widetilde{G}_z = \partial_{zz}. \tag{A.60}$$

- Shear stress terms

The difference equation of the shear term is

$$term1 = Bw_{i,k-1} + Dw_{i,k+1}, \tag{A.61}$$

where

$$B = -\frac{2\lambda_{z,i,k-1}F_{i,k-1}}{2 \triangle z}, \tag{A.62}$$

$$D = -\frac{2\lambda_{z,i,k+1}F_{i,k+1}}{2 \triangle z}. \tag{A.63}$$

- The highest order nonlinear terms with $F_w = F + r$

  The difference equation of the highest order nonlinear term is

$$term2 = Aw_{i,k-2} + Bw_{i,k-1} + Cw_{i,k} + Dw_{i,k+1} + Ew_{i,k+2}, \tag{A.64}$$

where

$$A = \frac{1}{(\triangle z)^4} a_m, \tag{A.65}$$

$$B = \frac{1}{(\triangle z)^4} \left(-3a_m - a_p\right), \tag{A.66}$$

$$C = \frac{1}{(\triangle z)^4} \left(3a_m + 3a_p\right), \tag{A.67}$$

$$D = \frac{1}{(\triangle z)^4} \left(-a_m - 3a_p\right), \tag{A.68}$$

$$E = \frac{1}{(\triangle z)^4} a_p. \tag{A.69}$$

with

$$a_p = \begin{cases} \left(\widetilde{F}_{i,k}^{n+1}\right)^3, & \text{if } \widetilde{F}_{i,k}^{n+1} = \widetilde{F}_{i,k+1}^{n+1}; \\ \frac{2\left(\widetilde{F}_{i,k}^{n+1}\widetilde{F}_{i,k+1}^{n+1}\right)^2}{\widetilde{F}_{i,k}^{n+1}+\widetilde{F}_{i,k+1}^{n+1}}, & \text{otherwise,} \end{cases} \tag{A.70}$$

$$a_m = \begin{cases} \left(\widetilde{F}_{i,k}^{n+1}\right)^3, & \text{if } \widetilde{F}_{i,k}^{n+1} = \widetilde{F}_{i,k-1}^{n+1}; \\ \frac{2\left(\widetilde{F}_{i,k}^{n+1}\widetilde{F}_{i,k-1}^{n+1}\right)^2}{\widetilde{F}_{i,k}^{n+1}+\widetilde{F}_{i,k-1}^{n+1}}, & \text{otherwise.} \end{cases} \tag{A.71}$$

- Mixed derivatives The difference equation of the mixed derivatives is

$$term31 = \frac{1}{(\triangle z)^4} a_p \left(F_{w,i,k+2} - 3F_{w,i,k+1} + 3F_{w,i,k} - F_{w,i,k-1}\right), \tag{A.72}$$

and

$$term32 = \frac{1}{(\triangle z)^4} a_m \left(F_{w,i,k-2} - 3F_{w,i,k-1} + 3F_{w,i,k} - F_{w,i,k+1}\right). \tag{A.73}$$

After the simplification, they become

$$term31 = Cw_{i,k} + Dw_{i,k+1}, \tag{A.74}$$

where

$$C = \begin{cases} \left(\widetilde{F}_{i,k}^{n+1}\right)^3 C_{4p}, & \text{if } \widetilde{F}_{i,k}^{n+1} = \widetilde{F}_{i,k+1}^{n+1}; \\ C_{3p}C_{4p}, & \text{otherwise,} \end{cases} \tag{A.75}$$

$$D = \begin{cases} 0, & \text{if } \widetilde{F}_{i,k}^{n+1} = \widetilde{F}_{i,k+1}^{n+1}; \\ C_{2p}C_{4p}, & \text{otherwise.} \end{cases} \tag{A.76}$$

and

$$C_{4p} = \left(F_{w,i,k+2} - 3F_{w,i,k+1} + 3F_{w,i,k} - F_{w,i,k-1}\right). \tag{A.77}$$

$$term32 = Bw_{i,k-1} + Cw_{i,k}, \tag{A.78}$$

where

$$B = \begin{cases} 0, & \text{if } \widetilde{F}_{i,k}^{n+1} = \widetilde{F}_{i,k-1}^{n+1}; \\ C_{3m}C_{4m}, & \text{otherwise,} \end{cases} \tag{A.79}$$

$$C = \begin{cases} \left(\widetilde{F}_{i,k}^{n+1}\right)^3 C_{4m}, & \text{if } \widetilde{F}_{i,k}^{n+1} = \widetilde{F}_{i,k-1}^{n+1}; \\ C_{2m}C_{4m}, & \text{otherwise.} \end{cases} \tag{A.80}$$

and

$$C_{4m} = \left(F_{w,i,k-2} - 3F_{w,i,k-1} + 3F_{w,i,k} - F_{w,i,k+1}\right). \tag{A.81}$$

In above equations, the functions $C_2\left(x,y\right)$and $C_3\left(x,y\right)$ are

$$C_2\left(x,y\right) = 2\frac{xy^2}{x+y}\left(2 - \frac{x}{x+y}\right) = C_3\left(y,x\right), \tag{A.82}$$

- Disjoining pressure terms

Here is an example as $m = 4$ and $n = 3$ for the classical disjoining pressure.

$$term4 = Bw_{i-1,k} + Cw_{i,k} + Dw_{i+1,k}, \tag{A.83}$$

where

$$B = \frac{B_{coeff,DisJP}}{(\triangle z)^2} \left(\frac{-4\delta^4}{F_{i,\,k-1}^2} + \frac{3\delta^3}{F_{i,\,k-1}} \right), \tag{A.84}$$

$$C = \frac{B_{coeff,DisJP}}{(\triangle z)^2} \left(\frac{-4\delta^4}{F_{i,\,k}^2} + \frac{3\delta^3}{F_{i,\,k}} \right), \tag{A.85}$$

$$D = \frac{B_{coeff,DisJP}}{(\triangle z)^2} \left(\frac{-4\delta^4}{F_{i,\,k+1}^2} + \frac{3\delta^3}{F_{i,\,k+1}} \right). \tag{A.86}$$

For the new disjoining pressure model with the inhomogeneous coefficients, there will be details later.

APPENDIX B. The disjoining pressure term and its functional derivative

This method is used in the chapter 5, as well as for water films and beads motion near a stagnation line.

The new disjoining pressure model and the inhomogeneous coefficients are applied in the bead simulation. This is also the finite difference equations to solve the disjoining pressure terms in the one-dimensional thin film equation. The discussion below is the finite difference equation of one disjoining pressure term.

When the disjoining pressure model is applied to the thin film equation, the term with the disjoining pressure is

$$\frac{\partial}{\partial x}\left(F^3\frac{\partial \Pi}{\partial x}\right)=\frac{\partial}{\partial x}\left(F^3\frac{\partial}{\partial x}\left[BT\left(F\right)^m\right]\right)-\frac{\partial}{\partial x}\left(F^3\frac{\partial}{\partial x}\left[BT\left(F\right)^n\right]\right), \tag{B.1}$$

where $(m,n)=(3,2)$ and $k=2$ are used as an example, the new disjoining pressure model, i.e.

$$\Pi = B\left[T\left(F\right)^m - T\left(F\right)^n\right], \tag{B.2}$$

is used. The hyperbolic tangent function $T\left(F\right)$ is

$$T\left(F\right)=\tanh\left[\left(\frac{\delta}{F}\right)^k\right], \tag{B.3}$$

the inhomogeneous coefficient is

$$B = B_0 + \triangle B\left(U+W\right), \tag{B.4}$$

where

$$U\left(F\right)=\tanh\left[-FF_x\left(\frac{\delta}{F}\right)^k\right], \tag{B.5}$$

and

$$W\left(F\right)=\tanh\left[\left(F_x\right)^2\left(\frac{\delta}{F}\right)^k\right]. \tag{B.6}$$

B.1 Derivatives of the functions T , U and W

In the new disjoining pressure model with inhomogeneous coefficients, the derivatives of some terms are

1. The hyperbolic tangent function T

$$\frac{\partial}{\partial x}\left[T\left(F\right)^{m}\right]=m\left\{T\left(F\right)^{m-1}-T\left(F\right)^{m+1}\right\}\frac{\partial}{\partial x}\left[\left(\frac{\delta}{F}\right)^{k}\right] \tag{B.7}$$

2. The first derivative of the inhomogeneous function U

$$\frac{\partial}{\partial x}\left[U\left(F\right)\right]=A_1\left(A_2+A_3+A_4\right), \tag{B.8}$$

where

$$A_1=-\left(1-U^2\right), \tag{B.9a}$$

$$A_2=F\left[\left(\frac{\delta}{F}\right)^{k}\right]\frac{\partial^2 F}{\partial x^2}, \tag{B.9b}$$

$$A_3=F\frac{\partial}{\partial x}\left[\left(\frac{\delta}{F}\right)^{k}\right]\frac{\partial F}{\partial x}, \tag{B.9c}$$

$$A_4=\left(\frac{\partial F}{\partial x}\right)^{2}\left[\left(\frac{\delta}{F}\right)^{k}\right]. \tag{B.9d}$$

3. The second derivative of the inhomogeneous function U

$$\frac{\partial^2}{\partial x^2}\left[U\left(F\right)\right]=\frac{\partial A_1}{\partial x}\left(A_2+A_3+A_4\right)+A_1\left(\frac{\partial A_2}{\partial x}+\frac{\partial A_3}{\partial x}+\frac{\partial A_4}{\partial x}\right), \tag{B.10}$$

where

$$A_1=-\left(1-U^2\right), \tag{B.11a}$$

$$A_2=F\left[\left(\frac{\delta}{F}\right)^{k}\right]\frac{\partial^2 F}{\partial x^2}, \tag{B.11b}$$

$$A_3=F\frac{\partial}{\partial x}\left[\left(\frac{\delta}{F}\right)^{k}\right]\frac{\partial F}{\partial x}, \tag{B.11c}$$

$$A_4=\left(\frac{\partial F}{\partial x}\right)^{2}\left[\left(\frac{\delta}{F}\right)^{k}\right], \tag{B.11d}$$

and

$$\frac{\partial A_1}{\partial x} = 2U\frac{\partial U}{\partial x}, \tag{B.12a}$$

$$\frac{\partial A_2}{\partial x} = F\frac{\partial}{\partial x}\left[\left(\frac{\delta}{F}\right)^k\right]\frac{\partial^2 F}{\partial x^2} + F\left[\left(\frac{\delta}{F}\right)^k\right]\frac{\partial^3 F}{\partial x^3} + \frac{\partial F}{\partial x}\left[\left(\frac{\delta}{F}\right)^k\right]\frac{\partial^2 F}{\partial x^2}, \tag{B.12b}$$

$$\frac{\partial A_3}{\partial x} = F\frac{\partial^2}{\partial x^2}\left[\left(\frac{\delta}{F}\right)^k\right]\frac{\partial F}{\partial x} + F\frac{\partial}{\partial x}\left[\left(\frac{\delta}{F}\right)^k\right]\frac{\partial^2 F}{\partial x^2} + \frac{\partial}{\partial x}\left[\left(\frac{\delta}{F}\right)^k\right]\left(\frac{\partial F}{\partial x}\right)^2, \tag{B.12c}$$

$$\frac{\partial A_4}{\partial x} = 2\frac{\partial F}{\partial x}\frac{\partial^2 F}{\partial x^2}\left[\left(\frac{\delta}{F}\right)^k\right] + \left(\frac{\partial F}{\partial x}\right)^2\frac{\partial}{\partial x}\left[\left(\frac{\delta}{F}\right)^k\right]. \tag{B.12d}$$

4. The first derivative of the inhomogeneous function W

$$\frac{\partial}{\partial x}\left[W\left(F\right)\right] = \beta A_1\left(A_2 + A_3\right), \tag{B.13}$$

where

$$A_1 = \left(1 - W^2\right), \tag{B.14a}$$

$$A_2 = 2\left(\frac{\delta}{F}\right)^k\frac{\partial F}{\partial x}\frac{\partial^2 F}{\partial x^2}, \tag{B.14b}$$

$$A_3 = \left(\frac{\partial F}{\partial x}\right)^2\frac{\partial}{\partial x}\left[\left(\frac{\delta}{F}\right)^k\right]. \tag{B.14c}$$

5. The second derivative of the inhomogeneous function W

$$\frac{\partial^2}{\partial x^2}\left[W\left(F\right)\right] = \beta\left\{\frac{\partial A_1}{\partial x}\left(A_2 + A_3\right) + A_1\left(\frac{\partial A_2}{\partial x} + \frac{\partial A_3}{\partial x}\right)\right\}, \tag{B.15}$$

where

$$A_1 = \left(1 - W^2\right), \tag{B.16a}$$

$$A_2 = 2\left(\frac{\delta}{F}\right)^k\frac{\partial F}{\partial x}\frac{\partial^2 F}{\partial x^2}, \tag{B.16b}$$

$$A_3 = \left(\frac{\partial F}{\partial x}\right)^2\frac{\partial}{\partial x}\left[\left(\frac{\delta}{F}\right)^k\right], \tag{B.16c}$$

and

$$\frac{\partial A_1}{\partial x} = \frac{\partial}{\partial x}\left(1 - W^2\right) = -2W\frac{\partial W}{\partial x}, \tag{B.17}$$

$$\begin{aligned}\frac{\partial A_2}{\partial x} &= \frac{\partial}{\partial x}\left[2\left(\frac{\delta}{F}\right)^k \frac{\partial F}{\partial x}\frac{\partial^2 F}{\partial x^2}\right] \\ &= 2\frac{\partial}{\partial x}\left[\left(\frac{\delta}{F}\right)^k\right]\frac{\partial F}{\partial x}\frac{\partial^2 F}{\partial x^2} + 2\left(\frac{\delta}{F}\right)^k \frac{\partial^2 F}{\partial x^2}\frac{\partial^2 F}{\partial x^2} + 2\left(\frac{\delta}{F}\right)^k \frac{\partial F}{\partial x}\frac{\partial^3 F}{\partial x^3},\end{aligned} \tag{B.18}$$

$$\begin{aligned}\frac{\partial A_3}{\partial x} &= \frac{\partial}{\partial x}\left\{\left(\frac{\partial F}{\partial x}\right)^2 \frac{\partial}{\partial x}\left[\left(\frac{\delta}{F}\right)^k\right]\right\} \\ &= 2\frac{\partial F}{\partial x}\frac{\partial^2 F}{\partial x^2}\frac{\partial}{\partial x}\left[\left(\frac{\delta}{F}\right)^k\right] + \left(\frac{\partial F}{\partial x}\right)^2 \frac{\partial^2}{\partial x^2}\left[\left(\frac{\delta}{F}\right)^k\right].\end{aligned} \tag{B.19}$$

B.2 Finite difference equation of the terms with B

For simplicity, one component in equation (B.1), i.e. $\frac{\partial}{\partial x}\left(F^3\frac{\partial}{\partial x}\left[BT\left(F\right)^m\right]\right)$ is used to illustrate the numerical scheme:

$$\frac{\partial}{\partial x}\left(F^3\frac{\partial}{\partial x}\left[BT\left(F\right)^m\right]\right) = \left(term11 + term11\right) + \left(-2m\delta^2\right)\cdot\left(term21 + term22\right), \tag{B.20}$$

where

$$term11 = \frac{\partial}{\partial x}\left(T\left(F\right)^m F^3\right)\frac{\partial B}{\partial x}, \tag{B.21a}$$

$$term12 = T\left(F\right)^m F^3\frac{\partial^2 B}{\partial x^2}, \tag{B.21b}$$

$$term21 = \left[T\left(F\right)^{m-1} - T\left(F\right)^{m+1}\right]\frac{\partial B}{\partial x}\frac{\partial F}{\partial x}, \tag{B.21c}$$

$$term22 = B\left[T\left(F\right)^{m-1} - T\left(F\right)^{m+1}\right]\frac{\partial^2 F}{\partial x^2}. \tag{B.21d}$$

1. Functional derivatives of term 1 The functional derivative of the term 1 is

$$\left\langle term1\right\rangle_F v = \frac{\partial}{\partial x}\left\langle\left(T\left(F\right)^m F^3\frac{\partial B}{\partial x}\right)\right\rangle_F v. \tag{B.22}$$

   It is written as

$$\left\langle term1\right\rangle_F v = part1 + part2 + part3, \tag{B.23}$$

where

$$part1 = \frac{\partial}{\partial x}\left(\langle T(F)^m\rangle_F vF^3\frac{\partial B}{\partial x}\right), \tag{B.24a}$$

$$part2 = \frac{\partial}{\partial x}\left(T(F)^m\left\langle F^3\right\rangle_F v\frac{\partial B}{\partial x}\right) + \frac{\partial}{\partial x}\left(T(F)^m F^3\frac{\partial}{\partial x}\langle B\rangle_F v\right), \tag{B.24b}$$

$$part3 = \frac{\partial}{\partial x}\left(T(F)^m F^3\frac{\partial}{\partial x}\langle B\rangle_F v\right). \tag{B.24c}$$

- Difference equations of part 1

$$part1 = \frac{\partial}{\partial x}\left(\langle T(F)^m\rangle_F vF^3\frac{\partial B}{\partial x}\right) = \frac{\partial}{\partial x}(Av) = A\frac{\partial v}{\partial x} + \frac{\partial A}{\partial x}v, \tag{B.25}$$

where

$$A = -2m\delta^2\left[T(F)^{m-1} - T(F)^{m+1}\right]\frac{\partial B}{\partial x}. \tag{B.26}$$

Its difference equation is

$$part1 = av_{i-2} + bv_{i-1} + cv_i + dv_{i+1} + ev_{i+2}, \tag{B.27}$$

where

$$a = \frac{1}{12\triangle x}A + 0, \tag{B.28a}$$

$$b = -\frac{1}{12\triangle x}8A + 0, \tag{B.28b}$$

$$c = 0 + \frac{\partial A}{\partial x}, \tag{B.28c}$$

$$d = \frac{1}{12\triangle x}8A + 0, \tag{B.28d}$$

$$e = -\frac{1}{12\triangle x}A + 0, \tag{B.28e}$$

and

$$A = -2m\delta^2\left[T(F)^{m-1} - T(F)^{m+1}\right]\frac{\partial B}{\partial x}. \tag{B.29}$$

- Difference equations of part 2

$$part2 = \frac{\partial}{\partial x}\left(T\left(F\right)^{m}\left\langle F^{3}\right\rangle_{F} v\frac{\partial B}{\partial x}\right) = A\frac{\partial v}{\partial x} + \frac{\partial A}{\partial x}v, \tag{B.30}$$

where

$$A = T\left(F\right)^{m} 3F^{2}\frac{\partial B}{\partial x}. \tag{B.31}$$

The difference equation is

$$part2 = av_{i-2} + bv_{i-1} + cv_{i} + dv_{i+1} + ev_{i+2}, \tag{B.32}$$

where

$$a = \frac{1}{12 \bigtriangleup x}A + 0, \tag{B.33a}$$

$$b = -\frac{1}{12 \bigtriangleup x}8A + 0, \tag{B.33b}$$

$$c = 0 + \frac{\partial A}{\partial x}, \tag{B.33c}$$

$$d = \frac{1}{12 \bigtriangleup x}8A + 0, \tag{B.33d}$$

$$e = -\frac{1}{12 \bigtriangleup x}A + 0, \tag{B.33e}$$

and

$$A = 3T\left(F\right)^{m} F^{2}\frac{\partial B}{\partial x}. \tag{B.34}$$

2. Functional derivatives of term 2

The term2 is

$$term2 = \frac{\partial}{\partial x}\left\{B\left[T\left(F\right)^{m-1} - T\left(F\right)^{m+1}\right]\frac{\partial F}{\partial x}\right\}. \tag{B.35}$$

The differential equation is

$$\begin{aligned}\left\langle term2\right\rangle_{F} v &= \left\langle \frac{\partial}{\partial x}\left\{B\left[T\left(F\right)^{m-1} - T\left(F\right)^{m+1}\right]\frac{\partial F}{\partial x}\right\}\right\rangle_{F} v \\ &= part1 + part2 + part3,\end{aligned} \tag{B.36}$$

where

$$part1 = \frac{\partial}{\partial x}\left\{B\left[T\left(F\right)^{m-1} - T\left(F\right)^{m+1}\right]\left\langle\frac{\partial F}{\partial x}\right\rangle_F v\right\}, \tag{B.37a}$$

$$part2 = \frac{\partial}{\partial x}\left\{B\left\langle\left[T\left(F\right)^{m-1} - T\left(F\right)^{m+1}\right]\right\rangle_F v\frac{\partial F}{\partial x}\right\}, \tag{B.37b}$$

$$part3 = \frac{\partial}{\partial x}\left\{\left\langle B\right\rangle_F v\left[T\left(F\right)^{m-1} - T\left(F\right)^{m+1}\right]\frac{\partial F}{\partial x}\right\}. \tag{B.37c}$$

The difference equation of each component in the term2, i.e. $part1$, $part2$ and $part3$ is written as following text.

- part 1

$$part1 = av_{i-2} + bv_{i-1} + cv_i + dv_{i+1} + ev_{i+2}, \tag{B.38}$$

where

$$a = -\frac{1}{12\left(\triangle x\right)^2}A + \frac{1}{12\triangle x}\frac{\partial A}{\partial x}, \tag{B.39a}$$

$$b = \frac{1}{12\left(\triangle x\right)^2}16A - \frac{1}{12\triangle x}8\frac{\partial A}{\partial x}, \tag{B.39b}$$

$$c = -\frac{1}{12\left(\triangle x\right)^2}30A + 0, \tag{B.39c}$$

$$d = \frac{1}{12\left(\triangle x\right)^2}16A + \frac{1}{12\triangle x}8\frac{\partial A}{\partial x}, \tag{B.39d}$$

$$e = -\frac{1}{12\left(\triangle x\right)^2}A - \frac{1}{12\triangle x}\frac{\partial A}{\partial x}, \tag{B.39e}$$

and

$$A = B\left[T\left(F\right)^{m-1} - T\left(F\right)^{m+1}\right]. \tag{B.40}$$

- part 2

$$\begin{aligned} part2 &= \frac{\partial}{\partial x}\left\{B\left\langle\left[T\left(F\right)^{m-1} - T\left(F\right)^{m+1}\right]\right\rangle_F v\frac{\partial F}{\partial x}\right\} \\ &= A\frac{\partial v}{\partial x} + \frac{\partial A}{\partial x}v, \end{aligned} \tag{B.41}$$

where

$$A = B \cdot C \cdot D, \tag{B.42}$$

$$C = \frac{\partial}{\partial x}\left[\left(\frac{\delta}{F}\right)^k\right], \tag{B.43}$$

$$D = \left\{(m-1)\left[T(F)^{m-2} - T(F)^m\right] - (m+1)\left[T(F)^m - T(F)^{m+2}\right]\right\}. \tag{B.44}$$

Its difference equation is

$$part2 = av_{i-2} + bv_{i-1} + cv_i + dv_{i+1} + ev_{i+2}, \tag{B.45}$$

where

$$a = \frac{1}{12 \triangle x}A + 0, \tag{B.46a}$$

$$b = -\frac{1}{12 \triangle x}8A + 0, \tag{B.46b}$$

$$c = 0 + \frac{\partial A}{\partial x}, \tag{B.46c}$$

$$d = \frac{1}{12 \triangle x}8A + 0, \tag{B.46d}$$

$$e = -\frac{1}{12 \triangle x}A + 0, \tag{B.46e}$$

and

$$A = B \cdot C \cdot D, \tag{B.47}$$

$$C = \frac{\partial}{\partial x}\left[\left(\frac{\delta}{F}\right)^k\right], \tag{B.48}$$

$$D = \left\{(m-1)\left[T(F)^{m-2} - T(F)^m\right] - (m+1)\left[T(F)^m - T(F)^{m+2}\right]\right\}. \tag{B.49}$$

B.3 Finite difference equation of the terms with U

1. Term 1

$$\begin{aligned} term1 &= \frac{\partial}{\partial x}\left(T(F)^m F^3 \frac{\partial}{\partial x}\langle B_0\rangle_F v\right) \\ &= \triangle B \cdot \frac{\partial}{\partial x}\left\{T(F)^m F^3\left[\frac{\partial}{\partial x}\langle U(F)\rangle_F v + \frac{\partial}{\partial x}\langle W(F)\rangle_F v\right]\right\} \end{aligned} \tag{B.50}$$

The term of U is

$$\begin{aligned} part1 &= \triangle B \cdot \frac{\partial}{\partial x}\left\{T\left(F\right)^{m}F^{3}\left[\frac{\partial}{\partial x}\left\langle U\left(F\right)\right\rangle_{F}v\right]\right\} \\ &= \beta\left(part11 + part12\right), \end{aligned} \tag{B.51}$$

where

$$part11 = \frac{\partial}{\partial x}\left\{T\left(F\right)^{m}F^{3}\frac{\partial}{\partial x}\left\langle -\left(1-U^{2}\right)F\frac{\partial}{\partial x}\left[\left(\frac{\delta}{F}\right)^{k}v\right]\right\rangle\right\}, \tag{B.52}$$

$$part12 = \frac{\partial}{\partial x}\left\{T\left(F\right)^{m}F^{3}\frac{\partial}{\partial x}\left\langle -\left(1-U^{2}\right)\frac{\partial F}{\partial x}\left[\left(\frac{\delta}{F}\right)^{k}v\right]\right\rangle\right\}. \tag{B.53}$$

- part11

$$part11 = av_{i-2} + bv_{i-1} + cv_{i} + dv_{i+1} + ev_{i+2}, \tag{B.54}$$

where

$$a = \frac{1}{12\triangle x}C_{i-2}A1 - \frac{1}{12\left(\triangle x\right)^{2}}C_{i-2}A2 - \frac{1}{2\left(\triangle x\right)^{3}}C_{i-2}A3, \tag{B.55a}$$

$$b = -\frac{1}{12\triangle x}8C_{i-1}A1 + \frac{1}{12\left(\triangle x\right)^{2}}16C_{i-1}A2 + \frac{1}{2\left(\triangle x\right)^{3}}2C_{i-1}A3, \tag{B.55b}$$

$$c = -\frac{1}{12\left(\triangle x\right)^{2}}30C_{i}A2, \tag{B.55c}$$

$$d = \frac{1}{12\triangle x}8C_{i+1}A1 + \frac{1}{12\left(\triangle x\right)^{2}}16C_{i+1}A2 - \frac{1}{2\left(\triangle x\right)^{3}}2C_{i+1}A3, \tag{B.55d}$$

$$e = -\frac{1}{12\triangle x}C_{i+2}A1 - \frac{1}{12\left(\triangle x\right)^{2}}C_{i+2}A2 + \frac{1}{2\left(\triangle x\right)^{3}}C_{i+2}A3, \tag{B.55e}$$

and

$$A1 = \frac{\partial}{\partial x}\left(A\frac{\partial D}{\partial x}\right), \tag{B.56a}$$

$$A2 = A\frac{\partial D}{\partial x} + \frac{\partial}{\partial x}\left(AD\right), \tag{B.56b}$$

$$A3 = AD, \tag{B.56c}$$

$$A = T\left(F\right)^{m}F^{3}, \tag{B.56d}$$

$$D = -\left(1-U^{2}\right)F, \tag{B.56e}$$

$$C = \left(\frac{\delta}{F}\right)^{k}. \tag{B.56f}$$

- part12

$$part12 = av_{i-2} + bv_{i-1} + cv_i + dv_{i+1} + ev_{i+2}, \tag{B.57}$$

where

$$a = -\frac{1}{12\left(\triangle x\right)^2} C_{i-2} A1 + \frac{1}{12 \triangle x} C_{i-2} A2 + 0, \tag{B.58a}$$

$$b = \frac{1}{12\left(\triangle x\right)^2} 16 C_{i-1} A1 - \frac{1}{12 \triangle x} 8 C_{i-1} A2 + 0, \tag{B.58b}$$

$$c = -\frac{1}{12\left(\triangle x\right)^2} 30 C_i A1 + 0 + C_i A3, \tag{B.58c}$$

$$d = \frac{1}{12\left(\triangle x\right)^2} 16 C_{i+1} A1 + \frac{1}{12 \triangle x} 8 C_{i+1} A2 + 0, \tag{B.58d}$$

$$e = -\frac{1}{12\left(\triangle x\right)^2} C_{i+2} A1 - \frac{1}{12 \triangle x} C_{i+2} A2 + 0, \tag{B.58e}$$

and

$$A1 = AD, \tag{B.59a}$$

$$A2 = \frac{\partial}{\partial x}\left(AD\right) + A\frac{\partial D}{\partial x}, \tag{B.59b}$$

$$A3 = \frac{\partial}{\partial x}\left\{A\frac{\partial D}{\partial x}\right\}, \tag{B.59c}$$

with

$$A = T\left(F\right)^m F^3, \tag{B.60a}$$

$$D = -\left(1 - U^2\right)\frac{\partial F}{\partial x}, \tag{B.60b}$$

$$C = \left(\frac{\delta}{F}\right)^k. \tag{B.60c}$$

2. term 2

   The term2 is

$$term2 = \frac{\partial}{\partial x}\left\{B\left[T\left(F\right)^{m-1} - T\left(F\right)^{m+1}\right]\frac{\partial F}{\partial x}\right\}, \tag{B.61}$$

Its functional derivative is

$$\begin{aligned}\langle term2\rangle_F v = {} & \frac{\partial}{\partial x}\left\{\langle B\rangle_F v\left[T(F)^{m-1}-T(F)^{m+1}\right]\frac{\partial F}{\partial x}\right\}\\ & + \frac{\partial}{\partial x}\left\{B\left\langle\left[T(F)^{m-1}-T(F)^{m+1}\right]\right\rangle_F v\frac{\partial F}{\partial x}\right\}\\ & + \frac{\partial}{\partial x}\left\{B\left[T(F)^{m-1}-T(F)^{m+1}\right]\left\langle\frac{\partial F}{\partial x}\right\rangle_F v\right\}.\end{aligned} \tag{B.62}$$

The terms having U are

$$\begin{aligned} part1 &= \frac{\partial}{\partial x}\left\{\langle U(F)\rangle_F v\left[T(F)^{m-1}-T(F)^{m+1}\right]\frac{\partial F}{\partial x}\right\}\\ &= \beta\left(part11+part12\right),\end{aligned} \tag{B.63}$$

where

$$part11 = \frac{\partial}{\partial x}\left\{-\left(1-U^2\right)\left[T(F)^{m-1}-T(F)^{m+1}\right]F\frac{\partial F}{\partial x}\frac{\partial}{\partial x}\left[\left(\frac{\delta}{F}\right)^k v\right]\right\}, \tag{B.64}$$

$$part12 = \frac{\partial}{\partial x}\left\{-\left(1-U^2\right)\left[T(F)^{m-1}-T(F)^{m+1}\right]\frac{\partial F}{\partial x}\frac{\partial F}{\partial x}\left[\left(\frac{\delta}{F}\right)^k v\right]\right\}. \tag{B.65}$$

- part11

  The finite difference equation of the term part11 is

$$part11 = av_{i-2}+bv_{i-1}+cv_i+dv_{i+1}+ev_{i+2}, \tag{B.66}$$

  where

$$a = \frac{1}{12\triangle x}C_{i-2}\frac{\partial D}{\partial x}-\frac{1}{12\left(\triangle x\right)^2}C_{i-2}D, \tag{B.67a}$$

$$b = -\frac{1}{12\triangle x}8C_{i-1}\frac{\partial D}{\partial x}+\frac{1}{12\left(\triangle x\right)^2}16C_{i-1}D, \tag{B.67b}$$

$$c = 0-\frac{1}{12\left(\triangle x\right)^2}30C_iD, \tag{B.67c}$$

$$d = \frac{1}{12\triangle x}8C_{i+1}\frac{\partial D}{\partial x}+\frac{1}{12\left(\triangle x\right)^2}16C_{i+1}D, \tag{B.67d}$$

$$e = -\frac{1}{12\triangle x}C_{i+2}\frac{\partial D}{\partial x}-\frac{1}{12\left(\triangle x\right)^2}C_{i+2}D, \tag{B.67e}$$

and

$$D = -\left(1-U^2\right)\left[T\left(F\right)^{m-1} - T\left(F\right)^{m+1}\right]\frac{\partial F}{\partial x}F, \tag{B.68a}$$

$$C = \left(\frac{\delta}{F}\right)^k. \tag{B.68b}$$

- part12

The finite difference equation of the term part12 is

$$part12 = av_{i-2} + bv_{i-1} + cv_i + dv_{i+1} + ev_{i+2}, \tag{B.69}$$

where

$$a = \frac{1}{12 \bigtriangleup x}C_{i-2}D + 0, \tag{B.70a}$$

$$b = -\frac{1}{12 \bigtriangleup x}8C_{i-1}D + 0, \tag{B.70b}$$

$$c = 0 + C_i\frac{\partial D}{\partial x}, \tag{B.70c}$$

$$d = \frac{1}{12 \bigtriangleup x}8C_{i+1}D + 0, \tag{B.70d}$$

$$e = -\frac{1}{12 \bigtriangleup x}C_{i+2}D + 0, \tag{B.70e}$$

with

$$D = -\left(1-U^2\right)\left[T\left(F\right)^{m-1} - T\left(F\right)^{m+1}\right]\left(\frac{\partial F}{\partial x}\right)^2, \tag{B.71a}$$

$$C = \left(\frac{\delta}{F}\right)^k. \tag{B.71b}$$

B.4 Finite difference equation of the terms with W

1. Term 1

$$term1 = \triangle B \cdot \frac{\partial}{\partial x}\left\{T\left(F\right)^m F^3\left[\frac{\partial}{\partial x}\left\langle W\left(F\right)\right\rangle_F v\right]\right\}, \tag{B.72}$$

where

$$\left\langle W\left(F\right)\right\rangle_F v = \beta\left(1-W^2\right)\frac{\partial F}{\partial x}\left\{2\frac{\partial}{\partial x}\left[\left(\frac{\delta}{F}\right)^k v\right] - \frac{\partial}{\partial x}\left[\left(\frac{\delta}{F}\right)^k\right]v\right\}. \tag{B.73}$$

The above equation can be written as

$$\begin{aligned} part2 &= \triangle B \cdot \frac{\partial}{\partial x}\left\{T\left(F\right)^{m} F^{3}\left[\frac{\partial}{\partial x}\left\langle W\left(F\right)\right\rangle_{F} v\right]\right\} \\ &= \beta\left(part21 + part22\right), \end{aligned} \tag{B.74}$$

where

$$part21 = \frac{\partial}{\partial x}\left\langle T\left(F\right)^{m} F^{3} \frac{\partial}{\partial x}\left\{2\left(1-W^{2}\right)\frac{\partial F}{\partial x}\frac{\partial}{\partial x}\left[\left(\frac{\delta}{F}\right)^{k} v\right]\right\}\right\rangle, \tag{B.75a}$$

$$part22 = \frac{\partial}{\partial x}\left\{T\left(F\right)^{m} F^{3} \frac{\partial}{\partial x}\left\{-\left(1-W^{2}\right)\frac{\partial F}{\partial x}\frac{\partial}{\partial x}\left[\left(\frac{\delta}{F}\right)^{k}\right] v\right\}\right\}. \tag{B.75b}$$

- part21

  The finite difference equation of the part21 is

$$part21 = av_{i-2} + bv_{i-1} + cv_{i} + dv_{i+1} + ev_{i+2}, \tag{B.76}$$

where

$$a = -\frac{1}{2\left(\triangle x\right)^{3}}C_{i-2}A1 - \frac{1}{12\left(\triangle x\right)^{2}}C_{i-2}A2 + \frac{1}{12\triangle x}C_{i-2}A3, \tag{B.77a}$$

$$b = \frac{1}{2\left(\triangle x\right)^{3}}2C_{i-1}A1 + \frac{1}{12\left(\triangle x\right)^{2}}16C_{i-1}A2 - \frac{1}{12\triangle x}8C_{i-1}A3, \tag{B.77b}$$

$$c = 0 - \frac{1}{12\left(\triangle x\right)^{2}}30C_{i}A2 + 0, \tag{B.77c}$$

$$d = -\frac{1}{2\left(\triangle x\right)^{3}}2C_{i+1}A1 + \frac{1}{12\left(\triangle x\right)^{2}}16C_{i+1}A2 + \frac{1}{12\triangle x}8C_{i+1}A3, \tag{B.77d}$$

$$e = \frac{1}{2\left(\triangle x\right)^{3}}C_{i+2}A1 - \frac{1}{12\left(\triangle x\right)^{2}}C_{i+2}A2 - \frac{1}{12\triangle x}C_{i+2}A3, \tag{B.77e}$$

and

$$A1 = AD, \tag{B.78a}$$

$$A2 = A\frac{\partial D}{\partial x} + \frac{\partial}{\partial x}\left(AD\right), \tag{B.78b}$$

$$A3 = \frac{\partial}{\partial x}\left\{A\frac{\partial D}{\partial x}\right\}, \tag{B.78c}$$

and

$$A = T(F)^m F^3, \tag{B.79a}$$

$$D = 2\left(1 - W^2\right)\frac{\partial F}{\partial x}, \tag{B.79b}$$

$$C = \left(\frac{\delta}{F}\right)^k. \tag{B.79c}$$

- part22

For the part22, the finite difference equation is

$$part22 = av_{i-2} + bv_{i-1} + cv_i + dv_{i+1} + ev_{i+2}, \tag{B.80}$$

where

$$a = -\frac{1}{12(\triangle x)^2}AD + \frac{1}{12\triangle x}\left\{A\frac{\partial D}{\partial x} + \frac{\partial}{\partial x}(AD)\right\} + 0, \tag{B.81a}$$

$$b = \frac{1}{12(\triangle x)^2}16AD - \frac{1}{12\triangle x}8\left\{A\frac{\partial D}{\partial x} + \frac{\partial}{\partial x}(AD)\right\} + 0, \tag{B.81b}$$

$$c = -\frac{1}{12(\triangle x)^2}30AD + 0 + \frac{\partial}{\partial x}\left\{A\frac{\partial D}{\partial x}\right\}, \tag{B.81c}$$

$$d = \frac{1}{12(\triangle x)^2}16AD + \frac{1}{12\triangle x}8\left\{A\frac{\partial D}{\partial x} + \frac{\partial}{\partial x}(AD)\right\} + 0, \tag{B.81d}$$

$$e = -\frac{1}{12(\triangle x)^2}AD - \frac{1}{12\triangle x}\left\{A\frac{\partial D}{\partial x} + \frac{\partial}{\partial x}(AD)\right\} + 0, \tag{B.81e}$$

and

$$A = T(F)^m F^3, \tag{B.82a}$$

$$D = -\left(1 - W^2\right)\frac{\partial F}{\partial x}\frac{\partial}{\partial x}\left[\left(\frac{\delta}{F}\right)^k\right]. \tag{B.82b}$$

2. Term 2

In the term 2, the part 2 is

$$part2 = \frac{\partial}{\partial x}\left\{\langle W(F)\rangle_F v\left[T(F)^{m-1} - T(F)^{m+1}\right]\frac{\partial F}{\partial x}\right\}, \tag{B.83}$$

with

$$\langle W(F)\rangle_F v = \beta\left(1-W^2\right)\frac{\partial F}{\partial x}\left\{2\frac{\partial}{\partial x}\left[\left(\frac{\delta}{F}\right)^k v\right]-\frac{\partial}{\partial x}\left[\left(\frac{\delta}{F}\right)^k\right]v\right\}. \tag{B.84}$$

Then part2 becomes

$$part2 = \beta\left(part21 + part22\right), \tag{B.85}$$

where

$$part21 = \frac{\partial}{\partial x}\left\{2\left(1-W^2\right)\left[T(F)^{m-1}-T(F)^{m+1}\right]\left(\frac{\partial F}{\partial x}\right)^2\frac{\partial}{\partial x}\left[\left(\frac{\delta}{F}\right)^k v\right]\right\}, \tag{B.86a}$$

$$part22 = \frac{\partial}{\partial x}\left\{-\left(1-W^2\right)\left[T(F)^{m-1}-T(F)^{m+1}\right]\left(\frac{\partial F}{\partial x}\right)^2\frac{\partial}{\partial x}\left[\left(\frac{\delta}{F}\right)^k\right]v\right\}. \tag{B.86b}$$

- part21 Finally, the finite difference equations are

$$part21 = av_{i-2} + bv_{i-1} + cv_i + dv_{i+1} + ev_{i+2}, \tag{B.87}$$

where

$$a = -\frac{1}{12\left(\triangle x\right)^2}C_{i-2}D + \frac{1}{12\triangle x}C_{i-2}\frac{\partial D}{\partial x}, \tag{B.88a}$$

$$b = \frac{1}{12\left(\triangle x\right)^2}16C_{i-1}D - \frac{1}{12\triangle x}8C_{i-1}\frac{\partial D}{\partial x}, \tag{B.88b}$$

$$c = -\frac{1}{12\left(\triangle x\right)^2}30C_iD + 0, \tag{B.88c}$$

$$d = \frac{1}{12\left(\triangle x\right)^2}16C_{i+1}D + \frac{1}{12\triangle x}8C_{i+1}\frac{\partial D}{\partial x}, \tag{B.88d}$$

$$e = -\frac{1}{12\left(\triangle x\right)^2}C_{i+2}D - \frac{1}{12\triangle x}C_{i+2}\frac{\partial D}{\partial x}, \tag{B.88e}$$

and

$$C = \left(\frac{\delta}{F}\right)^k, \tag{B.89a}$$

$$D = 2\left(1-W^2\right)\left[T(F)^{m-1}-T(F)^{m+1}\right]\left(\frac{\partial F}{\partial x}\right)^2. \tag{B.89b}$$

- part22

$$part22 = av_{i-2} + bv_{i-1} + cv_i + dv_{i+1} + ev_{i+2}, \tag{B.90}$$

where

$$a = \frac{1}{12 \bigtriangleup x} D + 0, \tag{B.91a}$$

$$b = -\frac{1}{12 \bigtriangleup x} 8D + 0, \tag{B.91b}$$

$$c = 0 + \frac{\partial D}{\partial x}, \tag{B.91c}$$

$$d = \frac{1}{12 \bigtriangleup x} 8D + 0, \tag{B.91d}$$

$$e = -\frac{1}{12 \bigtriangleup x} D + 0, \tag{B.91e}$$

and

$$D = -\left(1 - W^2\right) \left[T\left(F\right)^{m-1} - T\left(F\right)^{m+1}\right] \left(\frac{\partial F}{\partial x}\right)^2 \frac{\partial}{\partial x} \left[\left(\frac{\delta}{F}\right)^k\right]. \tag{B.92}$$

BIBLIOGRAPHY

[1] Achenbach, E. (1977). The effect of surface roughness on the heat transfer from a circular cylinder to the cross flow of air. *International Journal of Heat and Mass Transfer*, *20*, 359–369.

[2] Abramowitz, M. & Stegun, I. A. (Eds.) (1972). *Handbook of Mathematical Functions with Formulas, Graphs, and Mathematical Tables.* 9th printing, New York: Dover.

[3] Akylas, T. R. (1982). A nonlinear theory for the generation of water waves by wind. *Studies in Applied Mathematics*, *67*, 1–24.

[4] Atlanta: ASHRAE (2001). *Handbook of fundamentals.* American Society of Heating, Refrigeration, and Air-Conditioning Engineers, Inc.

[5] Babak, V. G. (1992). Line tension in the thermodynamics of thin liquid films. *Russian Chemical Review* translated from *Uspekhi Khimii*, *61*(10), 975–989.

[7] Babak, V. G. (1998). Thermodynamics of plane-parallel liquid films, *Colloids and Surfaces A*, *142*, 135–153.

[7] Babak, V. G. (1999). Generalised line tension theory revisited, *Colloids and Surfaces A*, *156*, 423–448.

[8] Bauer, S. & Dietrich, S. (1999). Wetting films on chemically heterogeneous substrates. *Physical Review E*, *60*, 6919–6941.

[9] Belcher, S. E., Harris, J. A. & Street, R. L. (1994). Linear dynamics of wind waves in coupled turbulent air-water flow. Part 1. Theory. *Journal of Fluid Mechanics*, *271*, 119–151.

[10] Bernis, F. & Friedman, A. (1974). Higher order nonlinear degenerate parabolic equations. *Journal of differential equations*, *83*, 71–95.

[11] Bertozzi, A. L. & Pugh, M. (1996). The lubrication approximation for the viscous films: regularity and long time behavior of weak solution. *Communications on pure and applied mathematics*, *29*, 321–342.

[12] Bilanin, A. J. & Anderson, D. N. (1995). Ice accretion with varying surface tension. *AIAA paper 95-0538*, presented at the 33rd Aerospace Sciences Meeting, Reno NV.

[13] Bertozzi A. L. & Brenner, M. P. (1997). Linear stability and transient growth in driven contact lines. *Physics of Fluids*, *9*(3), 530–539.

[14] Blennerhassett, P. J. & Smith, F. T. (1987). Short-scale waves on wind-driven water ('cat's paws'). *Proceedings of the Royal Society of London*, *A410*, 1–17.

[15] Bogolepov V. V. & Neiland, V. Ya. (1971). Viscous gas motion near small irregularities on a rigid body surface in supersonic flow. *Trudy TsAGI*, *1363.*

[16] Bogolepov V. V. & Neiland, V. Ya. (1976). Investigation of local perturbations in viscous supersonic flows. *Aeromechanics, Collected articles, Moscow Science* 104–118. (in Russian *Aeromekhanika. Sb. statej. Moskva. Nauka.* 1976. ss. 104–118). translated in *Soviet Research-Fluid Mechanics Soviet Research/Scripta Technica*, USA, 1980 *2*, 84–95.

[17] Borgas, M. S. & Grotberg, J. B. (1988). Monolayer flow on a thin film. *Journal of Fluid Mechanics*, *193*, 151–170.

[18] Bourgault, Y., Beaugendre, H. & Habashi, W.G. (2000). Development of a shallow water icing model in FENSAP-ICE. *Journal of Aircraft*, *37*(4), 640–646.

[19] Bourgault, Y., Habashi, W. G. & Beaugendre, H. (1999). Development of a shallow water icing model in FENSAP-ICE. *AIAA paper 99-0246*, presented at the 37th Aerospace Sciences Meeting, Reno NV.

[20] Boruvka, L. & Neumann, A. W. (1977). Generalization of the classical theory of capillarity. *The Journal of Chemical Physics*, *66*(12), 5464–5476.

[21] Brenner, M. P. (1993). Instability mechanism at driven contact lines. *Physiccal Review E*, *47*(6), 4597–4599.

[22] Brzoska, J. B., Brochard-Wyart, F. & Rondelez, F. (1992). Exponential growth of fingering instabilities of spreading films under horizontal thermal gradients. *Europhysics Letters*, *19*(2), 97–102.

[23] Burelbach, J. P., Bankoff, S. G. & Davis, S. H. (1988). Nonlinear stability of evaporating/condensing liquid films. *Journal of Fluid Mechanics*, *195*, 463–494.

[24] Canuto, C., Hussaini, M. Y., Quarteroni, A. & Zang T. A. (1988). *Spectral methods in fluid dynamics*. Berlin: Springer Series in Computational Physics.

[25] Cazabat, A. M., Heslot, F., Carles P. & Troian, S. M. (1992). Hydrodynamic fingering instability of driven wetting films. *Advances in Colloid and Interface Science*, *39*, 61–75.

[26] Cazabat, A. M., Heslot, F., Troian, S. M. & Carles P. (1990). Fingering instability of thin spreading films driven by temperature gradients. *Nature*, *346*, 824–826.

[27] Churaev, N. V., Starov, V. M. & Derjaguin, B. V. (1982). The shape of the transition zone between a thin film and bulk liquid and the line tension. *Journal of Colloid and Interface Science*, *89*, 16–24.

[28] Craik, A. D. D. (1966). Wind-generated waves in thin liquid films. *Journal of Fluid Mechanics*, *26*, 369–392.

[29] Crank J. & Nicolson P. (1947). A practical method for numerical evaluation of solutions of partial differential equations of the heat conduction type. *Proceedings of the Cambridge Philosophical Society*, *43*, 50–67.

[30] Davis, S. H. (1987). Thermocapillary instabilities. *Annual Review of Fluid Mechanics*, *19*, 403–435.

[31] de Bruyn, J. R. (1992). Growth of fingers at a driven three-phase contact line. *Physical Review A*, *46*(8), R4500.

[32] de Gennes, P. G. (1985). Wetting: statics and dynamics. *Reviews of Modern Physics*, *57*, 827–863.

[34] Derjaguin, B. V. & Churaev, N. V. (1976). Polymolecular adsorption and capillary condensation in narrow slit pores. *Journal of Colloid and Interface Science*, *54*(2), 157–175.

[34] Derjaguin, B. V. & Churaev, N. V. (1986). *Properties of water layers adjacent to interfaces.* In *Fluid interfacial phenomena* edited by C. A. Croxton. New York: Wiley.

[35] Dietrich, S. & Napiorkowski, M. (1991). Analytic results for wetting transitions in the presence of van der Waals tails. *Physical Review A*, *43*, 1861–1885.

[36] Diez, J. & Kondic, L. (2001). Contact line instabilities of thin liquid films. *Physical Review Letters*, *86*(4), 632–635.

[37] Diez, J., Kondic, L. & Bertozzi, A. L. (2000). Global models for moving contact lines. *Physical Review E*, *63*, 011208.

[38] Dobbs, H. T. & Indekeu, J. O. (1993). Line tension at wetting: interface displacement model beyond the gradient-squared approximation. *Physica A*, *201*, 457–481.

[39] Dussan V E. B. & Davis, S. H. (1974). On the motion of a fluid-fluid interface along a solid surface. *Journal of Fluid Mechanics*, *65*, 71–95.

[40] Dussan V E. B. (1979). On the spreading of liquids on solid surface: Static and dynamic contact lines. *Journal of Fluid Mechanics*, *11*, 371–400.

[41] Edmonstone, B. D., Matar, O. K. & Craster, R. V. (2002). Surfactant-induced fingering phenomena in thin film flow down an inclined plane. *Physica D*, *209*, 62–79.

[42] Eckhaus, W. (1965). *Studies in nonlinear stability theory.* Berlin: Springer.

[43] Eres, M. H., Schwartz, L. W. & Roy, R. V. (2000). Fingering phenomena for driven coating films. *Physics of Fluids*, *12*, 1278–1295.

[44] Fan, H., Gao, Y. X. & Huang, X. Y. (2001). Thermodynamics modeling for moving contact line in gas/liquid/solid system: Capillary rise problem revisited. *Physics of Fluids*, *13*(6), 1615–1623.

[45] Fan, H. (2006). Liquid droplet spreading with line tension effect. *Journal of Physics: Condensed Matter*, *18*, 4481–4488.

[46] Feldman, S. (1957). On the hydrodynamic stability of two viscous incompressible fluids in parallel uniform shearing motion. *Journal of Fluid Mechanics*, *2*, 343–370.

[47] Finn, R. (1986). *Equilibrium capillary system.* New York: Springer-Verlag.

[48] Frumkin, A. N. (1938). On the phenomena of wetting and sticking of bubbles. *Zhurnal Fizicheskoi Khimii*, *12*, 337–345, (in Russian).

[49] Gaver, D. P., III & Grotberg, J. B. (1990). The dynamics of a localized surfactant on a thin film. *Journal of Fluid Mechanics*, *213*, 127–148.

[50] Glasner, K. B. (2003). Spreading of droplets under the influence of intermolecular forces. *Physics of Fluids*, *15*(7), 1837–1842.

[51] Halpern, D. & Grotberg, J. B. (1992). Dynamics and transport of a localized soluble surfactant on a thin film. *Journal of Fluid Mechanics*, *237*, 1–11.

[52] Hansman, R. J. & Turnock, S. R. (1989). Investigation of surface water behavior during glaze ice accretion. *Journal of Aircraft*, *26*(2), 140–147.

[53] Hocking, L. M. (1993). The influence of intermolecular forces on thin fluid layers. *Physics of Fluids*, *5*, 793–799.

[54] Hooper, A. P. & Boyd, W. G. (1987). Shear-flow instability due to a wall and a viscosity discontinuity at the interface. *Journal of Fluid Mechanics*, *179*, 201–225.

[55] Huppert, H. E. (1982). Flow and instability of a viscous current down a slope. *Nature*, *300*, 427–429.

[56] Indekeu, J. O. (1992). Line tension near the wetting transition: results from an interface displacement model. *Physica A*, *183*, 439–461.

[57] Indekeu, J. O. (1994). Line tension at wetting. *International Journal of Modern Physics B*, *8*(3), 309–345.

[58] Islam, Md. N. & Kato, T. (2003). Thermodynamic study on surface adsorption and micelle formation of poly(ethylene glycol) mono-n-tetradecyl ethers. *Langmuir*, *19*, 7201–7205.

[59] Jerrett, J. M. & de Bruyn, J. R. (1992). Fingering instability of a gravitationally driven contact line. *Physics of Fluids A*, *4*(2), 234–242.

[60] Joesph, D. D. (1976). *Stability of fluid motions.* 2 vols. Springer Tracts in natural philosophy, vols 27 and 28. Berlin: Springer.

[61] Johnson, M. F. G., Schluter, R. A., Miksis, M. J., & Bankoff, S. G. (1992). Experimental study of rivulet formation on an inclined plate by fluorescent imaging. *Journal of Fluid Mechanics*, *394*, 339–354.

[62] Johnson, R. E. (1959). Conflicts between gibbsian thermodynamics and recent treatments of interfacial energies in solid-liquid-vapor system. *Journal of Physical Chemistry*, *63*, 1655–1658.

[63] Kalliadasis, S., Bielarz, C. & Homsy, G. M. (2000). Steady free-surface thin film flows over topography. *Physics of Fluids*, *12*(8), 1889–1998.

[64] Kalliadasis, S. & Homsy, G. M. (2001). Stability of free-surface thin film flows over topography. *Journal of Fluid Mechanics*, *448*, 387–410

[65] Kataoka, D. E. & Troian, S. M. (1997). A theoretical study of instabilities at the advancing front of thermally driven coating films. *Journal of Colloid and Interface Science*, *192*, 350–362.

[66] Khanna, R. & Sharma, A. (1997). Pattern formation in spontaneous dewetting of thin apolar films. *Journal of Colloid and Interface Science*, *195*(1), 42–50.

[68] Kralchevsky, P. A. & Ivanov, I. B. (1985). On the Mechanical Equilibrium between a Film of Finite Thickness and the External Meniscus. *Chemical Physics Letters*, *121*, 111–116.

[68] Kralchevsky, P. A. & Ivanov, I. B. (1985). The Transition Region between a Thin Film and the Capillary Meniscus. *Chemical Physics Letters*, *121*, 116–121.

[69] Krotov, V. V. & Rusanov, A. I. (1999). *Physicochemical hydrodynamics of capillary system.* London: Imperial College Press.

[70] Lanczos, C. (1966) *The variational principles of mechanics.* Third Edition. Toronto: University of Toronto Press.

[71] Leibovich, S. & Seebass, A. R. (1974). *Nonlinear waves.* Ithaca [N.Y.]: Cornell University Press.

[72] Levich, V. G. (1962). *Physicochemical hydrodynamics. U.S.S.R Translated by* Scripta Technica, Inc, 1962.

[73] Levich, V. G. & Krylov, V. S. (1969). Surface-tension-driven phenomena. *Annual Review of Fluid Mechanics*, *1*, 293–316.

[74] Li, D. & Neumann, A. W. (1991). Thermodynamics of contact angle phenomena in the presence of a thin liquid film. *Advances in Colloid and Interface Science*, *36*, 125–151.

[75] Lighthill, M. J. (1978). *Waves in fluids.* Cambridge: Cambridge University Press.

[76] Lin, C. C. (1955). *The theory of hydrodynamic stability.* Cambridge: Cambridge University Press.

[77] Lock, R. C. (1954). Hydrodynamic stability of the flow in the laminar boundary layer between parallel streams. *Proceedings of the Cambridge Philosophical Society. Mathematical and Physical Sciences*, *50*, 105–124.

[78] Ludviksson, V. & Lightfoot, E. N. (1971). The dynamics of thin liquid films in the presence of surface-tension gradients. *AIChE Journal*, *17*(5), 1166–1173.

[79] Luo, H. & Pozrikdis C. (2006). Shear-driven and channel flow of a liquid film over a corrugated or indented wall. *Journal of Fluid Mechanics*, *556*, 167–188.

[80] Matar, O. K. & Troian, S. M. (1999). The development of transient fingering patterns during the spreading of surfactant coated films. *Physics of Fluids*, *11*(11), 3232–3246.

[81] Matheis, B. D. & Rothmayer, A. P. (2003). Impact of underlying surface roughness on water mass transport. *AIAA paper 2003-1220*, presented at the 41st Aerospace Sciences Meeting, Reno NV.

[82] Marshall, J. S. & Ettema, R. (2004). *Contact-line instabilities of driven liquid films.* In: Rahman M. (ed.), *Instability of Flows.* Southampton, UK; Boston: WIT Press.

[83] Messiter, A. F. (1970). Boundary-layer flow near the trailing edge of a flat plate. *SIAM Journal on Applied Mathematics*, *18*(1), 241–257.

[84] Messinger, B. L. (1953). Equilibrium temperature of unheated icing surface as a function of airspeed. *Journal of Aeronautical Science*, *20*(1), 29–42.

[85] Miles, J. W. (1959). On the generation of surface waves by shear flows. Part 2. *Journal of Fluid Mechanics*, *6*, 568–582.

[86] Miles, J. W. (1962). On the generation of surface waves by shear flows. Part 4. *Journal of Fluid Mechanics*, *13*, 433–448.

[87] Minkov, E. & Novick-Cohen, A. (2001). Droplet profiles under the influence of van der Waals forces. *European Journal of Applied Mathematics*, *12*, 367–393.

[88] Witelski, T.P. & Bowen, M. (2003). ADI schemes for higher-order nonlinear diffusion equations. *Applied Numerical Mathematics*, *45*, 331–351.

[89] Myers, T. G., Charpin, J. P. E. & Chapman, S. J. (2002). The flow and solidification of a thin film on an arbitrary three dimensional surface. *Physics of Fluids*, *14(8)*, 2788–2803.

[90] Neiland, V. Ya. (1969). Theory of laminar boundary layer separation in supersonic flow. *Fluid Dynamics*, *4*(4), 33–35.

[91] Neumann, A. W. & Spelt, J. K. (1996). *Applied surface thermodynamics*. New York: Marcel Dekker.

[92] Olsen, W., Shaw, R. & Newton, J. (1984). Ice shapes and the resulting drag increase for a NACA 0012 airfoil. *AIAA paper 1984-0109*, presented at the 22nd Aerospace Sciences Meeting, Reno NV.

[93] Olsen, W. & Walker, E. (1987). Experimental evidence for modifying the current physical model for ice accretion on aircraft structures. *NASA Technical Memorandum* 87184, 1–45.

[94] Oron, A. & Bankoff, S. G. (1999). Dewetting of a heated surface by an evaporating liquid film under conjoining/disjoining pressures. *Journal of Colloid and Interface Science*, *218*(1), 152–166.

[95] Oron, A., Davis, S. H. & Bankoff, S. G. (1997). Long-scale evolution of thin liquid films. *Reviews of Modern Physics*, *69*(3), 931–980.

[96] Poinsatte, P. E., Van Fossen, G. J., Newton, J. E. & De Witt, K. J. (1991). Heat transfer measurements from a smooth NACA 0012 airfoil. *Journal of Aircraft*, *28*(12), 892–898.

[97] Poinsatte, P. E., Van Fossen, G. J. & De Witt, K. J. (1991). Roughness effects on heat transfer from a NACA 0012 airfoil. *Journal of Aircraft*, *28*(12), 908–911.

[98] Pelekasis, N. A. & Tsamopoulos, J. A. (2001). Linear stability of a gas boundary layer flowing past a thin liquid film over a flat plate. *Journal of Fluid Mechanics*, *436*, 321–352.

[99] Pismen, L. M. & Thiele, U. (2006). Asymptotic theory for a moving droplet driven by a wettability gradient. *Physics of Fluids*, *18*(041204).

[100] R Rosen, M. J. (1989). *Surfactants and interfacial phenomena*. 2nd ed., New York: Wiley.

[101] Rothmayer, A. P. (2003). Scaling laws for water and ice layers on airfoils. *AIAA paper 2003-1217*, presented at the 41st Aerospace Sciences Meeting, Reno NV.

[102] Rothmayer, A. P. (2003). On the creation of ice surface roughness by interfacial instabilities. *AIAA paper 2003-0972*, presented at the 41st Aerospace Sciences Meeting, Reno NV.

[103] Rothmayer, A. P. & Krakos, J.A. (2004). Residual droplet impacts and thin film dynamics. *AIAA paper 2004-0057*, presented at the 42nd Aerospace Sciences Meeting, Reno NV.

[104] Rothmayer, A. P. (2006). Stagnation point icing. *AIAA paper 2006-1081*, presented at the 44th Aerospace Sciences Meeting, Reno NV.

[105] Rothmayer, A. P., Matheis, B. D. & Timoshin, S. N. (2002). Thin liquid film flowing over external aerodynamic surfaces. *Journal of Engineering Mathematics*, *42*, 341–357.

[106] Rothmayer, A. P. & Smith, F. T. (1998). Incompressible triple-deck theory. Part III Chapter 23 In: R.W. Johnson (ed.), *The Handbook of Fluid Dynamics*, Boca Raton: CRC Press, 23/1–23/24.

[107] Rothmayer, A. P. & Tsao, J. C. (2000). Water film runback on an airfoil surface. *AIAA paper 2000-0237*, presented at the 38th Aerospace Sciences Meeting, Reno NV.

[109] Roura, P. & Fort, J. (2004). Local thermodynamic derivation of Youngs equation. *Journal of Colloid and Interface Science*, *272*, 420–429

[109] Roura, P. (2005). Thermodynamic derivations of the mechanical equilibrium conditions for fluid surfaces: Youngs and Laplaces equations. *American Journal of Physics*, *73*(12), 1139–1147

[110] Rusanov, A. I. (1992). Problems of surface thermodynamics. *Pure and Applied Chemistry*, *64*(1), 111–124.

[111] Schlichting, H. & Gersten, K. (1999). *Boundary layer theory.* New York: Springer-Verlag.

[112] Schwartz, L. W. & Eley, R. R. (1998). Simulation of droplet motion on low-energy and heterogeneous surfaces. *Journal of Colloid and Interface Science*, *202*(1), 173–188.

[113] Schwartz, L. W. (1989). Viscous flows down an inclined plane: instability and finger formation. *Physics of Fluids A*, *1*(3), 443–445.

[114] Schwartz, L. W. & Weidner, D. E. (1995). Modeling of coating flows on curved surfaces. *Journal of Engineering Mathematics*, *29*, 91–103.

[115] Shapiro, E. & Drikakis, D. (2005). Artificial compressibility, characteristics-based schemes for variable density, incompressible, multi-species flows. Part I. Derivation of different formulations and constant density limit. *Journal of Computational Physics*, *210*(2), 584–607.

[116] Shuaib, N. H., Powera, H. & Hibberd, S. (2006). Multiple solutions of gravity and surface shear driven thin film flows over a rectangular cavity. *Physics of Fluids*, *12*, No.057102.

[117] Silvi, N. & Dussan, V E. B. (1985). On the rewetting of an inclined solid surface by a liquid. *Physics of Fluids*, *28*(1), 5–7.

[118] Smith, F. T., Brighton, P. W. M., Jackson, P. S. & Hunt, J. C. R. (1981). On boundary-layer flow past two-dimensional obstacles. *Journal of Fluid Mechanics*, *113*, 123–152.

[119] Smith, F. T. (1983). Properties and a finite-difference approach for interactive three-dimensional boundary layers. *United Technologies Research Center Rept.*, *83*(46).

[120] Solomentsev, Y. & White, L. R. (1999). Microscopic drop profiles and the origins of line tension. *Journal of Colloid and Interface Science*, *218*, 122–136

[121] Stewartson, K. & Williams, P. G. (1969). Self induced separation. *Proceedings of the Royal Society of London*, *A312*, 181–206.

[122] Stillwagon, L. E. & Larson, R. G. (1990). Levelling of thin films over uneven substrates during spin coating. *Physics of Fluids A*, *2*(11), 1937–1944.

[123] Stoker, J. J. (1957). *Water waves.* New York: Interscience.

[124] Stone, H. A. (1990). A simple derivation of the time-dependent convective-diffusion equation for surfactant transport along a deforming interface. *Physics of Fluids A*, *2*, 111–112.

[125] Sun, T. F. & Teja, A. S. (2003). Density, viscosity, and thermal conductivity of aqueous ethylene, diethylene, and triethylene glycol mixtures between 290 K and 450 K. *Journal of Chemical & Engineering Data*, *48*, 198–202.

[126] Thomas, S. K., Cassoni, R. P. & MacArthur, C. D. (1996). Aircraft anti-icing and de-icing techniques and modeling. *Journal of Aircraft*, *33*(5), 841–854.

[127] Tannehill, J. C., Dale, A. A. & Pletcher, R. H. (1997). *Computational Fluid Mechanics and Heat Transfer*(2nd edition). Taylor & Francis.

[128] Timoshin, S. N. (1997). Instability in a high Reynolds number boundary layer on a film-coated surface. *Journal of Fluid Mechanics*, *353*, 163–195.

[129] Timoshin, S. N. & Hooper, A. P. (2000). Mode coalescence in a two-fluid boundary-layer stability problem. *Physics of Fluids*, *12*, 1969–1978.

[130] Troian, S. M., Wu, X. L. & Safran S. A. (1989). Fingering instability in thin wetting films. *Physical Review Letters*, *62*, 1496–1500.

[131] Troian, S. M., Herbolzheimer, E., Safran, S. A. & Joanny J. F. (1989). Fingering instabilities of driven spreading films. *Europhysics Letters*, *10*(1), 25–30.

[132] Tsao, J. C., Rothmayer, A. P. & Ruban, A. I. (1997). Stability of air flow past thin liquid films on airfoils. *Computers & Fluids*, *26*(5), 427–452.

[133] Yih, C. S. (1967). Instability due to viscosity stratification. *Journal of Fluid Mechanics*, *27*, 337–352.

[134] Yih, C. S. (1990). Wave formation on a liquid layer for de-icing airplane wings. *Journal of Fluid Mechanics*, *212*, 41–53.

[135] van Leer, B. (1979). Towards the ultimate conservative difference scheme. V. A second-order sequel to Godunov's method. *Journal of Computational Physics*, *32*, 101–136.

[136] Valenzuela, G. R. (1976). The growth of gravity-capillary waves in a coupled shear flow. *Journal of Fluid Mechanics*, *76*, 229–250.

[137] van Gastel, K., Janssen, P. A. E. M. & Komen, G. J. (1985). On phase velocity and growth rate of wind-induced gravity-capillary waves. *Journal of Fluid Mechanics*, *161*, 199–216.

[138] Vargas, M. (2005). Current experimental basis for modeling ice accretions on swept wings. *AIAA paper 2005-5188*, presented at the 4th AIAA Theoretical Fluid Mechanics Meeting, Toronto, Ontario Canada.

[139] Vold, R. D. & Vold, M. J. (1983). *Colloid and interface chemistry.* London: Addison-Wesley.

[140] Wang, G. & Rothmayer, A. P. (2005). Air driven water flow past small scale surface roughness. *AIAA paper 2005-0653*, presented at the 43rd Aerospace Sciences Meeting, Reno NV.

[141] Wang, G. & Rothmayer, A. P. (2007a). Properties of thin water films driven by air through surface roughness. *AIAA paper 2007-0901*, presented at the 45th Aerospace Sciences Meeting, Reno NV.

[142] Wang, G. & Rothmayer, A. P. (2007b). Thin water films driven by air shear stress through roughness. *Computers & Fluids*, accepted.

[143] Warner, M. R. E., Craster R. V. & Matar, O. K. (2002). Unstable van der Waals driven line rupture in Marangoni driven thin viscous films. *Physics of Fluids*, *14*(5), 1642–1654.

[145] Weast, R. C., Astle, M. J. & Beyer, W. H. (1986). *CRC Handbook of Chemistry and Physics.* Boca Raton, FL: CRC Press.

[145] White, L. R. (1977). On deviations from Young's equation. *Journal of the Chemical Society, Faraday Transactions*, *73*, 390–398.

[146] Whitham, G. B. (1974). *Linear and nonlinear waves.* New York: Wiley.

[147] Williams, M. B. & Davis, S. H. (1982). Nonlinear theory of film rupture. *Journal of Colloid and Interface Science*, *90*(1), 220–228.

[148] Wong, H., Rumschitzki, D. & Maldarelli, C. (1996). On the surfactant mass balance at a deforming fluid interface. *Physics of Fluids*, *8*(11), 3203–3204.

[149] Wu, Q. F. & Wong, H. (2004). A slope-dependent disjoining pressure for non-zero contact angles. *Journal of Fluid Mechanics*, *506*, 157–185.